

THE USE OF MICROWAVE TOMOGRAPHY IN BONE HEALING  
MONITORING

by

Mohanad Ahmed Alkhodari

A Thesis Presented to the Faculty of the  
American University of Sharjah  
College of Engineering  
in Partial Fulfillment  
of the Requirements  
for the Degree of

Master of Science in  
Biomedical Engineering

Sharjah, United Arab Emirates

April 2019



## Approval Signatures

We, the undersigned, approve the master's thesis of Mohanad Alkhodari.

Thesis Title: The Use of Microwave Tomography in Bone Healing Monitoring

**Signature**

**Date of Signature**

---

Dr. Amer Zakaria  
Assistant Professor, Department of Electrical Engineering  
Thesis Advisor

---

Dr. Nasser Qaddoumi  
Professor, Department of Electrical Engineering  
Thesis Advisor

---

Dr. Salam Dhou  
Assistant Professor, Department of Computer Science and Engineering  
Thesis Committee Member

---

Dr. Mahmoud H. Ismail  
Associate Professor, Department of Electrical Engineering  
Thesis Committee Member

---

Dr. Hasan Al-Nashash  
Director, Biomedical Engineering Graduate Program

---

Dr. Lotfi Romdhane  
Associate Dean for Graduate Affairs and Research  
College of Engineering

---

Dr. Naif Darwish  
Acting Dean, College of Engineering

---

Dr. Mohamed El Tarhuni  
Vice Provost for Graduate Studies

## **Acknowledgments**

First and foremost, I would like to acknowledge the support of the American University of Sharjah (AUS) and the Biosciences and Bioengineering Research Institute (BBRI) in supplying me with an adequate research budget and with the equipment needed to complete simulations and experiments relevant to my master degree thesis in Biomedical Engineering. I genuinely appreciate the support of the universitys Electrical Engineering department and graduate program of biomedical engineering faculty who granted me the graduate teaching and research assistantship throughout the whole period of studying, which highly enhanced my learning abilities and working skills.

Further, I would like to extend my heartfelt gratitude to my first supervisor, Dr. Amer Zakaria. None of this work would have been accomplished without his weekly supervision and assistance as well as his unstoppable motivation. I would also like to acknowledge the efforts made by my second supervisor, Prof. Nasser Qaddoumi, in the support throughout the work on this thesis. Both of them have actually spared no efforts in putting me on the right track through their valuable comments and recommendations. Last but not least, I am grateful to Dr. Hasan Al-Nashash for he has inspired me to pick this area of research presented in my thesis. His positivity, enthusiasm, and insightful guidance have urged me to bring out my maximum efforts.

Special thanks go to my parents, Ahmed and Eman Alkhodari, and my siblings, Amani, Husam, and Tahani, for their encouragements and positive reassurances throughout my journey as a graduate student. Besides, I cannot forget my sweet pet, Eid, for the comfort he provided me with whenever I felt stressed out. Above all, I thank Allah Subhanahu wa Taala who guided me to achieve my goals and accomplishments so far and who made everything in this journey possible.

## **Dedication**

*To my Family and all the Growing Human Minds...*

## Abstract

In this thesis, a numerical study is conducted to investigate the use of microwave tomography in monitoring bone health in human lower limbs. By monitoring bone volume fraction (BVF) and bone density, the effectiveness of Vitamin D treatment can be evaluated for osteoporosis patients. In microwave tomography, the leg is radiated with non-ionizing low-power electromagnetic signals with scattered electric fields measured at several locations surrounding the leg. Within the framework of inverse scattering problems, the measured fields are used as inputs for an optimization algorithm to estimate the location and electrical properties inside the human leg. In this work, three two-dimensional cross-sectional models of human leg at different fat thicknesses are created and simulated using a finite-element method, where the transverse magnetic approximation is applied. The synthetic results are then inverted using a finite-element contrast source inversion method. Furthermore, an enhancement procedure is followed to investigate the effect of incorporating prior information about the object-of-interest (OI), changing the boundaries of the imaging domain, relocating antennas, and using ultrasound gel as a matching medium. In addition, an image processing approach is provided to build estimated models to be used in the enhancement procedure. The final results show that variations in BVF affect the results of the inversion algorithm. The real part relative permittivity line plots showed a downward trend as the BVF increases, which can be related to an increase in the bone density. The outcomes of this thesis support the hypothesis that a MWT wearable system is useful for bone density monitoring application, and more specifically for Vitamin D treatment evaluation.

**Search Terms:** *Bone density, bone volume fraction, electromagnetic imaging, microwave tomography, finite-element method, contrast source inversion, k-means clustering, inhomogeneous background*

## Table of Contents

Abstract . . . . .	6
List of Figures . . . . .	9
List of Tables . . . . .	15
List of Abbreviations . . . . .	16
Chapter 1. Introduction . . . . .	17
1.1 Scope of Research . . . . .	17
1.2 Motivation . . . . .	17
1.3 Background . . . . .	18
1.3.1 Medical imaging . . . . .	18
1.3.2 Microwave imaging . . . . .	19
1.3.3 Anatomy of human leg bones . . . . .	22
1.3.4 Vitamin D and bone volume fraction (BVF) . . . . .	25
1.4 Current State-of-Art in MWT . . . . .	26
1.5 Thesis Problem Statement . . . . .	29
1.6 Thesis Outline . . . . .	30
Chapter 2. Mathematical Formulation and Numerical Modeling . . . . .	32
2.1 The Forward Problem . . . . .	32
2.2 Two-Dimensional Transverse Magnetic Approximation . . . . .	35
2.3 The Finite Element Method (FEM) . . . . .	36
2.4 Solving the Inverse Problem . . . . .	37
2.4.1 The contrast source inversion . . . . .	38
2.4.2 FEM-CSI . . . . .	39
Chapter 3. Numerical Modeling and Blind Inversion . . . . .	42
3.1 Human Leg Modeling . . . . .	42
3.2 Optimum Frequency Selection . . . . .	44
3.3 Forward Simulations . . . . .	46
3.4 Blind Inversion . . . . .	48

3.5	Inversion at Non-optimum Frequencies . . . . .	50
3.6	Analysis and Observations . . . . .	52
Chapter 4. Inversion Enhancements . . . . .		56
4.1	Incorporating Prior Information . . . . .	56
4.2	Varying the Imaging Domain Boundary . . . . .	59
4.3	Relocating Antennas . . . . .	64
4.4	Changing the Matching Medium . . . . .	69
4.5	Analysis and Observations . . . . .	73
Chapter 5. Image Processing for Enhanced Reconstruction . . . . .		81
5.1	K-means Clustering . . . . .	81
5.2	Structural Information Extraction Procedure . . . . .	82
5.3	Pre-Processing . . . . .	84
5.3.1	Conversion to a square grid . . . . .	84
5.3.2	Extraction of the matching medium . . . . .	85
5.4	Clustering Algorithm . . . . .	86
5.5	Building the Estimated Model . . . . .	91
5.6	Inversion Results . . . . .	98
5.7	Analysis and Observations . . . . .	102
Chapter 6. Analysis on Bone Health Monitoring . . . . .		115
6.1	Bone Density Variations . . . . .	115
6.2	Building the Estimated Models . . . . .	118
6.3	Enhanced Inversion Results . . . . .	118
6.4	Statistical Analysis of Bone Health Variations . . . . .	125
6.5	Analysis and Observations . . . . .	126
Chapter 7. Conclusion and Future Work . . . . .		129
References . . . . .		130
Vita . . . . .		137



## List of Figures

Figure 1.1: Microwave tomography system configuration. . . . .	21
Figure 1.2: Leg bones structure and anatomy. retrieved from [19]. . . . .	23
Figure 1.3: Cross-sectional view of the leg structure. retrieved from [20]. . . . .	24
Figure 2.1: The overall mathematical procedure of reconstructing MWT images. . . . .	40
Figure 3.1: Three cross-sectional MRI images representing three fat layer thick- nesses. . . . .	42
Figure 3.2: MRI Axial image for human leg showing structures including skin, fat, muscles, tibia and fibula. . . . .	43
Figure 3.3: Triangular meshes generated by GMSH of the three MRI images. . . . .	44
Figure 3.4: MRI model 1: The real and imaginary components of the relative complex permittivity reconstruction. . . . .	49
Figure 3.5: MRI model 2: The real and imaginary components of the relative complex permittivity reconstruction. . . . .	49
Figure 3.6: MRI model 3: The real and imaginary components of the relative complex permittivity reconstruction. . . . .	50
Figure 3.7: Testing frequency values on MRI model 1 healthy bone. . . . .	51
Figure 3.8: Testing frequency values on MRI model 2 healthy bone. . . . .	51
Figure 3.9: Testing frequency values on MRI model 3 healthy bone. . . . .	52
Figure 3.10: Box plot representation of relative permittivity values using the for- ward model as bone mask in MRI model 1. . . . .	54
Figure 3.11: Box plot representation of relative permittivity values using the for- ward model as bone mask in MRI model 2. . . . .	54
Figure 3.12: Box plot representation of relative permittivity values using the for- ward model as bone mask in MRI model 3. . . . .	54
Figure 3.13: The box plot representation of the tibia bone real part relative per- mittivity in MRI model 1. . . . .	55
Figure 3.14: The box plot representation of the tibia bone real part relative per- mittivity in MRI model 2. . . . .	55
Figure 3.15: The box plot representation of the tibia bone real part relative per- mittivity in MRI model 3. . . . .	55
Figure 4.1: Structural information used within the inversion mesh as prior infor- mation for MRI model 1. . . . .	57

Figure 4.3: Structural information used within the inversion mesh as prior information for MRI model 3. . . . .	58
Figure 4.2: Structural information used within the inversion mesh as prior information for MRI model 2. . . . .	58
Figure 4.4: Inversion meshes with prior information about location and dielectric properties of tissues for MRI models 1, 2, and 3. . . . .	59
Figure 4.5: Incorporating prior info to enhance MRI model 1 reconstruction. . .	60
Figure 4.6: Incorporating prior info to enhance MRI model 2 reconstruction. . .	61
Figure 4.7: Incorporating prior info to enhance MRI model 3 reconstruction. . .	62
Figure 4.8: Old and new imaging domain boundaries for MRI model 1. . . . .	63
Figure 4.9: Old and new imaging domain boundaries for MRI model 2. . . . .	64
Figure 4.10: Old and new imaging domain boundaries for MRI model 3. . . . .	64
Figure 4.11: Varying imaging domain to enhance MRI model 1 reconstruction. . .	65
Figure 4.12: Varying imaging domain to enhance MRI model 2 reconstruction. . .	66
Figure 4.13: Varying imaging domain to enhance MRI model 3 reconstruction. . .	67
Figure 4.14: Old and new antennas' locations for MRI model 1. . . . .	68
Figure 4.15: Old and new antennas' locations for MRI model 2. . . . .	68
Figure 4.16: Old and new antennas' locations for MRI model 3. . . . .	69
Figure 4.17: Changing location of antennas to enhance MRI model 1 reconstruction.	70
Figure 4.18: Changing location of antennas to enhance MRI model 2 reconstruction.	71
Figure 4.19: Changing location of antennas to enhance MRI model 3 reconstruction.	72
Figure 4.20: Relative permittivity values of AquaSonic 100 ultrasound gel. . . . .	73
Figure 4.21: The effect of using ultrasound gel as matching medium for MRI model 1 . . . . .	74
Figure 4.22: The effect of using ultrasound gel as matching medium for MRI model 2 . . . . .	75
Figure 4.23: The effect of using ultrasound gel as matching medium for MRI model 3 . . . . .	76
Figure 5.1: Reconstruction enhancement using k-means clustering algorithm complete procedure. . . . .	83

Figure 5.2: The extraction process of the Glycerin/Water matching medium real part values in MRI models 1, 2, and 3. . . . .	87
Figure 5.3: The extraction process of the Glycerin/Water matching medium imaginary part values in MRI models 1, 2, and 3. . . . .	88
Figure 5.4: The extraction process of the ultrasound gel matching medium real part values in MRI models 1, 2, and 3. . . . .	89
Figure 5.5: The extraction process of the ultrasound gel matching medium imaginary part values in MRI models 1, 2, and 3. . . . .	90
Figure 5.6: K-means clusters from the real part relative permittivity images in MRI models 1, 2, and 3 using Glycerin/Water solution (Left = <i>Low-Permittivity</i> , Right = <i>High-Permittivity</i> ). . . . .	92
Figure 5.7: K-means clusters from the real part relative permittivity images in MRI models 1, 2, and 3 using ultrasound gel (Left = <i>Low-Permittivity</i> , Right = <i>High-Permittivity</i> ). . . . .	93
Figure 5.8: K-means clusters from the imaginary part relative permittivity images in MRI models 1, 2, and 3 using Glycerin/Water solution (Left = <i>Low-Permittivity</i> , Right = <i>High-Permittivity</i> ). . . . .	94
Figure 5.9: K-means clusters from the imaginary part relative permittivity images in MRI models 1, 2, and 3 using ultrasound gel (Left = <i>Low-Permittivity</i> , Right = <i>High-Permittivity</i> ). . . . .	95
Figure 5.10: Extracting boundaries of the real part of relative permittivity <i>Low-Permittivity</i> cluster with Glycerin/Water solution for MRI model 1. . . . .	96
Figure 5.11: Extracting boundaries of the real part relative permittivity <i>Low-Permittivity</i> cluster with Glycerin/Water solution for MRI model 2. . . . .	97
Figure 5.12: Extracting boundaries of the real part relative permittivity <i>Low-Permittivity</i> cluster with Glycerin/Water solution for MRI model 3. . . . .	97
Figure 5.13: Extracting the boundaries of the real part relative permittivity <i>Low-Permittivity</i> cluster with ultrasound gel for MRI model 1. . . . .	98
Figure 5.14: Extracting boundaries of the real part relative permittivity <i>Low-Permittivity</i> cluster with ultrasound gel for MRI model 2. . . . .	98
Figure 5.15: Extracting boundaries of the real part relative permittivity <i>Low-Permittivity</i> cluster with ultrasound gel for MRI model 3. . . . .	99
Figure 5.16: Extracting the boundaries of the imaginary part relative permittivity clusters with Glycerin/Water solution (Left = <i>Low-Permittivity</i> , Right = <i>High-Permittivity</i> ). . . . .	100

Figure 5.17: Extracting the boundaries of the imaginary part relative permittivity clusters with ultrasound gel (Left = <i>Low-Permittivity</i> , Right = <i>High-Permittivity</i> ). . . . .	101
Figure 5.18: The boundary of the estimated model created using real part relative permittivity clusters along with new imaging domain and antennas location (Left = Forward problem MRI models, Middle = Glycerin/Water solution models, Right = Ultrasound gel models). . . . .	102
Figure 5.19: The boundary of the estimated model created using imaginary part relative permittivity clusters along with new imaging domain and antennas location (Left = Forward problem MRI models, Middle = Glycerin/Water solution models, Right = Ultrasound gel models). . . . .	103
Figure 5.20: Inversion results for the real-part based clustering model using the Glycerin/Water solution with mid-value inhomogeneous scenario. . . . .	104
Figure 5.21: Inversion results for the real-part based clustering model using the Glycerin/Water solution with skin-fat inhomogeneous scenario. . . . .	105
Figure 5.22: Inversion results for the real-part based clustering model using the ultrasound gel with mid-value inhomogeneous scenario. . . . .	106
Figure 5.23: Inversion results for the real-part based clustering model using the ultrasound gel with skin-fat inhomogeneous scenario. . . . .	107
Figure 5.24: Inversion results for the imaginary-part based clustering model using the Glycerin/Water solution with mid-value inhomogeneous scenario. . . . .	108
Figure 5.25: Inversion results for the imaginary-part based clustering model using the Glycerin/Water solution with skin-fat inhomogeneous scenario. . . . .	109
Figure 5.26: Inversion results for the imaginary-part clustering model using the Glycerin/Water solution with skin-fat-muscle inhomogeneous scenario. . . . .	110
Figure 5.27: Inversion results for the imaginary-part clustering model using the ultrasound gel with mid-value inhomogeneous scenario. . . . .	111
Figure 5.28: Inversion results for the imaginary-part clustering model using the ultrasound gel with skin-fat inhomogeneous scenario. . . . .	112
Figure 5.29: Inversion results for the imaginary-part based clustering model using the ultrasound gel with skin-fat-muscle inhomogeneous scenario. . . . .	113
Figure 6.1: MRI model 1: The real and imaginary components of the relative permittivity reconstructions using Glycerin/Water solution. . . . .	116
Figure 6.2: MRI model 1: The real and imaginary components of the relative permittivity reconstructions using ultrasound gel. . . . .	116

Figure 6.3: MRI model 2: The real and imaginary components of the relative permittivity reconstructions using Glycerin/Water solution. . . . .	116
Figure 6.4: MRI model 2: The real and imaginary components of the relative permittivity reconstructions using ultrasound gel. . . . .	117
Figure 6.5: MRI model 3: The real and imaginary components of the relative permittivity reconstructions using Glycerin/Water solution. . . . .	117
Figure 6.6: MRI model 3: The real and imaginary components of the relative permittivity reconstructions using ultrasound gel. . . . .	117
Figure 6.7: MRI model 1: The real-part based clustering estimated models. . . .	118
Figure 6.8: MRI model 2: The real-part based clustering estimated models. . . .	119
Figure 6.9: MRI model 3: The real-part based clustering estimated models. . . .	119
Figure 6.10: MRI model 1: The imaginary-part based clustering estimated models.	119
Figure 6.11: MRI model 2: The imaginary-part based clustering estimated models.	120
Figure 6.12: MRI model 3: The imaginary-part based clustering estimated models.	120
Figure 6.13: MRI model 1: The mid-value inversion results using the real-part based clustering estimated model for 80:20 Glycerin/Water solution.	121
Figure 6.14: MRI model 1: The skin-fat inversion results using the real-part based clustering estimated model for 80:20 Glycerin/Water solution. . . . .	121
Figure 6.15: MRI model 1: The mid-value inversion results using the real-part based clustering estimated model for ultrasound gel. . . . .	121
Figure 6.16: MRI model 1: The skin-fat inversion results using the real-part based clustering estimated model for ultrasound gel. . . . .	122
Figure 6.17: MRI model 2: The mid-value inversion results using the real-part based clustering estimated model for 80:20 Glycerin/Water solution.	122
Figure 6.18: MRI model 2: The skin-fat inversion results using the real-part based clustering estimated model for 80:20 Glycerin/Water solution. . . . .	122
Figure 6.19: MRI model 2: The mid-value inversion results using the real-part based clustering estimated model for ultrasound gel. . . . .	123
Figure 6.20: MRI model 2: The skin-fat inversion results using the real-part based clustering estimated model for ultrasound gel. . . . .	123
Figure 6.21: MRI model 3: The mid-value inversion results using the real-part based clustering estimated model for 80:20 Glycerin/Water solution.	123

Figure 6.22: MRI model 3: The skin-fat inversion results using the real-part based clustering estimated model for 80:20 Glycerin/Water solution. . . . .	124
Figure 6.23: MRI model 3: The mid-value inversion results using the real-part based clustering estimated model for ultrasound gel. . . . .	124
Figure 6.24: MRI model 3: The skin-fat inversion results using the real-part based clustering estimated model for ultrasound gel. . . . .	124
Figure 6.25: MRI model 1: The complete bone values extraction procedure results using 80:20 Glycerin/Water solution. . . . .	125
Figure 6.26: MRI model 2: The complete bone values extraction procedure results using 80:20 Glycerin/Water solution. . . . .	126
Figure 6.27: MRI model 3: The complete bone values extraction procedure results using 80:20 Glycerin/Water solution. . . . .	126
Figure 6.28: MRI model 1: The line plot representation of the mean value of the real part relative permittivity of bones. . . . .	126
Figure 6.29: MRI model 2: The line plot representation of the mean value of the real part relative permittivity of bones. . . . .	127
Figure 6.30: MRI model 3: The line plot representation of the mean value of the real part relative permittivity of bones. . . . .	127
Figure 7.1: The setting used to measure AquaSonic 100 ultrasound gel dielectric properties. . . . .	135
Figure 7.2: The loads used for calibrating the probe: short-circuit load and distilled water. . . . .	136
Figure 7.3: Relative permittivity values of distilled water: theoretical values versus measurements. . . . .	136

## List of Tables

Table 3.1: Attenuation Coefficient [dB/m] and Skin Depth [cm] for Skin, Fat, and Muscle tissues . . . . .	45
Table 3.2: Bulk Electrical Properties of Regions in the FEM Model . . . . .	47
Table 4.1: Bones mean value real part relative permittivity in MRI model 1. . . .	78
Table 4.2: Bones mean value real part relative permittivity in MRI model 2. . . .	78
Table 4.3: Bones mean value real part relative permittivity in MRI model 3. . . .	78

## **List of Abbreviations**

<b>ABC</b>	Absorbing Boundary Condition
<b>BMD</b>	Bone Mineral Density
<b>BVF</b>	Bone Volume Fraction
<b>CG</b>	Conjugate gradients
<b>CSI</b>	Contrast Source Inversion
<b>DXA</b>	Dual-energy X-ray Absorptiometry
<b>EM</b>	Electromagnetic
<b>FD</b>	Finite-difference
<b>FEM</b>	Finite Element Method
<b>GNI</b>	Guass-Newton inversion
<b>MoM</b>	Method-of-Moments
<b>MR</b>	Multiplicative Regularization
<b>MRI</b>	Magnetic Resonance Imaging
<b>MWI</b>	Microwave Imaging
<b>MWT</b>	Microwave Tomography
<b>OI</b>	Object-of-Interest
<b>PDE</b>	Partial Differential Equation
<b>QCT</b>	Quantitative Computed Tomography
<b>RF</b>	Radio Frequencies
<b>TM</b>	Transverse Magnetic



# **Chapter 1: Introduction**

## **1.1. Scope of Research**

This thesis presents research work in the area of microwave tomography (MWT) for evaluating bones' health via monitoring variations in the bones' dielectric properties. Microwave tomography, in general, is an imaging modality that has been used in various biomedical applications, such as breast cancer detection and brain tumor diagnosis, as well as in industrial non-destructive testing, such as grain spoilage monitoring and structural crack detection. In the application being considered in this thesis, the objective is to illustrate quantitatively changes in the bones' health by reconstructing two-dimensional (2D) tomographic slices of a human leg. These 2D slices will show the main electrical properties (permittivity and conductivity) of bones and tissues surrounding them. Furthermore, changes in the bones' health will manifest themselves as changes in these dielectric properties, which are correlated to the bones' density. Variations in bones' density may arise as a result of low body absorption of calcium, which might be to an underlying deficiency in Vitamin D. Moreover, a decrease in bones' density increases the amount of water/blood content within bone pores, which in turn causes an increase in the electrical properties of bone [1]. Therefore, by using MWT to reconstruct 2D images of a human's leg electrical properties, the health of bone tissues can be monitored.

## **1.2. Motivation**

In the field of medical diagnosis, bone health monitoring is one of the crucial topics with the increase in bone diseases such as osteoporosis. According to the National Osteoporosis Foundation (NOF), more than 10 million people in the United States of America (USA) are affected by osteoporosis, with an additional 33.6 million people suffering from low bone density of the hip [2]. One of the main causes of osteoporosis is Vitamin D deficiency; Vitamin D enables the body to absorb calcium, which is necessary for bones to maintain their health and strength. As reported by the International Osteoporosis Foundation (IOF) [3], the United Arab Emirates (UAE) is one of the top countries with both degeneration cases: Osteoporosis and Vitamin D deficiency. It is estimated that 78% of UAE's population suffers from Vitamin D deficiency, which is

due to several factors such as genetics, lifestyle, low activity, obesity, and cultural dress code and practices.

Currently, the golden standards considered for the assessment of bone mineral density (BMD) are the dual-energy X-ray absorptiometry (DXA) and the quantitative computed tomography (QCT). In these systems, examinations are done for the anatomical structures of the body such as the hip, the spine, and the wrist, where the denser cortical bones are more dominant than the spongy trabecular bones [4]. A major drawback of these systems is their excessive use of ionizing X-ray radiation emitted to human bodies, which may lead to health challenges for long term monitoring. In addition, the overall cost of these machines is considered extremely high [4, 5].

An alternative to the aforementioned techniques is using microwave tomography (MWT) for the diagnosis of human bones health. In comparison to DXA and QCT, MWT emits low-power, non-ionizing electromagnetic radiation onto the objects being imaged. Therefore, monitoring on regular basis using MWT is safe compared to the other techniques, which is important in evaluating the efficiency of long-term treatments of bone osteoporosis. Furthermore, a MWT system is relatively lower in cost and more operator friendly than X-ray based imaging. The advantages that MWT has to offer is the driving force behind the research work conducted in this thesis.

### **1.3. Background**

**1.3.1. Medical imaging.** In 1895, the first medical imaging of human tissues was introduced by Wilhelm Conard with the discovery of X-ray beams emitted from a Crooke's tube [6]. Ever since, the quality of health care services provided to patients has been improving significantly. Medical imaging refers to the process of analyzing the functionality of biological tissues and organs non-invasively by creating visuals that represent their structures [7]. In addition to acquiring images, the latest medical imaging modalities also provide various image processing, recording, and storing techniques. Such techniques allow a physician, who is usually a radiologist, to observe various valuable outcomes related to the health conditions of patients, and thus diagnose them properly. To support the decision of the radiologist, modern diagnostic imaging

modalities have been developed to assist in the process of decision making using computerized analysis [8], which is performed using image processing techniques.

Several imaging modalities are commonly used now-a-days by clinicians in the diagnosis and treatment of patients such as X-ray computed tomography (CT) scans, magnetic resonance imaging (MRI), and ultrasound. The computed tomography modality obtains several slices for a certain organ allowing for the possibility of merging all the other slices together to form a three-dimensional (3D) image. X-ray CT scans demonstrate high resolution accompanied with high quality of the imaging of soft tissues within the body, like muscles and organs. However, the high dose of X-ray beams emitted into the body per scan can increase the possibility of causing cancer in the future [9, 10]. In contrast, MRI does not employ a high dose of ionizing radiations to obtain images of biological structures. Instead, three-dimensional images are created from the utilization of magnetic fields at radio frequencies (RF) waves directed to the body. Nevertheless, MRI imaging requires around an hour to complete each scan, and its equipment is considered very expensive compared to other imaging systems. Another common imaging modality is ultrasound imaging, which is a non-ionizing technique that depends on the use of acoustic waves generated from piezoelectric materials. Based on the reflections of these sound waves, images are reconstructed in a real-time imagery manner [7, 11]. Ultrasound imaging is considered very efficient when it comes to hard tissues like bones, but it is actually weak in terms of resolution when dealing with soft tissues [9]. Further, in addition to 2D and 3D imaging systems, imaging in a one-dimensional (1D) form is often possible to determine the location of certain body organs and tissues functionality over time such as the brain, muscles, and heart. This is commonly done using data recording techniques. Examples of 1D imaging techniques are Electroencephalography (EEG) of the brain, Electromyography (EMG) of muscles, and Electrocardiography (ECG) of the heart [11].

**1.3.2. Microwave imaging.** In addition to the modalities discussed in the previous section, many modern medical imaging modalities are still being developed. An example of such modalities is microwave imaging (MWI), which can be either radar-based or tomographic based imaging. Microwave Imaging (MWI) uses electromagnetic

(EM) waves in the microwave spectrum, whose frequency range is in between 300 MHz and 300 GHz; this corresponds to a wavelength range from 1 m to 1 mm in free-space. It was proposed in 1979 with the first imaging experiments on kidneys by Larsen and Jacobi [9, 12], where they were able to distinguished various tissues within the kidney such as the cortex corticis, the deeper cortical layers, the medullary outer zone containing loops of henle, and the calyces region. Further research in MWI emerged again after the huge development of computers and algorithms. Researchers consider it as a promising imaging technique in the field of medicine, as it does not transmit harmful waves into the body [1, 9, 13]; MWI uses low-power non-ionizing electromagnetic radiation. This modern modality is a cost-effective one when compared to other commonly-used imaging modalities, as it does not require expensive equipment to be built and used.

Microwave imaging systems are either radar-based or tomographic-based. In radar-based systems, the transceiver transmits an ultra-wide band (UWB) signal into a human organ, and then receives it back as a reflection. The locations of certain tissues or cancer cells are represented by reconstructed images with higher reflection values relative to other normal tissues [14]. Such image details are considered qualitative, as radar systems identify a tumor based on the strength of the reflected electromagnetic waves at certain locations. On the other hand, a microwave tomography-based system conducts the imaging of organs in a slice-by-slice manner, much closer to the methodology of X-ray CT scans. It represents more quantitative details about tissues, reconstructing images based on the scattered electromagnetic waves measured at the receivers. The measured signals are processed using optimization algorithms that creates a dielectric properties map corresponding to various regions within the imaging chamber. Tomographic-based systems show a high efficiency when detecting very small tissues, which is usually lacked in radar-based systems [14, 15].

The complete microwave tomography system, which is the selected system for this thesis research, consists of an antenna array surrounding an object-of-interest (OI) being imaged. As shown in Fig. 1.1, the object of interest (OI) is located at the middle of the imaging chamber, surrounded by the antenna array. The elements of the antenna array acts as transmitters and receivers interchangeably. Each antenna in the

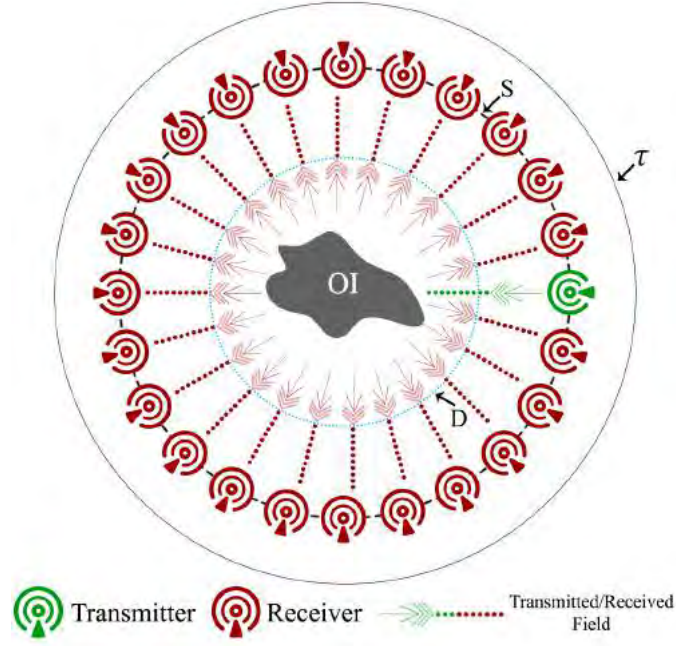


Figure 1.1: Microwave tomography system configuration.

array transmits an electromagnetic signal at a time, while the rest of the antennas act as receivers. This setup is located within an imaging chamber with the OI immersed inside a matching medium in order to reduce any signal losses caused by difference in electrical properties between the OI and the medium surrounding it [13]. As shown in Fig. 1.1, domain  $D$  represents the imaging domain, which is the imaging region of the system, surface  $S$  depicts the boundary where the antennas are located surrounding the OI, and  $\tau$  is the boundary of the imaging chamber.

It worth mentioning that  $D$ ,  $S$ , and  $\tau$  are not necessarily circular. They can be modified to follow any shape decided by the user. For example, the antennas locations may follow the boundaries of the OI being imaged. Furthermore, the imaging domain can be fixed to cover only the OI region, which can reduce the overall image reconstruction time. However, commonly circular boundaries are followed by most researchers for its simplicity. Moreover, the overall design of the MWT system allows it to be portable, which means that it can be used both inside and outside the clinic.

Compared to other imaging modalities, MWT systems lack the high spatial resolution provided by X-ray CT or MRI images, as they only image the bulk features of biological organs providing a map for their electrical properties. Each human tis-

sue is characterized by its own relative permittivity ( $\epsilon_r$ ) and conductivity ( $\sigma$ ), which is a function of the frequency of the electromagnetic wave transmitted to it [13]. The electrical properties of human tissues has been measured and presented by C. Gabriel *et al.* for various in-vivo and in-vitro experiments [16]. The performed measurements demonstrated differences between healthy and cancerous tissues, which will result in a contrast in the images reconstructed using MWI. According to various studies, a tumor tissue causes more electromagnetic waves to be scattered than the healthy tissues; this indicates higher permittivity values for tumorous regions, which is used to identify the location of a tumor in MWI [13, 15].

The overall simulations and reconstruction procedures for microwave imaging systems consist of a forward problem and an inverse problem. In the forward problem, the main goal is to find the total electric field that results from the scattering of the incident field in the presence of an object-of-interest; information about the electrical properties of the OI is known. There are various ways to solve the forward problem using electromagnetic computational techniques such as the finite-element method (FEM), the method-of-moments (MoM), and finite-differences (FD). In the inverse problem, the object's electrical properties, the relative permittivity and conductivity, are estimated based on the measurements of the scattered electric field at receiver locations [17]. There are various algorithms that are commonly used to solve MWI inverse problems, which include the contrast Source inversion (CSI), Guass-Newton inversion technique (GNI), and modified conjugate gradients (CG) methods. In this thesis, the forward problem will be solved using the finite-element method to create synthetic data (numerically-generated experimental data), whereas the inverse problem is solved using the contrast source inversion technique.

**1.3.3. Anatomy of human leg bones.** Similar to the other organs of the human body, the lower extremity comprises of various biological tissues such as the bones, muscles, fat, skin, ligaments, tendons, joints, nerves, and blood vessels. However, because the core of this thesis focuses on bone imaging, the presented work will concentrate on the lower extremitys bones anatomy. In general, the main functionality of human bones is to provide support and protection for the whole human body. Specifically-

speaking, the shape of each skeleton bone usually reflects its nature of functionality; for instance, the brain is enclosed within skull bones for the purpose of protection, while the leg consists of long bones for locomotion support [18]. In addition, bones have a precious property which is managing the process of mineral homeostasis and blood cells formation in the human body. Furthermore, the bone marrow is responsible of storing fat inside the internal bone cavities to be used whenever the body needs it. Regarding minerals, such as calcium and phosphorus, they are stored in the bone tissues themselves where hormones manage their movement back and forth between bones and the blood according to the body's need. Calcium is deposited as salt within bone tissues with a small amount stored as  $Ca^{2+}$  cations in the blood. These stored minerals are vital for the body's signal transmission performed by its nervous system, for the contraction of muscles, and for blood clotting. Thus, the bone is considered by itself a living organ formed as a connective tissue in the body [18, 19].

Some of the very important bones in the human body are the lower limb bones located within the human appendicular skeleton. These bones are mainly the femur, patella, tibia, fibula, and the foot bones. Actually, being at the bottom part of the body, the location of these bones gives them the essential functionality of carrying the whole body and enduring its pressure. Considering the leg bones in particular, the fibula and

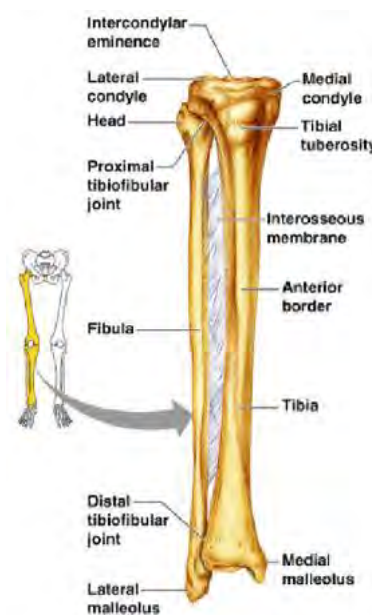


Figure 1.2: Leg bones structure and anatomy. retrieved from [19].

tibia bones are shown in Fig. 1.2. The fibula is the smaller bone located at the lateral part of the leg, while the tibia is the bigger bone located at the medial part of the leg. The proximal and distal parts of both bones, located near the joints, consist mostly of trabacular or spongy bones. Most of the area of these bones is covered by the compact bones, with a cavity inside each bone including the bone marrow. These compact bones have high density and less pores compared to the spongy bones that have the appearance of a sponge with lots of pores. Both types of bones are of a high importance to the body, as the compact bones provide the strength needed for protection and support while the spongy bones include pores that store blood and marrow allowing the exchange of minerals and liquids in and out of the bone [19]. Each type of bones, the compact and the spongy, should maintain a stable level in a healthy strong human body in order to perform their utmost functionality [19].

In Fig. 1.3, an illustration of the cross-sectional view of the human leg that contains the tibia and fibula bones along with the other surrounding tissues is shown. The Tibialis Anterior muscle covers and supports the lateral surface of the tibia, leaving the other medial surface totally exposed to fat and skin layers, which causes much harm when the skin is bumped. On the other hand, the fibula is completely enclosed by muscles named the Fibularis Brevis and Longus muscles [18–20]. It is worth mentioning

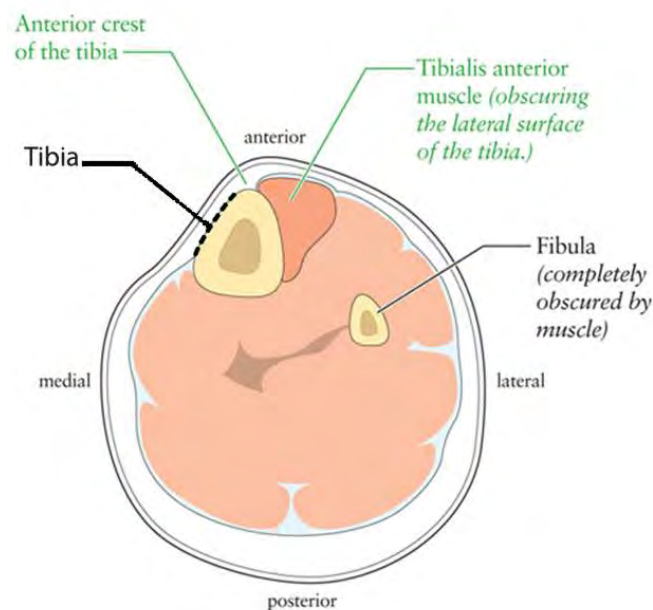


Figure 1.3: Cross-sectional view of the leg structure. retrieved from [20].



here that the fat layer is thicker on the posterior part of the leg, and it varies from one human to another. As stated earlier in this section, the other tissues included in the body's lower extremity are not of our interest. This is due to the fact that microwave imaging does not have the capability of detecting very small components within the leg; it only captures the bulk parts such as bones, muscles, fat, and the skin [13].

**1.3.4. Vitamin D and bone volume fraction (BVF).** Vitamin D was first identified back in 1921 for its major role in calcium homeostasis. This vitamin consists of two forms; Vitamin  $D_2$  (ergocalciferol) and  $D_3$  (cholecalciferol). The major sources of Vitamin  $D_2$  are vegetables and oral supplements. On the other hand, Vitamin  $D_3$  can be obtained from the exposure to ultraviolet B (UVB) radiations from the sun, oily fish, fortified food such as milk, yogurts, cereals, and other oral supplements [21]. Both types of Vitamin D are absorbed by the intestine and metabolized in the liver as 25-hydroxyvitamin D [ $25(OH)D$ ], known as calcidiol. The active form of the vitamin, 1,25-dihydroxyvitamin D [ $1,25(OH)_2D$ ] (calcitriol), is then created by the kidney by the enzyme  $1\alpha$ -hydroxylase [21, 22]. To measure Vitamin D level, a blood serum is taken any time of a day from the patient. The blood serum provides an indication about the concentration of 25-hydroxyvitamin  $D_3$ , as it has been proven the Vitamin  $D_3$  is used more than Vitamin  $D_2$  by the body [22].

Vitamin D is mainly responsible for managing the absorption of calcium within the intestine. Therefore deficiency in Vitamin D may cause a decrease in the amount of calcium supplied to bones, which can lead to lowering the bones' density. Lower density results in decrements in the amount of bone minerals and bone mass [23], which is critical to the human's health. In addition, having deficiencies in calcium levels within the blood could be accompanied usually with a lower BMD and low-impact skeletal fractures. Further, patients with Vitamin D deficiency show other symptoms such as hypocalcemia and/or hypophosphatemia, low 24-hour urine calcium excretion rate, and low levels of total  $25(OH)D$  [22].

To elaborate more on the BMD, the metric bone volume fraction (BVF) is commonly used to represent the mass and quality of bone in patients. BVF represents the

volume of the mineralised bone per unit volume of the sample [24] and can be mathematically calculated as,

$$\text{BVF} = \frac{\text{Bone Volume (BV)}}{\text{Total Sample Volume (TV)}}. \quad (1)$$

It is usually represented as a percentage value. In a case of Vitamin D deficiency, bones are expected to be osteoporotic, which means they have more pores due to lack of minerals. Thus, the overall percentage of BVF would be less compared to healthy and stable patients. This factor is used to evaluate the treatment process of bone fragility by comparing the supplement efficiency after the course intake.

BVF can be determined either non-invasively or invasively. The two main methods to determine the quality of the bone non-invasively are the DXA and  $\mu\text{QCT}$ . DXA provides a non-volumetric measurement of bone quantity per scan area, as it measures only the areal bone mineral density in  $\text{gcm}^2$ . On the other hand, in  $\mu\text{QCT}$ , a volumetric density assessment in  $\text{gcm}^3$  is provided with a voxel size of  $500 \mu\text{m}$  [24, 25]. To determine BVF invasively, a bone specimen with void spaces is immersed in distilled water for a few hours, and then the mass of absorbed water,  $W_f$ , in grams is found as

$$W_f = W_W - W_D. \quad (2)$$

Here  $W_W$  is the overall weight of the sample after immersion and  $W_D$  is the weight of actual bone specimen. Next, the void volume,  $V_P$ , is calculated as  $V_P = W_f/0.9971$ . Then, the porosity of the bone is calculated as  $P = V_P/V_T$ , where  $V_T$  is the bone's total volume. Finally, BVF is given as  $1 - P$ . The details of this procedure are outlined here [26].

#### 1.4. Current State-of-Art in MWT

Microwave tomography has been investigated in various biomedical applications such as brain stroke detection, breast cancer monitoring, bone and lung imaging. Here, some examples from the literature are outlined.

S. Semenov *et al.* [27] investigated the possibility of using microwave tomography for the detection of brain stroke in a 2D model, given that the brain is shielded by tissues of high dielectric properties contrasts which are the skull and the Cerebrospinal

fluid. A 2D model was created for the brain surrounded by 32 dipole antennas that act as transmitters and receivers, working at a frequency of 0.5–2 GHz. The utilized image reconstruction algorithms were a non-linear Newton approach for single- and dual-frequency values, along with a multiplicative regularized contrast source inversion (MR-CSI) algorithm. It was found that the MWI system detected the stroke location as white circles within the created model. Moreover, the dual-frequency approach improved the image reconstruction outcomes. I. Sarwar *et al.* [28] proposed an algorithm for microwave imaging systems to monitor brain stroke using a programmable system-on-chip. The calculations are done using a Field-Programmable Gate Array (FPGA), which provided them with a  $5\times$  speed increase in calculations compared to running the inversion algorithms on a computer workstation. Their inversion algorithm is based on Born approximations, with the data collected from their MWT system consisting of 24 transmitters and receivers connected to an RF switch and Vector Network Analyzer (VNA).

In the area of breast cancer detection, A. Golnabi *et al.* [29] developed an algorithm to reconstruct accurate 3D images of a breast shaped phantom simulating a cancerous region. In the proposed system, 16 monopole antennas located on two movable plates were used for the imaging procedure at a frequency range from 0.3–3 GHz. The movable plates were used in order to image the phantom when all antennas were at the same level (2D in-plane) or at different heights (3D planes). The matching medium used was mixture of 80:20 ratio of glycerin and water. This technique utilized the finite difference time domain (FDTD) method for the calculations of the forward problem, and Gauss-Newton iterative approach for the inverse problem. A 3D view of the breast with the simulated cancer was obtained, in addition to 2D slices at various heights of the breast phantom. This algorithm imaged the breast phantom successfully estimating the dielectric properties of the various tissues within the simulated breast. Golnabi's research demonstrated the possibility of using 3D MWI in breast cancer diagnoses.

Bone imaging has received attention in microwave imaging through the work of P. M. Meaney *et al.* [1]. They investigated the relation between microwave dielectric properties and bulk bone density measurements. They found that there is a strong correlation between permittivity and conductivity values and Bone Volume Fraction

(BVF). Their in-vitro research discovered that whenever the BVF drops, that is a drop in bone density, the dielectric properties increase. Thus, they were able to detect such differences in the re-constructed images to represent them as variation in bone density measurements. In addition, C. Gilmore et al. [9] explored the possibility of imaging human bones within limbs in in-vivo experiments, where 24 dipole antennas working in the frequency range of 0.8–1.2 GHz were located inside a water and salt matching fluid. The forward problem was solved using FEM to measure the incident, total, and scattered electric fields. The inverse problem was solved using the contrast source inversion (CSI) algorithm. To conduct the experiment,  $24 \times 23$  data points were collected per volunteer at various frequencies and the reconstruction procedure was performed both with and without prior information about the background medium. It was found that the less adipose the layer thickness within the limb, the better the dielectric properties profile of the reconstructed image, showing accurate detection of two bones within the limbs. In addition, prior information used before the reconstruction process that is related to the thickness and dielectric properties of the adipose layer improved the images obtained. The system succeeded in detecting the two bones within the limb, ulna and radius, providing values of permittivity and conductivity close to those reported in the literature. This research opened the gate toward MWI for bone health analysis and treatment monitoring applications.

Most recently, image enhancement algorithms has been integrated within the inversion algorithm to improve the contrast in MWT images. A. Zamani *et al.* [30] developed an algorithm that can significantly improve the performance of microwave imaging systems. Their research focuses at the boundary identification of the object of interest. By measuring variations in the resonant frequency of the antennas surrounding the OI, the boundaries of the OI can be detected and incorporated into the inversion algorithm. To test their algorithm, simulations of human trials for torso imaging were conducted; their focus was to use radar-based MWI system to detect the location of lung cancer. Their MWI system operated in the frequency range of 0.75–1.75 GHz, with 12-element antenna array surrounding the OI. Their results have showed significant improvements to the image reconstruction process. In another application, M. Omer *et al.* [31] extracted prior information about the OI structure by integrating the

results of an ultrasound imaging system. Ultrasound transducers provide fine structural details of various regions within the OI, which was in this research the breast. To extract regions, k-means clustering algorithm was utilized to segment the image into various segment representing tissues. These segments are incorporated into a time-delay computation that discretize the clustered image into reconstruction positions. They have successfully showed improved detection of tumor when prior information are incorporated in MWI simulations. Further, L. Guo *et al.* [32] used k-means clustering along with support vector machine (SVM) method to localized stroke in phantoms. Their research was to localize and classify stroke types based on the reconstructed tomographic images. The Born iterative method was used to obtain the dielectric properties with 36 dipole antennas operating at 0.85 GHz. K-means clustering segmented the resulting images into three clusters, one of which may include the stroke. Using SVM, stroke was classified after training the classifier. Their algorithm have provided a 91% sensitivity and 87% specificity when localizing brain tumors.

These research works introduced new technique to enhance the reconstruction of MWT images. Thus, further investigations are carried on from this point in this thesis work.

### **1.5. Thesis Problem Statement**

In literature, it was shown that the de-mineralization processes affect the overall bone quality and strength, which in turn affect the interaction between the biological tissues and the electromagnetic waves. This is depicted through variations in the relevant dielectric properties and can be monitored from the images reconstructed by a MWI system [1, 26]. In addition, several tests were done on bone volume fraction (BVF) [1] have showed that the BVF is inversely proportional to the dielectric properties such that the lower the fraction, the higher the values of the tissues dielectric properties. All these discussions drag the attention toward Vitamin D treatment monitoring applications which, to the best of our knowledge, have not yet been explored, especially that there is indeed a strong correlation between amount of minerals in bones and the bones' electrical properties [1, 33]. Having said that, the aim of this thesis is to explore the feasibility of using microwave tomography (MWT) in diagnosing human bone health under certain conditions. In addition, through simulations, the optimum

parameters and settings, which best represent an actual microwave tomography system, are identified. Based on previous research [30–32], it was shown that changing the location of different imaging boundaries affects the efficiency of reconstruction. Therefore, the effect of varying different parameters related to microwave tomography is explored and evaluated based on the inversion algorithm reconstructions quality. In addition, an image processing approach is followed to extract useful information from the reconstructed images in order to be used for the image enhancement process. All these objectives are directed toward building a smart wearable microwave system for bone health monitoring applications in the future.

## **1.6. Thesis Outline**

In Chapter 2, the mathematical formulation of the forward problem as well as the inverse problem are presented. The forward problem is solved for two-dimensional transverse magnetic electromagnetic problems using the finite-element method. The inverse problem is solved using the finite-element contrast source inversion method.

In Chapter 3, the complete procedure followed to simulate an actual microwave tomography system is presented. Three finite element meshes representing three human cross-sectional leg models were created; these leg models having varying fat thickness. Next, the forward problem is simulated for a chosen set of parameters; the forward problem is simulated several times for bones with varying values of electrical properties. Moreover, the synthetic data calculated using the forward problem simulations are imported to the inversion algorithm to estimate a relative complex permittivity map for the object-of-interest (OI) located within an imaging domain. The results for the inversion problem are shown for healthy as well as unhealthy bones.

In Chapter 4, an enhancement process is followed to improve the reconstruction of the relative permittivity complex map of the OI. Several parameters are investigated including incorporating prior information about the OI structure and dielectric properties, varying the size of imaging domain, relocating the antennas surrounding the OI, and using a different matching media.

In Chapter 5, an image processing approach is provided to extract structural information from the blind inverted images. The structural information are used to estimate the OI boundaries, to be further utilized for for in the enhancement process.

In Chapter 6, the effect of varying bone health according to its BVF is explored. Bone health conditions are taken under five BVF scenarios. For each BVF scenario, the blind inversion along with the enhancement procedure are followed and discussed briefly. The changing pattern of bone density in terms of real part relative permittivity values is represented as line plots and analyzed.

The thesis is concluded in Chapter 7, followed by prospects for future work.

## Chapter 2: Mathematical Formulation and Numerical Modeling

In this chapter the mathematical formulation of the forward problem as well as the inverse problem are presented. The forward problem is solved for two-dimensional transverse magnetic electromagnetic problems using the finite-element method. The inverse problem is solved using the finite-element contrast source inversion method. For both the forward and inverse problems, the electromagnetic problem is solved within the framework of contrast sources, which is explained in this chapter.

### 2.1. The Forward Problem

In the forward problem, the main objective is to determine the electric field intensity strength at different locations  $\vec{r} = (x, y, z)$  within a microwave imaging chamber. In Cartesian coordinates, the electric field inside the chamber will have three vector components such that,

$$\vec{E}(\vec{r}) = E_x(\vec{r})\hat{a}_x + E_y(\vec{r})\hat{a}_y + E_z(\vec{r})\hat{a}_z, \quad (3)$$

where  $(\hat{a}_x, \hat{a}_y, \hat{a}_z)$  are the unit vectors in the  $(x, y, z)$  coordinates respectively.

Furthermore, in this work the electric field is considered to have time-harmonic dependency of  $\exp(j\omega t)$  where  $j = \sqrt{-1}$  given an angular frequency  $\omega = 2\pi f$  for a frequency  $f$ .

Next, the electric field inside the chamber can be of three types. Given a transmitter  $t$ , the first kind is the incident field  $\vec{E}_{\text{inc},t}$ , which is the electric field generated by source in the absence of an object-of-interest (OI). The second type is the total electric field  $\vec{E}_{\text{tot},t}$ , which is the electric field intensity in the presence of the OI within the chamber. The third field is the scattered electric field  $\vec{E}_{\text{scat},t}$ , which is the electric field scattering effect caused by the OI itself [13]. By measuring the incident and total fields at the receivers within the chamber, the scattered electric field can be simply calculated as,

$$\vec{E}_{\text{scat},t} = \vec{E}_{\text{inc},t} - \vec{E}_{\text{tot},t} \quad (4)$$

Mathematically, the time-harmonic electric fields inside the imaging chamber can be modeled using Helmholtz vector wave equations. Helmholtz wave equations are



second-order differential equations, which can be used to solve for the electric fields given the appropriate boundary conditions. For a source  $t$ , the incident electric field inside an imaging chamber is a solution for the following Helmholtz equation,

$$\nabla \times \nabla \times \vec{E}_{\text{inc},t}(\vec{r}) - k_b^2(\vec{r})\vec{E}_{\text{inc},t}(\vec{r}) = -j\omega\mu_0\vec{J}_t(\vec{r}). \quad (5)$$

Here  $\vec{r}$  is a position vector,  $k_b$  is the wavenumber of the matching medium (background) within the chamber,  $\mu_0 = 4\pi \times 10^{-7}$  [H/m] is the magnetic permeability of free-space,  $\vec{J}_t$  is the electric current density that is used to model transmitter  $t$ . The wavenumber  $k_b$  has units of [rad/m], and is calculated as

$$k_b = 2\pi f \sqrt{\mu_0 \epsilon_0 \epsilon_b(\vec{r})}, \quad (6)$$

where  $\epsilon_0 = 8.854 \times 10^{-12}$  [F/m] is the electric permittivity of free-space and  $\epsilon_b$  is the relative complex permittivity of the background medium.

In regard to the total field, it is the solution for the following Helmholtz second-order differential equation,

$$\nabla \times \nabla \times \vec{E}_{\text{tot},t}(\vec{r}) - k^2(\vec{r})\vec{E}_{\text{tot},t}(\vec{r}) = -j\omega\mu_0\vec{J}_t(\vec{r}). \quad (7)$$

Here  $k = 2\pi f \sqrt{\mu_0 \epsilon_0 \epsilon_r(\vec{r})}$ , where  $\epsilon_r$  is the relative complex permittivity at any location inside the chamber in the presence of the OI. For both the background and OI, the relative complex permittivity is defined,

$$\begin{aligned} \epsilon_r(\vec{r}) &= \epsilon_r'(\vec{r}) - j\epsilon_r''(\vec{r}) \\ &= \epsilon_r'(\vec{r}) - \frac{j\sigma_{\text{eff}}(\vec{r})}{2\pi f \epsilon_0}. \end{aligned} \quad (8)$$

Here  $\epsilon_r'$  is the dielectric constant of a material and  $\sigma_{\text{eff}}$  is a material's effective conductivity. The dielectric constant is a measure of the material's ability to store electrical energy relative to free-space, whereas conductivity is a measure of the material's capability to conduct electricity.

Using the definition in equation (4) along with the equations (5) and (7), it can be shown that the scattered field is the solution of the following equation,

$$\nabla \times \nabla \times \vec{E}_{\text{scat},t}(\vec{r}) - k^2(\vec{r})\vec{E}_{\text{scat},t}(\vec{r}) = (k^2(\vec{r}) - k_b^2(\vec{r}))\vec{E}_{\text{inc},t}(\vec{r}). \quad (9)$$

Next, let the contrast within the chamber be defined as,

$$\chi(\vec{r}) = \frac{\epsilon_r(\vec{r}) - \epsilon_b(\vec{r})}{\epsilon_b(\vec{r})}. \quad (10)$$

The contrast function is used to determine the *contrast* level or relative difference in electrical properties between a point located in the OI with a certain permittivity value  $\epsilon_r(\vec{r})$  and a matching medium of a permittivity of  $\epsilon_b(\vec{r})$ . Outside the domain of the OI,  $\chi(\vec{r}) = 0$ . Using the definition of the contrast, the scattered field equation (9) can be rewritten as

$$\nabla \times \nabla \times \vec{E}_{\text{scat},t}(\vec{r}) - k_b^2(\vec{r})(\chi(\vec{r}) + 1)\vec{E}_{\text{scat},t}(\vec{r}) = k_b^2(\vec{r})\chi(\vec{r})\vec{E}_{\text{inc},t}(\vec{r}). \quad (11)$$

Further, the contrast source can be defined as

$$\vec{w}_t(\vec{r}) = \chi(\vec{r})\vec{E}_{\text{inc},t}(\vec{r}). \quad (12)$$

Using the contrast source definition, the scattered field equation can be written as,

$$\nabla \times \nabla \times \vec{E}_{\text{scat},t}(\vec{r}) - k_b^2(\vec{r})\vec{E}_{\text{scat},t}(\vec{r}) = k_b^2(\vec{r})\vec{w}_t(\vec{r}). \quad (13)$$

The contrast source  $\vec{w}_t(r)$  resembles a current source located in the scatterer object at position  $\vec{r}$ . It produces the scattered field in the microwave imaging environment with the background medium of  $\epsilon_b$ , and it is used in the inverse problem analysis.

In this thesis, the FEM 2D-TM solver is used to generate synthetic data (numerical experimental values) for different models and MWT configurations.

## 2.2. Two-Dimensional Transverse Magnetic Approximation

In the work presented in the thesis, the transverse magnetic (TM) approximation is used. In TM approximation, the electric field has only one longitudinal component in the  $z$ -direction, with magnetic field having two transverse components in the  $(x - y)$  plane, such as to satisfy Maxwell equations.

This approximation is considered because it is assumed that the electrical properties as well as the electric fields are not changing with respect to the  $z$ -direction. Moreover the electric fields are assumed to be  $z$ -polarized with no transverse components in the  $(x - y)$  plane. Therefore, this means that for a position vector  $\vec{r} = (x, y)$ , the fields  $\vec{E}_{\text{inc},t}$ ,  $\vec{E}_{\text{tot},t}$ , and  $\vec{E}_{\text{scat},t}$  are written as,

$$\begin{aligned}\vec{E}_{\text{inc},t}(\vec{r}) &= E_{\text{inc},t,z}(\vec{r})\hat{z}, \\ \vec{E}_{\text{tot},t}(\vec{r}) &= E_{\text{tot},t,z}(\vec{r})\hat{z}, \\ \vec{E}_{\text{scat},t}(\vec{r}) &= E_{\text{scat},t,z}(\vec{r})\hat{z}.\end{aligned}\tag{14}$$

Using the TM approximation, it can be shown that equations (11) and (13) can be given as

$$\nabla^2 E_{\text{scat},t,z}(\vec{r}) + k_b^2(\vec{r})(\chi(\vec{r}) + 1)E_{\text{scat},t,z}(\vec{r}) = -k_b^2(\vec{r})\chi(\vec{r})E_{\text{inc},t,z}(\vec{r}),\tag{15}$$

and

$$\nabla^2 E_{\text{scat},t,z}(\vec{r}) + k_b^2(\vec{r})E_{\text{scat},t,z}(\vec{r}) = -k_b^2(\vec{r})w_{t,z}(\vec{r}).\tag{16}$$

These two equations are known as the scalar Helmholtz equations.

To solve these second-order differential equations, the appropriate boundary conditions (BCs) need to be defined at the boundaries of the imaging chamber problem domain.

If the imaging chamber boundary is a conductive enclosure, the perfect electrical conductor (PEC) boundary conditions are used, resulting in homogeneous Dirichlet BCs,

$$E_{\text{scat},t,z}(\vec{r} \in \Gamma) = 0.\tag{17}$$

Here  $\Gamma$  represents points at the boundary of the chamber.

On the other hand, in some microwave tomography systems, the chamber boundaries can be assumed to extend to infinity under two conditions. These conditions are: (i) the reflections from the chamber boundaries can be ignored, and/or (ii) there is a lot of loss in the matching medium itself such that little electric fields are reflected back from the chamber walls. Under these conditions, the fields in the model will satisfy the Sommerfeld radiation condition given as,

$$\lim_{r \rightarrow \infty} \sqrt{r} \left( \frac{\partial}{\partial r} E_{\text{scat},t,z}(\vec{r}) + jk_b E_{\text{scat},t,z}(\vec{r}) \right) = 0. \quad (18)$$

Here  $r$  is the magnitude of the position vector  $\vec{r}$  for points located at the boundary of the chamber.

### 2.3. The Finite Element Method (FEM)

In the work presented herein, the TM scattered field equations defined in (15) and (16) are solved numerically using the finite-element method (FEM).

The finite element method (FEM) is a frequency-domain numerical technique that divides any space domain into several discrete elements. At each of these elements, the second-order differential equations are solved in a numerical manner to calculate specific quantities [34]. A. Winslow was the first to use FEM to solve for magnetic fields on an irregular mesh for practical experiments [35].

Further, FEM is used in the discretization of partial differential equations (PDEs) for solving electromagnetic problems. These PDEs are the Helmholtz equations, which are used to determine the scattered electric field intensity within a domain [36]. For microwave imaging (MWI) systems, given a domain that encloses an object of interest (OI), to solve for the electric fields using FEM, this domain is segmented into a mesh of triangles. Each triangle will have electric properties associated with them depending on their location in the mesh. Further, the mesh is characterized by  $N$  number of nodes, and  $T$  triangles that are connected with no gaps in between them. After creating the mesh, FEM is used to solve for the scattered electric field at each node of the triangles within this mesh. In MWI, FEM is used to solve the fields for both the forward and inverse problems.

In the proposed work, a 2D TM FEM solver developed by A. Zakaria [36] in MATLAB will be utilized. Within the framework of FEM, the Helmholtz equations (15) and (16) are given as

$$\underline{E}_{\text{scat},t,z} = \mathcal{L}_\chi [\underline{E}_{\text{inc},t,z}], \quad (19)$$

and

$$\underline{E}_{\text{scat},t,z} = \mathcal{L} [\underline{w}_{t,z}]. \quad (20)$$

The variables and operators in equations (19) and (20) are, respectively, complex ( $\mathbb{C}$ ) vectors and matrices, and are defined as follows,

- $\underline{E}_{\text{scat},t,z} \in \mathbb{C}^N$  is a vector of size  $N$  for the values of the scattered electric fields  $z$ -component calculated at the nodes of a triangular mesh.
- $\underline{E}_{\text{inc},t,z} \in \mathbb{C}^N$  is a vector of size  $N$  for the incident field values due to a transmitter  $t$ , computed analytically at the nodes of the triangular mesh.
- $\mathcal{L}_\chi \in \mathbb{C}^{N \times N}$  is an FEM matrix operator. This operator contains information about the contrast  $\chi$  within the imaging domain along with information about the boundaries of the problem domain.
- $\underline{w}_{t,z} \in \mathbb{C}^N$  is a vector of size  $N$  for the values of the contrast sources with respect to transmitter  $t$  within the imaging domain.
- $\mathcal{L} \in \mathbb{C}^{N \times N}$  is an another FEM matrix operator. This operator contains information about the problem's boundary and matching medium.

The matrix operators  $\mathcal{L}_\chi$  and  $\mathcal{L}$  depend on the basis functions used to discretize the problem domain as well as on the geometrical information of the nodes and triangles in the mesh. The derivation of these operators are beyond the scope of this thesis and it has been outlined in details in [36].

#### 2.4. Solving the Inverse Problem

In the inverse problem, the main goal is to use the information obtained about the scattered electric field  $\vec{E}_{\text{scat},t}$  at the receivers surrounding an object to reconstruct a quantitative image. This image estimates the relative complex permittivity distribution within the object along with the object's location inside the imaging domain  $D$  located inside the MWI chamber.

The inverse problem is a mathematically challenging problem as it is ill-posed due to several reasons. First, the solution for the inverse problem is non-unique; that is there might be more than one solution for the same problem. Secondly, the problem is not stable; small changes in the measured electric field results in large changes in the reconstructed image. Finally, a solution might not exist as the optimization algorithm solving the problem might not converge. In order to tackle these mathematical challenges, specialized optimization algorithms on conjunction with regularization techniques can be utilized [13,36]. In this thesis, the contrast source inversion technique with multiplicative regularization will be used [36].

**2.4.1. The contrast source inversion.** The contrast source inversion is a nonlinear optimization algorithm that was developed P. M. van den Berg in 1997 [37]. In contrast source inversion (CSI), two variables, the contrast  $\chi$  and the contrast source  $\vec{w}_t$ , are updated successively to minimize a cost function  $C^{\text{CSI}}(\chi, \vec{w}_t)$ . This cost function is given as

$$C^{\text{CSI}}(\vec{w}_t, \chi) = \frac{\sum_{t=1}^T \|\vec{u}_t(\vec{r}') - \mathcal{G}_S(\vec{w}_t(\vec{r}))\|_S^2}{\sum_{t=1}^T \|\vec{u}_t(\vec{r}')\|_S^2} + \frac{\sum_{t=1}^T \|\chi \vec{E}_{\text{inc},t}(\vec{r}) - \vec{w}_t(\vec{r}) + \chi \mathcal{G}_D(\vec{w}_t(\vec{r}))\|_D^2}{\sum_{t=1}^T \|\chi(\vec{r}) \vec{E}_{\text{inc},t}(\vec{r})\|_D^2}. \quad (21)$$

In this cost function, the variables are defined as,

- $S$  is the measurement domain that contains the receivers at location  $\vec{r}'$ .
- $D$  is the imaging domain that contains the object-of-interest. A location inside the imaging domain is defined using the position vector  $\vec{r}$ .
- $\vec{u}_t(\vec{r}')$  is the electric fields measured at the receivers.
- $\vec{w}_t(\vec{r})$  and  $\chi(\vec{r})$  are the contrast sources and contrasts, respectively, within the imaging domain.
- $\vec{E}_{\text{inc},t}(\vec{r})$  is the incident field defined inside the imaging domain.
- $\mathcal{G}_S$  is a mathematical operator that uses the values of the contrast source  $\vec{w}_t(\vec{r})$  to calculate the scattered field at the receiver locations.
- $\mathcal{G}_D$  is a mathematical operator that uses the values of the contrast source  $\vec{w}_t(\vec{r})$  to calculate the scattered electric field inside the imaging domain.

In the cost function,  $\|\cdot\|^2$  is  $L_2$ -norm or Euclidean norm.

**2.4.2. FEM-CSI.** The contrast source inversion (CSI) method has been developed within the framework of the finite-element method (FEM) by Zakaria et al. [36]. The use of FEM to develop CSI offers several advantages in comparison to other conventional techniques [36]. One advantage is the ability to incorporate inhomogeneous medium as a background reference; this improves the quality of the algorithm reconstruction. Another advantage is that the inversion can be performed on irregular grid of triangles; this means that if the object-of-interest has any curvature it can be captured better. A third advantage is the ability to reduce the algorithm computational complexity by using a triangular mesh of varying elements densities without compromising the image reconstruction quality.

Using FEM, the discretized form of the CSI cost function is given as

$$F^{\text{CSI}}(\underline{w}_{t,z}, \underline{\chi}) = F^S(\underline{w}_{t,z}) + F^D(\underline{w}_{t,z}, \underline{\chi}), \quad (22)$$

where

$$F^S(\underline{w}_{t,z}) = \frac{\sum_{t=1}^T \|\underline{u}_t - \mathcal{M}_S \mathcal{L}[\underline{w}_{t,z}]\|_S^2}{\sum_{t=1}^T \|\underline{u}_t\|_S^2}, \quad (23)$$

and

$$F^D(\underline{w}_{t,z}, \underline{\chi}) = \frac{\sum_{t=1}^T \|\underline{\chi} \odot \underline{E}_{\text{inc},t,z}^I - \underline{w}_{t,z} + \underline{\chi} \odot \mathcal{M}_D \mathcal{L}(\underline{w}_{t,z})\|_D^2}{\sum_{t=1}^T \|\underline{\chi} \odot \underline{E}_{\text{inc},t,z}\|_D^2}. \quad (24)$$

In equations (23) and (24), the discretized variables and operators are,

- $\underline{u}_t \in \mathbb{C}^R$  is a vector of size  $R$  of the scattered electric field values measured at the receivers for a transmitter  $t$ .
- $\underline{w}_{t,z} \in \mathbb{C}^N$  is a vector of size  $N$  for the contrast source values inside the imaging domain for a transmitter  $t$ .
- $\underline{E}_{\text{inc},t,z}^I \in \mathbb{C}^I$  is a vector of size  $I$  for the incident field values inside the imaging domain  $D$  for transmitter  $t$ .
- $\underline{\chi} \in \mathbb{C}^I$  is a vector of size  $I$  for the contrast values inside the imaging domain  $I$ .
- $\mathcal{L} \in \mathbb{C}^{N \times N}$  is the FEM matrix operator defined earlier.
- $\mathcal{M}_S \in \mathbb{C}^{R \times N}$  is a matrix operator that calculates the scattered field values at the receiver locations on  $S$ .

- $\mathcal{M}_D \in \mathbb{C}^{I \times N}$  is a matrix operator that calculates the scattered field values inside the imaging domain  $D$ .

In the cost function equations, the operator  $\odot$  is element-wise vector multiplication.

At each iteration of the FEM-CSI algorithm, the two variables  $\underline{\chi}$  and  $\underline{w}_{t,z}$  are updated successively. The contrast source variable  $\underline{w}_{t,z}$  is updated using a conjugate-gradient method with Polak-Ribière search directions. Next, the contrast variables  $\underline{\chi}$  are updated analytically. These two variables are updated until the algorithm converges. To enhance the quality of the FEM-CSI reconstruction results, multiplicative regularization (MR) can be used to achieve imbalance correction between the real and imaginary components of the relative complex permittivity as well as preserve the edges of the reconstructed images. The details of the FEM-CSI algorithm as well as the regularization are outlined in [36].

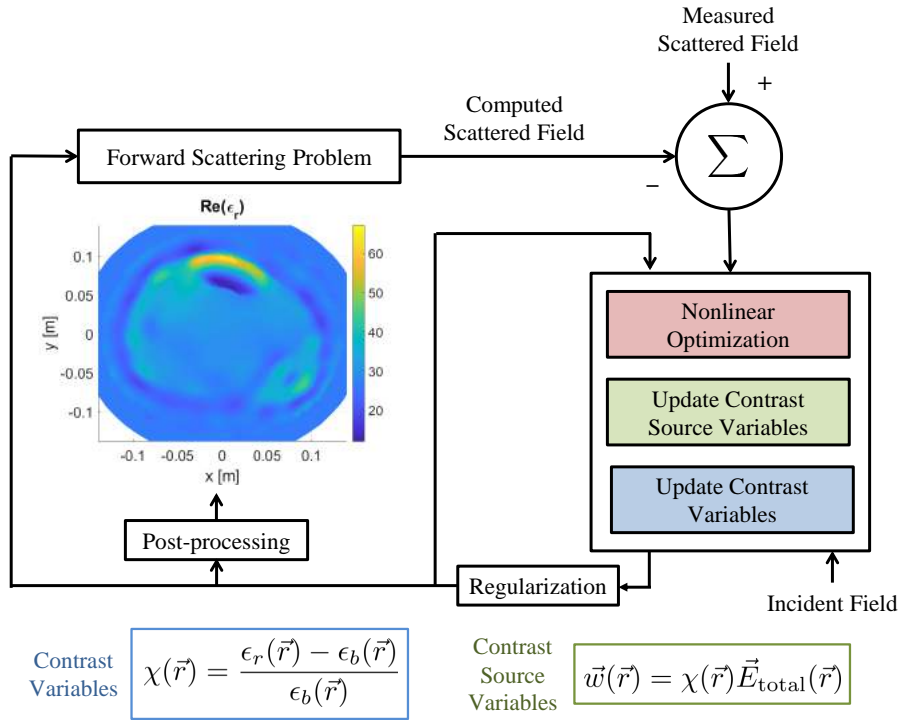


Figure 2.1: The overall mathematical procedure of reconstructing MWT images.

Fig. 2.1 shows the overall mathematical procedure of reconstructing MWT images. The procedure starts by entering the measured scattered electric field to the non-



linear optimizer that calculates the initial contrast and contrast source values along with the corresponding cost function  $F^{\text{CSI}}(\underline{w}_{t,z}, \chi)$ . Then, the multiplicative regularization is applied prior to obtaining the dielectric properties map. To reconstruct the real and imaginary relative permittivity, both permittivity parts are obtained by mathematically calculating the value of  $\epsilon_r$  at every point based on equation (10). Next, to obtain the computed scattered field, the forward scattering problem is calculated using equation (20), based on the value of the contrast source, and subtracted from the measured scattered field. This is done with the goal of minimizing the value of the cost function in the presence of the values of the incident electric field at every iteration. The process iteratively updates the contrast and contrast source until convergence or until the number of iterations reaches the maximum.

In this thesis, the MR-FEM-CSI code implemented by [36] will be utilized to conduct the required studies.

## Chapter 3: Numerical Modeling and Blind Inversion

In this chapter, a complete procedure is followed to simulate an actual microwave tomography configuration. Three cross-sectional MRI images of human leg, with various fat thicknesses, are obtained from online sources and used to generate the corresponding finite-element models. The selection of the different MWT system parameters is discussed including the number of antennas, optimum frequency of operation, type of matching medium, and variations in the dielectric properties of different tissues. In addition, the procedures of solving the forward problem using FEM and the inverse problem utilizing FEM-CSI are briefly discussed. At the end, statistical analysis on the obtained results are shown to investigate the feasibility of using MWT for bone health monitoring applications.

### 3.1. Human Leg Modeling

To model a biological structure that would best simulate bone structures within the human body, the human leg is selected to be the OI. Three cross-sectional MRI images representing the human leg under different fat thickness scenarios are retrieved from [38], [39], and [40] as shown in Figures 3.1 (a), (b), and (c), respectively. The purpose of having various fat thicknesses is to illustrate the effect of the fat layer on the efficiency of bone density monitoring throughout the re-construction process using MWT.

The process of creating the 2D model corresponding to each MRI image is done using GMSH software. GMSH is a software used commonly by engineers and scien-

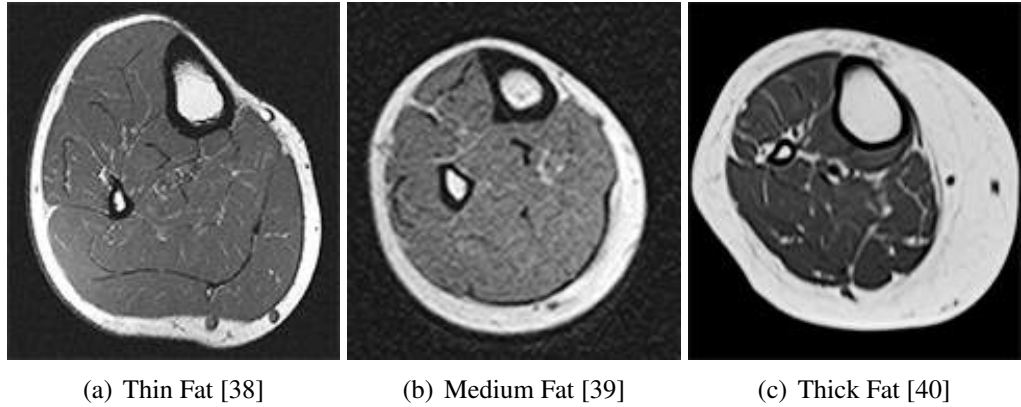


Figure 3.1: Three cross-sectional MRI images representing three fat layer thicknesses.

tists to build geometries and meshes. This software was built in 1998 and improved throughout the years to include four modules, which are the geometry designer, mesh generator, PDE solver, and post-processor [41,42]. In this thesis, the designer and mesh generator are used only. In 2D modeling, the mesh elements can be squares or triangles, however, triangles are commonly used because they can fit in curved and circular edges without any overlapping between different regions [43].

In order to create each model, GMSH requires a structural file as an input, which includes the boundary points for each tissue layer within the model. Furthermore, MATLAB is used to manually extract boundaries corresponding to five major tissues from the MRI images; these five major tissues are shown in Fig. 3.2. The points corresponding to the extracted boundaries are imported into GMSH and connected with lines to form the overall model for each MRI image.

Next, the formed structure from each MRI model is imported to GMSH to generate a triangular mesh. Each mesh includes  $N$  number of nodes connecting  $T$  number of triangles. Each node in the mesh has its own local index with respect to a triangular element and a global location number with respect to the whole mesh.

The lines connecting the nodes within a triangle are within a pre-determined characteristic length (CL) that represents the size length of a triangle's side.

To predict the electromagnetic behavior accurately, the CL is determined using the following equation,

$$CL = \frac{\lambda}{10}, \quad (25)$$

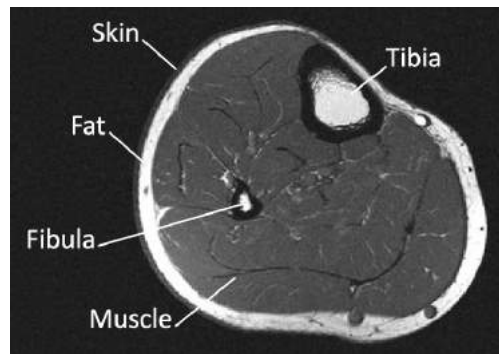


Figure 3.2: MRI Axial image for human leg showing structures including skin, fat, muscles, tibia and fibula.

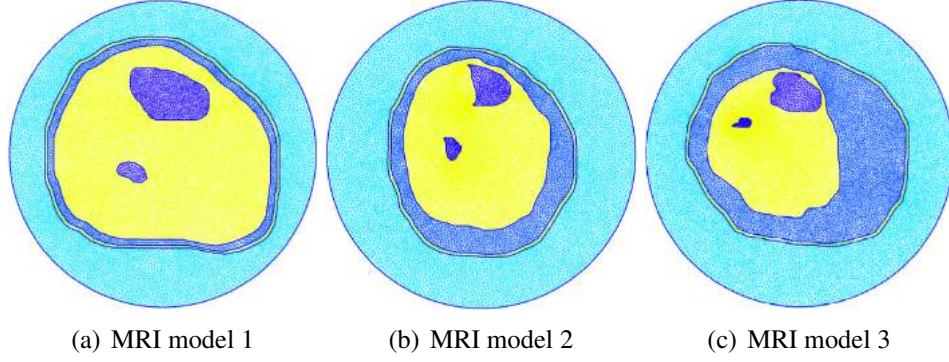


Figure 3.3: Triangular meshes generated by GMSH of the three MRI images.

where the wavelength  $\lambda$  is given by

$$\lambda = \frac{c}{f\sqrt{\epsilon_{r,\max}}}. \quad (26)$$

Here  $c = 3 \times 10^8$  [m/s] is the speed of light in free-space,  $f$  is the simulation frequency, and  $\epsilon_{r,\max}$  is the largest possible value of the dielectric constant within the OI. In general, having smaller characteristic length provides better and more accurate simulation results, as the electromagnetic wave is being discretized into a higher number of segments within its wavelength interval [9,36]. Fig. 3.3 shows the corresponding triangular meshes generated for the three MRI images models using the GMSH software.

### 3.2. Optimum Frequency Selection

Before proceeding with the forward and inverse problems analysis, the optimum frequency to be used should be determined. The selection of the optimum frequency is important as it will effect the performance of the MWT system as well as the quality of the inverse problem reconstructions.

As an electromagnetic wave propagates in various media, it suffers from power loss due to material attenuation. A method to decide on an optimum frequency of operation is to investigate this attenuation through a parameter known as the skin depth of an electromagnetic (EM) wave. The skin depth is a value that represents the depth at which the EM wave reaches 36.8% of its maximum value at the interface between two

Table 3.1: Attenuation Coefficient [dB/m] and Skin Depth [cm] for Skin, Fat, and Muscle tissues

Frequency	Skin ( $\alpha, \delta$ )	Fat ( $\alpha, \delta$ )	Muscle ( $\alpha, \delta$ )
0.5 GHz	171.19, 5.10	40.48, 21.5	108.31, 8.0
0.8 GHz	206.46, 4.20	48.99, 17.7	197.17, 4.4
1.0 GHz	224.97, 3.80	56.20, 15.5	341.01, 2.6

media [44]. In the application herein, this interface is between the matching medium and skin. The skin depth is given as,

$$\delta = \frac{1}{\alpha}. \quad (27)$$

Here  $\alpha$  is the attenuation, in Nepers-per-meter ([Np/m]), that the electromagnetic wave (EM) experiences as it propagates. The attenuation is calculated as,

$$\alpha = \omega \sqrt{\frac{\mu_0 \epsilon_r \epsilon_0}{2} \left[ \sqrt{1 + \left[ \frac{\sigma}{\omega \epsilon_0 \epsilon_r} \right]^2} - 1 \right]}. \quad (28)$$

To convert from [Np/m] to [dB/m],  $1Np = 8.868dB$ . The parameters, relative permittivity ( $\epsilon_r$ ) and conductivity ( $\sigma$ ), vary for different types of tissues and are a function of frequency. Thus the attenuation will also change as frequency changes.

For different types of tissues in a human leg, the attenuation along with the skin depth are calculated for three different frequencies as shown in Table 3.1. The three selected frequencies are 0.5 GHz, 0.8 GHz, and 1 GHz; these frequencies are commonly used in literature for biomedical MWT applications [1,9,45]. The table shows that when the frequency increases, the attenuation increases and thus the skin depth decreases; this indicates that the distances traveled by the EM wave beyond the skin get reduced at higher frequencies. Thus, the effect of internal organs on the scattered fields may not be sensed and thus the reconstruction of the inversion algorithm will be poor.

In addition to attenuation and skin depth, electromagnetic waves suffer from reflections at the interface between two media due to the impedance mismatch. Here the two media can be between the matching medium and the skin, or any two tissues within

an organ. These reflections can be quantified using a parameter called the reflection coefficient, which can be calculated between two media as follows,

$$\Gamma = \frac{\frac{1}{\sqrt{\epsilon_{r2}}} - \frac{1}{\sqrt{\epsilon_{r1}}}}{\frac{1}{\sqrt{\epsilon_{r2}}} + \frac{1}{\sqrt{\epsilon_{r1}}}}. \quad (29)$$

Here  $\epsilon_{r1}$  and  $\epsilon_{r2}$  represent the relative permittivity value of the first and second layers, respectively, and they are frequency-dependent.

Since both skin depth and reflection coefficient are frequency-dependent, there must be an optimum frequency that would decrease the attenuation and meanwhile compensating for the reflection wave loss. Furthermore, for a MWT configuration, one would prefer to use lower frequencies in order to have more depth of penetration, which would result in better reconstruction images. However, this comes with the cost of having bigger antennas. Antenna sizes are related to the wavelength of the propagating EM signal; furthermore, the smaller the frequency, the larger the wavelength and thus the antennas. Having big antennas is not useful for wearable applications, which is the aim of the system being designed. On the other hand, having higher frequencies require more power within the system since the attenuation is higher. Higher power might not be feasible as it might exceed accepted levels of EM radiation exposure for humans. Also, high-power EM transmitters are expensive.

Thus, to get the advantages of both higher and lower frequency values, the selected frequency of operation is 0.8 GHz. Going further in the upcoming sections, the reconstruction results of all three frequencies is provided to support this decision.

### 3.3. Forward Simulations

As mentioned earlier, the forward problem is solved using 2D FEM solver developed by A. Zakaria et al. [46, 47], where the MWT configuration along with OI are represented by triangular meshes introduced in Section 3.1. The main objective of the forward simulations are to collect synthetic data to test the inversion algorithm and the feasibility of using MWT to detect changes in bones' electrical properties.

The inputs for the finite element solver were as follows,

- Mesh: generated from MRI cross-sections.
- Simulation frequency: 0.8 GHz.

Table 3.2: Bulk Electrical Properties of Regions in the FEM Model

Region	Relative Complex Permittivity ( $\epsilon_r$ )
Matching Medium	$26 - j18.0$
Skin	$42 - j18.8$
Fat	$11 - j2.3$
Muscles	$55 - j20.5$

- Model Boundary: absorbing boundary condition (ABC).
- Relative complex permittivity of various regions in model (given in Table 3.2 and based on [5, 16]).
- Transmitters' (TX) configuration: 24 point-sources equally distributed on a circle of radius 15 cm.
- Receivers' (RX) configurations: 24 receivers located on a circle of radius 15 cm. The receivers and transmitters are located on the boundary labeled as  $S$  in Figure 1.1.
- Matching medium surrounding the OI: 80:20 Glycerin/Water Solution with relative complex permittivity of  $\epsilon_r = 26 - j18$  [48, 49].

The number of TX and RX antennas was determined after several tests. The inversion results did not have significant improvements when increasing the number of antennas to more than 24. In addition, having less number of antennas degraded the overall quality of the reconstructed images. As for the selected matching medium, it is considered as an optimum medium for biomedical MWT applications; however other matching media will be investigated later in the thesis.

Table 3.2 shows the dielectric properties of different tissues within the model based on [5, 16] observations at 0.8 GHz frequency.

To simulate vitamin D deficiency, bone density and BVF should be varied within the simulated model. The variation in bone density and BVF was discussed by P.M. Meaney et al. [1] for certain scenarios. Based on their study, as the volume of bones decreases, the overall BVF decreases and furthermore, the relative electrical properties increase. In addition, as previously discussed in 1.3.4, due to Vitamin D deficiency, the absorption of calcium to the bones is reduced which may lead to lowering the BVF

values. To illustrate reduction in BVF, the following varying bone electrical properties are considered initially,

- Healthy Bone:  $\epsilon_r = 13 - j3.0$ ,
- Bone with 0.25 BVF:  $\epsilon_r = 18 - j3.2$ ,
- Bone with 0.1 BVF:  $\epsilon_r = 23 - j3.4$ .

For a healthy person, the BVF value is considered to be the highest, which is given as 0.5 in [1]. A BVF of 0.25 equals half of highest value of a healthy patient, while a 0.1 BVF is considered to be a severe case with low bone density. Going further in the thesis, more BVF values are used to evaluate the quality of bone reconstruction algorithms.

### 3.4. Blind Inversion

After collecting the synthetic data for different models with varying bone electrical properties, the data are used as inputs for the inversion algorithm. As mentioned in the previous chapter, the inversion algorithm considered in this work is the multiplicative regularized contrast source inversion method (MR-CSI) implemented within the framework of the finite-element method (FEM) [36]. The forward problem and inversion algorithm share similar parameters, which are the frequency of operation, the matching medium, and the number of transmitters and receivers as well as their locations.

The difference between the forward problem and the inverse problem is the mesh used to solve both problems. To prevent inverse crime, the forward mesh and inversion mesh are chosen to be different. In addition, 3% uniform noise was added to the synthetic data.

For the inversion algorithm, the imaging domain,  $D$ , where the electrical properties of the human leg are to be estimated, was chosen to be a circular domain with a radius of size 14 cm. The inversion algorithm was executed three times for each synthetic dataset representing different values of BVFs. Each time, the inversion algorithm was allowed to run for 1000 iterations to ensure convergence. The results of the inversion algorithm are shown in Figures 3.4, 3.5, and 3.6 for MRI models 1, 2 and 3, respectively. For each result, the red-dotted lines indicate the location of the bones. The analysis of the result will be discussed in Section 3.6.



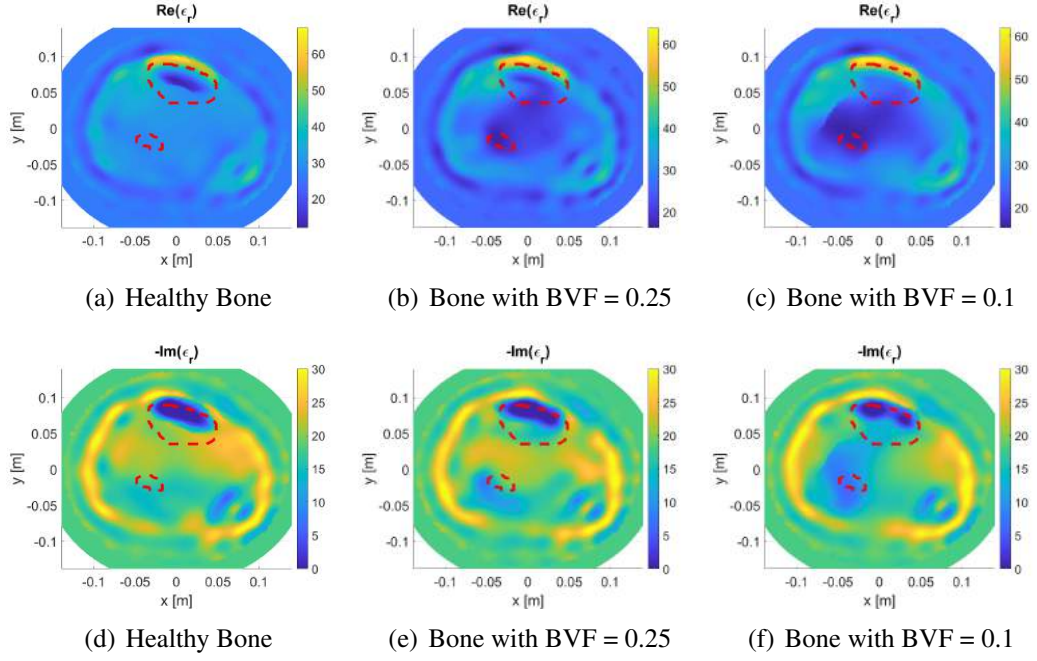


Figure 3.4: MRI model 1: The real and imaginary components of the relative complex permittivity reconstruction.

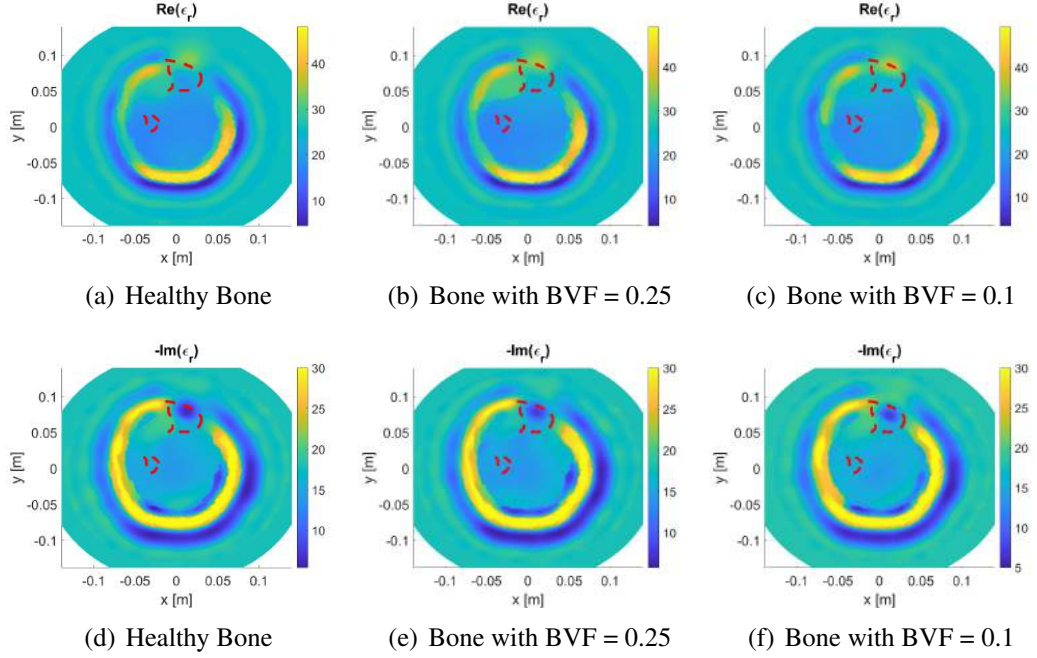


Figure 3.5: MRI model 2: The real and imaginary components of the relative complex permittivity reconstruction.

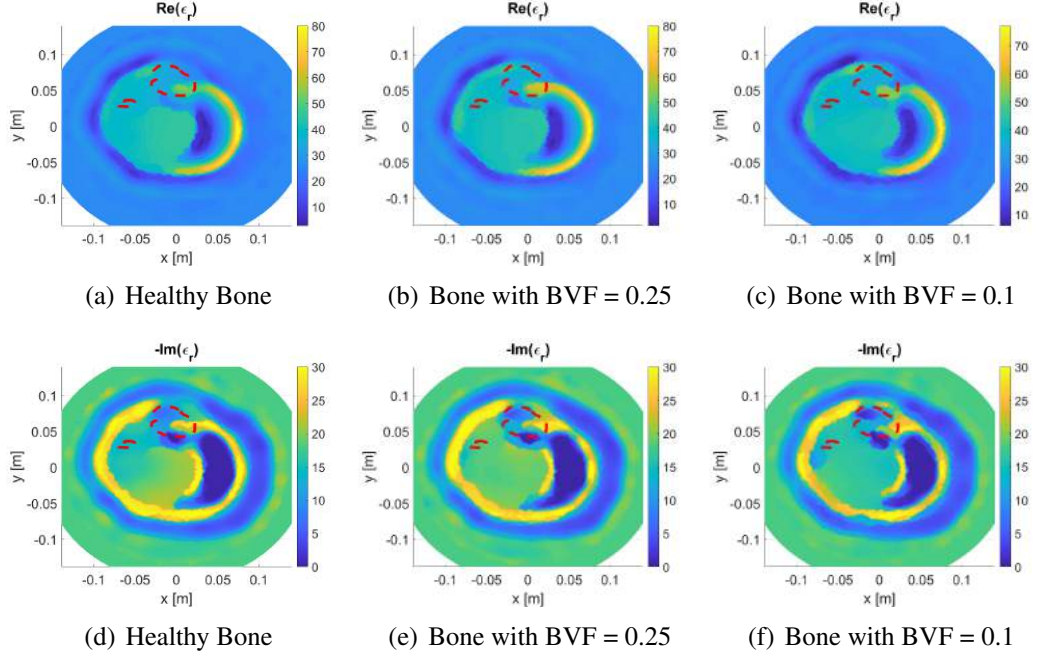


Figure 3.6: MRI model 3: The real and imaginary components of the relative complex permittivity reconstruction.

### 3.5. Inversion at Non-optimum Frequencies

As previously discussed in section 3.2, the optimum frequency of operation is selected to be 0.8 GHz. Aside from showing the mathematical evaluation of this selection, testing the three frequencies within the framework of the forward and inverse solver is done following the same procedure mentioned in the previous sections. Figures 3.7, 3.8, and 3.9 show the results of the three frequency values, 0.5 GHz, 0.8 GHz, and 1.0 GHz, for MRI models 1, 2, and 3 healthy bone case.

From the figures, it can be noted that using lower frequencies results in better reconstruction process. However, as previously discussed, this comes with the cost of having bigger antennas that can not be suitable for portable and wearable applications. On the other hand, having high frequencies reduces the quality of the reconstruction. In conclusion, the above figures prove that our selection of 0.8 GHz is the optimum between the three frequency values.

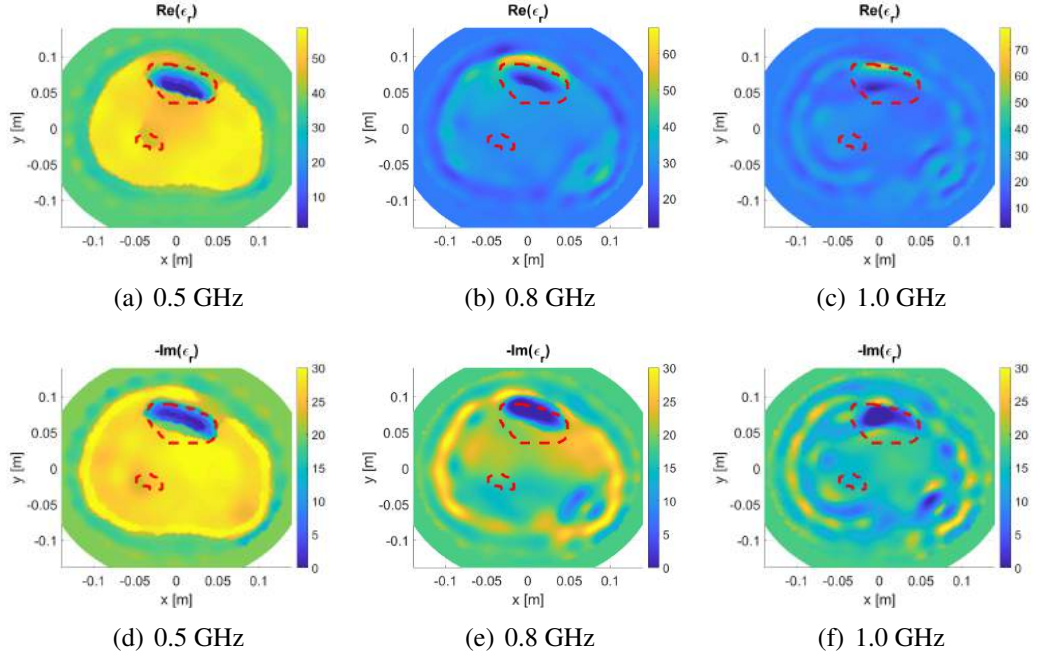


Figure 3.7: Testing frequency values on MRI model 1 healthy bone.

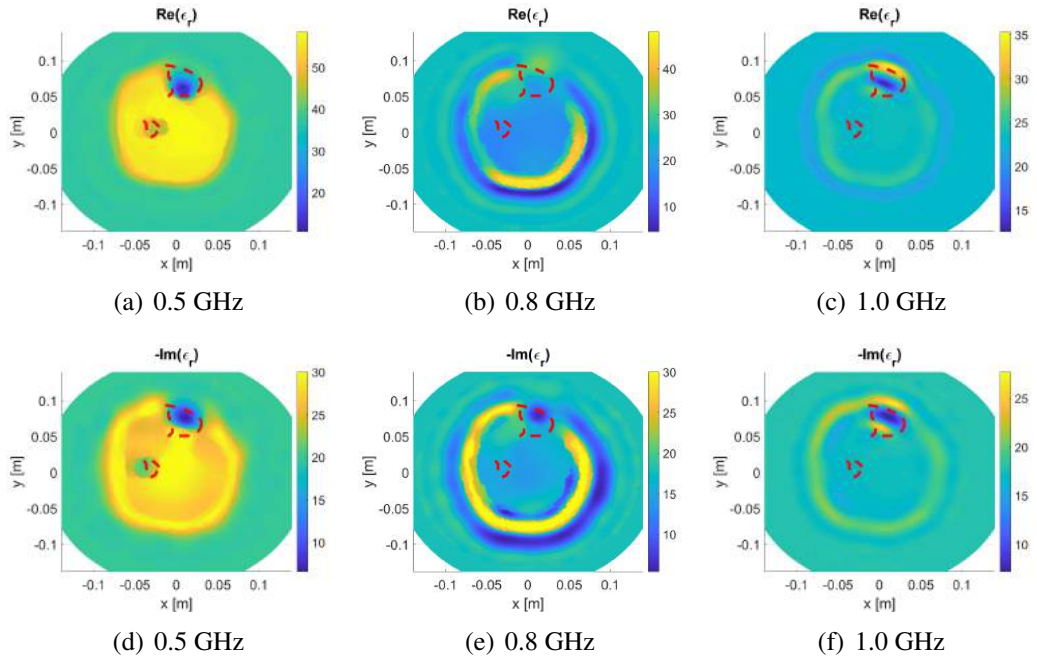


Figure 3.8: Testing frequency values on MRI model 2 healthy bone.

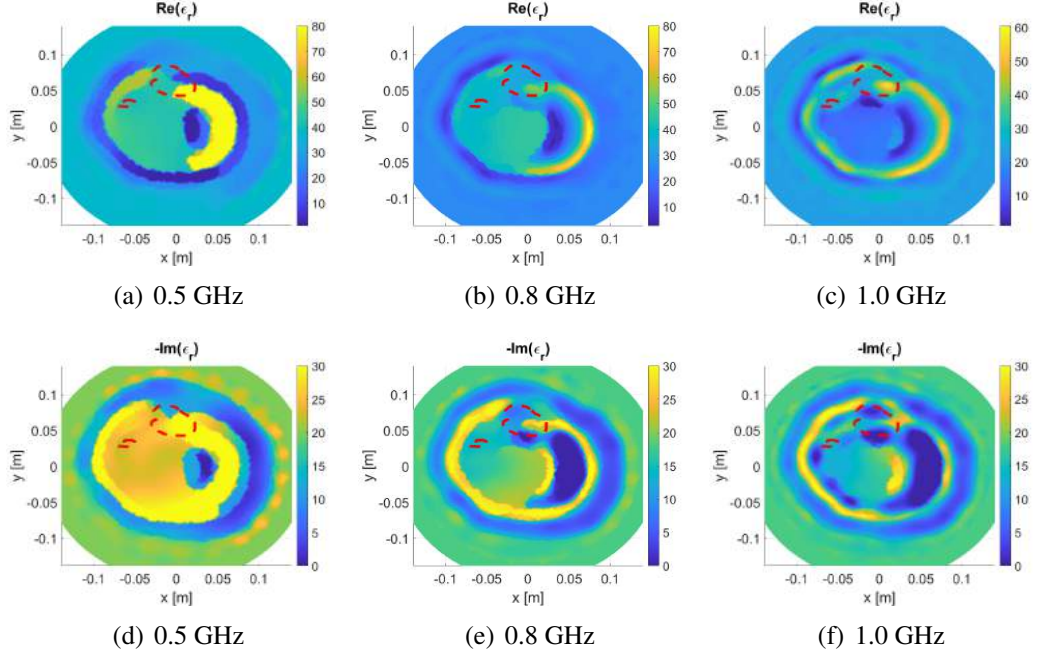


Figure 3.9: Testing frequency values on MRI model 3 healthy bone.

### 3.6. Analysis and Observations

For all the inversion results, the algorithm was successful in locating the leg and estimating its size. Further, the algorithm was able to distinguish two main regions within the leg, an outer region depicting the skin and fat layer, and an inner region representing the muscle. The skin and fat layer were almost merged together because the skin layer is thin in comparison to the wavelength at 0.8 GHz and its electrical properties are close to that of the matching medium.

Within the muscle region, the location of the tibia bone is clear from the reconstructions of the imaginary component for the various BVF cases; these reconstructions are similar to each other, which is expected since changes to the imaginary component of  $\epsilon_r$  are small between a health bone and bone with lower BVF. Nevertheless, for the real component reconstructions, the tibia bone is not well-reconstructed. However, it can be noted that the tibia bone reconstruction is merging with the muscle as the bone density decreases, especially for MRI model 1. These results of the real-component reconstruction indicate that there is potential in using MWT for monitoring the progress of bone density treatment. In regard to the fibula bone, it was not well reconstructed;

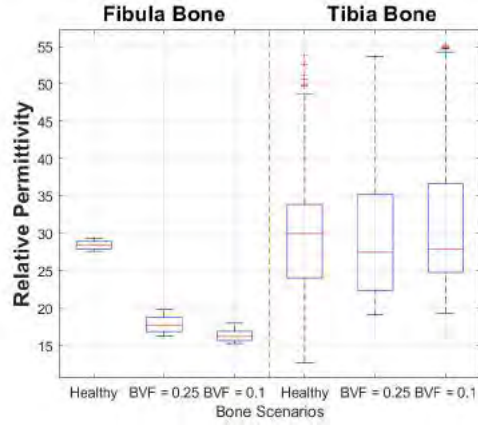
since the bone is small and well inside the leg, the scattered field from it is small and cannot be captured by the receivers surrounding the leg. Further investigations are required to find a solution to enhance the reconstruction.

To elaborate more on that, statistical investigations on the change in bones' dielectric properties are carried out. For the statistical analysis, two methodologies are followed.

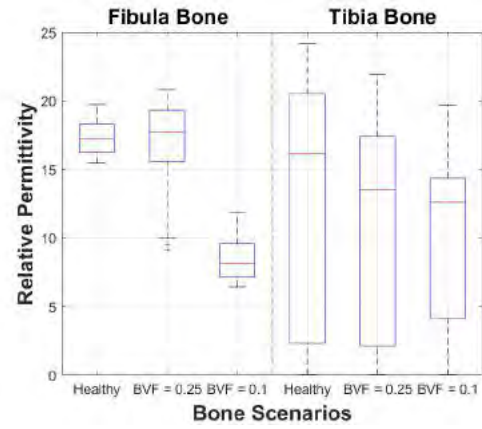
In the first method, the forward model is used to provide structural information and to obtain the boundaries of both tibia and fibula bones. Next, each obtained boundary is used as a mask on both real and imaginary relative permittivity reconstruction results, which is shown as red dashed line in Figures 3.4, 3.5, and 3.6. The values within these masks are extracted from the reconstruction results to obtain the dielectric values of both bones. Statistical analysis in the form of box plots are performed on the extracted results for each bone. The corresponding box plots are shown in Figures 3.10, 3.11, and 3.12 for MRI models 1, 2, and 3, respectively.

To solve the region overestimation problem, a second method of analysis that relies on using the imaginary part of reconstructed images is considered. The imaginary part of relative permittivity reconstructions are used to provide the structure of the tibia bone as estimated by the inversion algorithm. From the reconstructed images, it can be noted that the imaginary part gave a good representation of the structure of the detected bone; thus the boundaries of the reconstructed tibia bone are extracted. Next, these boundaries are used as a mask to extract dielectric information from the real part of relative permittivity images. The extracted dielectric data for all bone scenarios are illustrated using the box plot representation shown in Figures 3.13, 3.14, and 3.15 for MRI models 1, 2, and 3, respectively. In all three box plots, it can be observed that the mean of the real part of the relative permittivity is increasing with a decrease in bone density. This supports the hypothesis of this thesis; however, improvements on the inversion process is going to be performed in the next chapters for better reconstructions and better analysis of variations in the bone properties. It is important to note here that the second technique in analyzing the bone properties uses the reconstruction results exclusively, therefore it is more realistic. In an actual practical medical system, the forward model is not available to extract the actual bones' locations and structure.



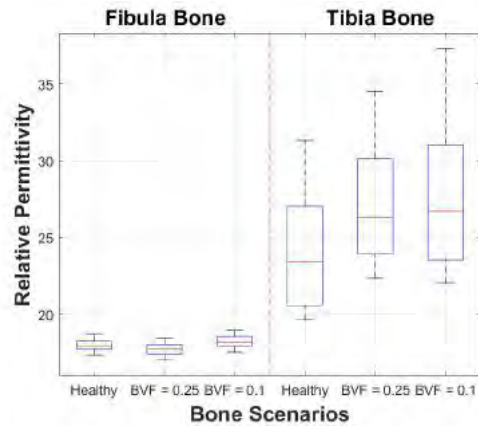


(a) Real part

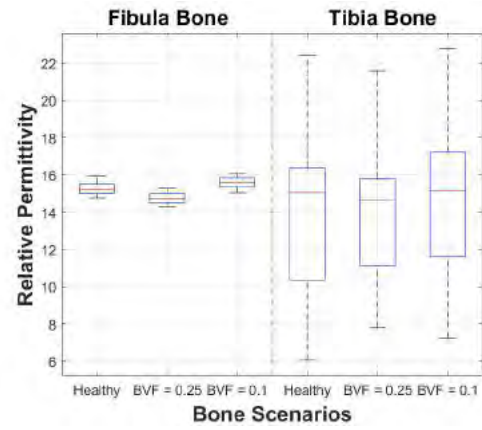


(b) Imaginary part

Figure 3.10: Box plot representation of relative permittivity values using the forward model as bone mask in MRI model 1.

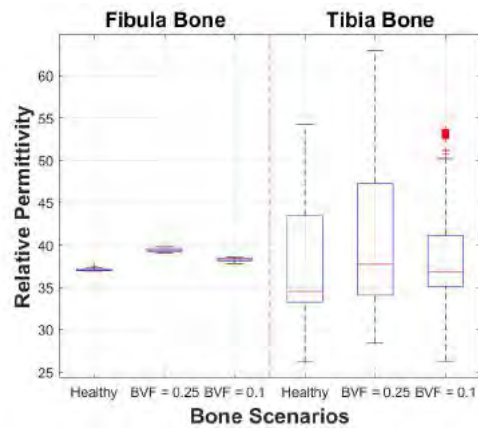


(a) Real part

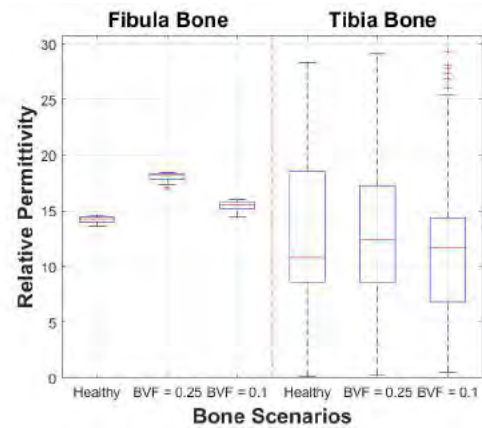


(b) Imaginary part

Figure 3.11: Box plot representation of relative permittivity values using the forward model as bone mask in MRI model 2.



(a) Real part



(b) Imaginary part

Figure 3.12: Box plot representation of relative permittivity values using the forward model as bone mask in MRI model 3.

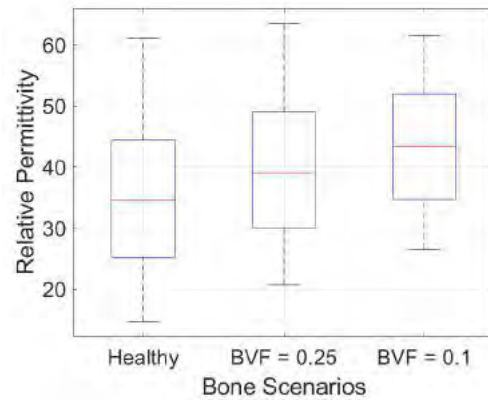


Figure 3.13: The box plot representation of the tibia bone real part relative permittivity in MRI model 1.

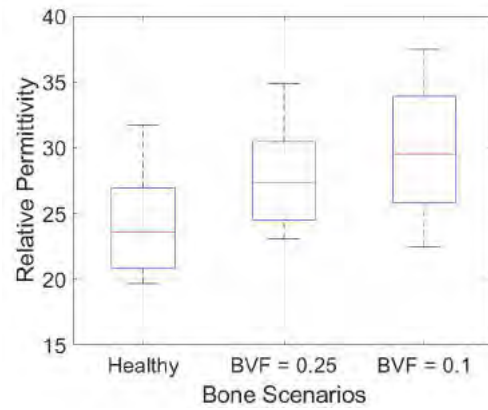


Figure 3.14: The box plot representation of the tibia bone real part relative permittivity in MRI model 2.

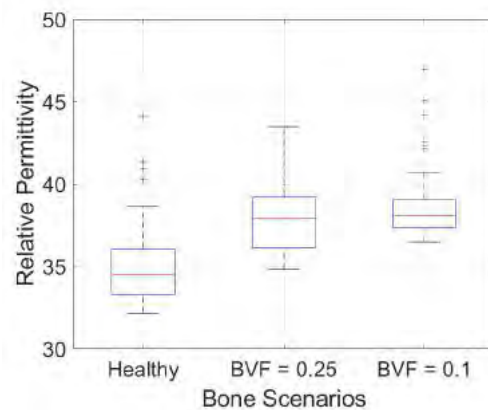


Figure 3.15: The box plot representation of the tibia bone real part relative permittivity in MRI model 3.

## Chapter 4: Inversion Enhancements

In this chapter, enhancement procedures of the inversion process are explored. Several parameters related to the inversion algorithm are changed and investigated, which are: the incorporation of prior information related to the structure and dielectric properties, the imaging domain boundary, the antennas' location, and the matching medium. In addition, the analysis and observations based on the outcomes are briefly discussed.

### 4.1. Incorporating Prior Information

As previously mentioned in Section 3, all reconstructed images gave good results in terms of locating the human leg, which is the OI. However, the localization of bone tissues was not clear in all images. Moreover, images were not reliable for bone density and dielectric properties monitoring and evaluation. Thus, the use of inversion enhancement procedures are required in order to achieve better reconstructions. One method to achieve this, is by using prior information related to the OI's various features as input to the inversion algorithm. Within the framework of FEM-CSI, the prior information is incorporated as an inhomogeneous background.

The first incorporated feature is related to the structural information of the OI. As shown by C. Gilmore *et al.* [9], the use of prior information about the boundaries of various tissues within the organ enhanced the overall quality of reconstruction. The second feature that can be incorporated as prior information is the dielectric properties of every tissue. Estimate values for the complex permittivity of healthy tissues can be found in literature, and can be used as an initial guess for bulk regions within OI. These bulk regions are the skin, fat, and muscle tissues.

In [9], the estimations of the OI structure were done manually by a trained eye experienced in microwave imaging. This procedure, however, required manual interference with the reconstruction results, which can not be done by non-expert users, such as medical doctors. Another technique to estimate the boundaries of the various tissues automatically before performing MWT was by incorporating a secondary imaging modality such as ultrasound [31] or MRI [50]; however this technique might be costly and less user-friendly.



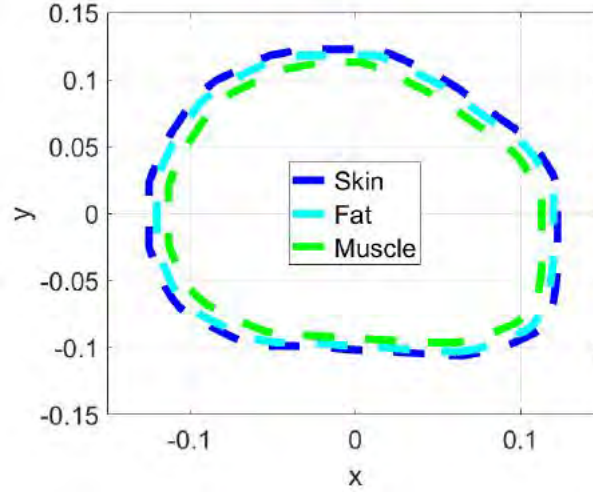


Figure 4.1: Structural information used within the inversion mesh as prior information for MRI model 1.

In this thesis, to prove the concept of using prior information, the structural information is obtained initially from the forward problem MRI models. However, since the MRI images are not available usually for a patient, in Chapter 5 the structural information is estimated from the blind MWT reconstructions using an image processing algorithm discussed later. Further, structural information of the tissue layers extracted from the MRI models are shown in Figures 4.1, 4.2, and 4.3 for MRI models 1, 2, and 3, respectively. The structural information represents the boundaries between the matching medium and the skin, the skin and fat layer, and the fat layer and muscle tissues. This structural information is input to the inversion algorithm. In comparison, for the blind inversions presented in Chapter 3, the input mesh included only the chamber boundary with unknown information about the OI structure. Further, Fig. 4.4 shows the inversion meshes of MRI models 1, 2, and 3 after exporting the points to GMSH. It should be noted that the meshes do not include bone structural information as it is the main tissue within the leg to be imaged and monitored.

For each MRI model, three inhomogeneous background cases are considered. The difference between each case are the values of the relative permittivity assigned for the different regions. These case are,

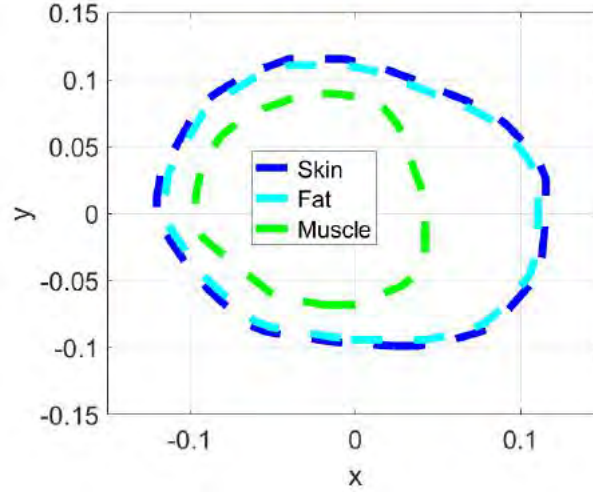


Figure 4.3: Structural information used within the inversion mesh as prior information for MRI model 3.

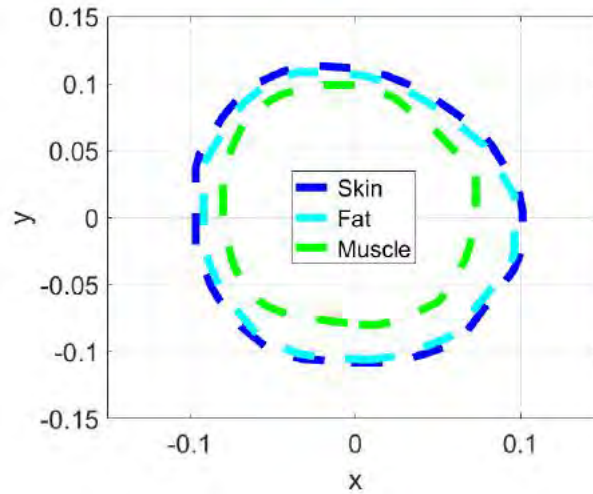


Figure 4.2: Structural information used within the inversion mesh as prior information for MRI model 2.

1. **Inhomogeneous background with a mid value layer:** the relative permittivity value for the skin, fat, and muscle tissues is set to a common middle value calculated as,

$$\epsilon_r^{\text{mid}} = \frac{\epsilon_r^{\text{high}} + \epsilon_r^{\text{low}}}{2}, \quad (30)$$

where  $\epsilon_r^{\text{high}}$  and  $\epsilon_r^{\text{low}}$  are, respectively, the highest and lowest values of expected bulk permittivity within the OI. In this thesis, the highest value corresponds to the

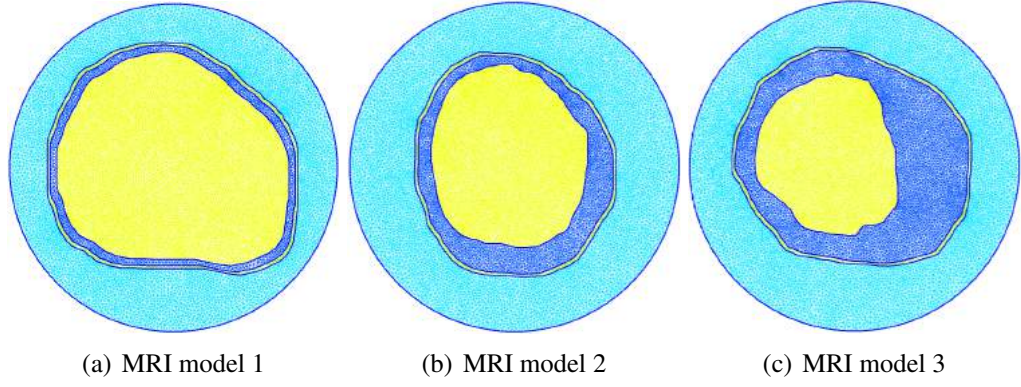


Figure 4.4: Inversion meshes with prior information about location and dielectric properties of tissues for MRI models 1, 2, and 3.

muscle relative permittivity while the lowest value is the fat relative permittivity. The values are obtained from literature [16].

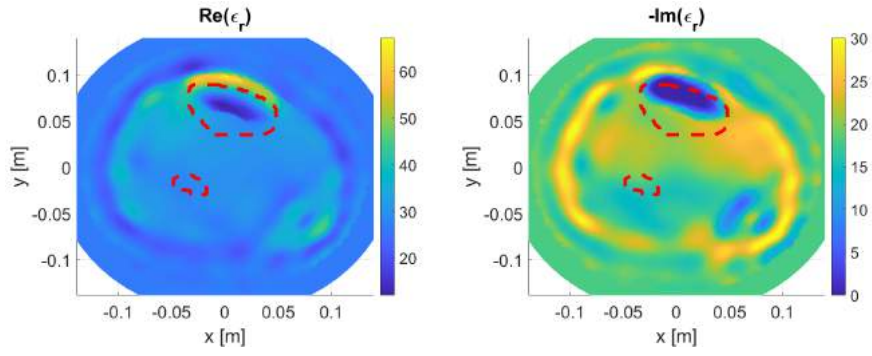
2. **Inhomogeneous background with a skin-fat layer:** the skin layer is assigned the skin's relative permittivity from literature, whereas the fat and muscle tissues are assigned the fat's relative permittivity value.
3. **Inhomogeneous background with a skin-fat-muscle layer:** each layer - skin, fat, and muscle - is assigned its respective relative permittivity obtained from literature.

The relative permittivity values used for skin, fat, and muscle tissues have been reported earlier in Table 3.1 in Chapter 3.

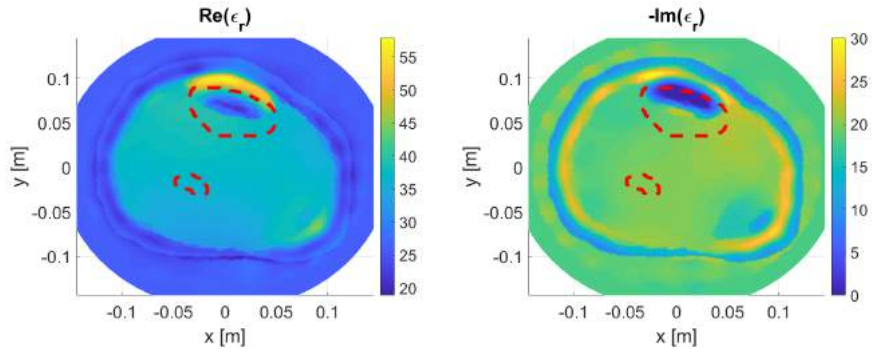
The inversion reconstruction results using the three aforementioned inhomogeneous background cases for a healthy bone case are shown in Figures 4.5, 4.6, 4.7 for MRI models 1, 2, and 3, respectively. Similar to the blind inversion results done before, the imaging domain was circular and the antennas were located on a circular surface surrounding the OI. The analysis and discussion of results are done in Section 4.5.

#### 4.2. Varying the Imaging Domain Boundary

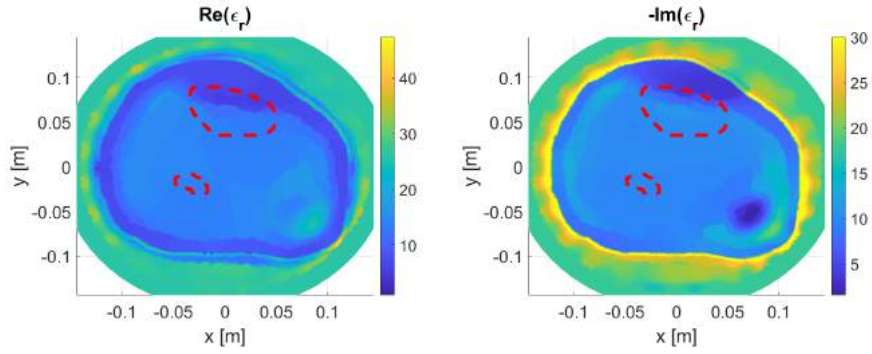
This section discusses the effect of changing the imaging domain from circular to other shapes that follow the OI outer contour. As shown by [30], reducing the imaging domain area enhances the reconstruction process. Moreover, the reconstruction



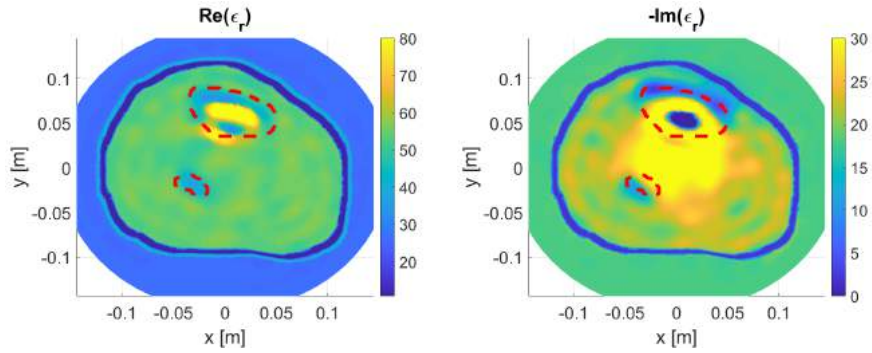
(a) Blind Inversion



(b) Inhomogeneous background with mid value layer

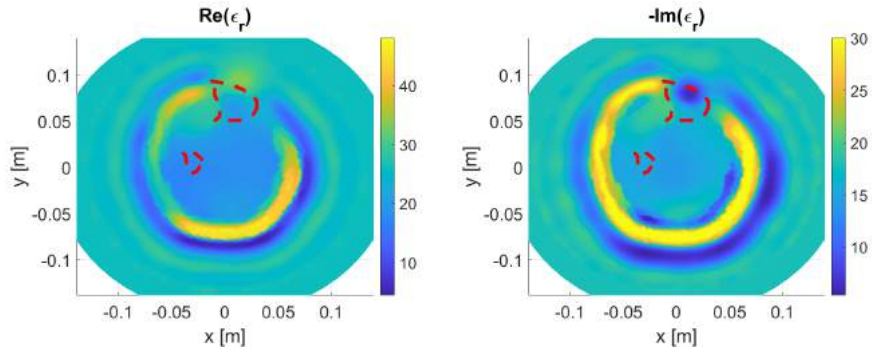


(c) Inhomogeneous background with skin-fat layer

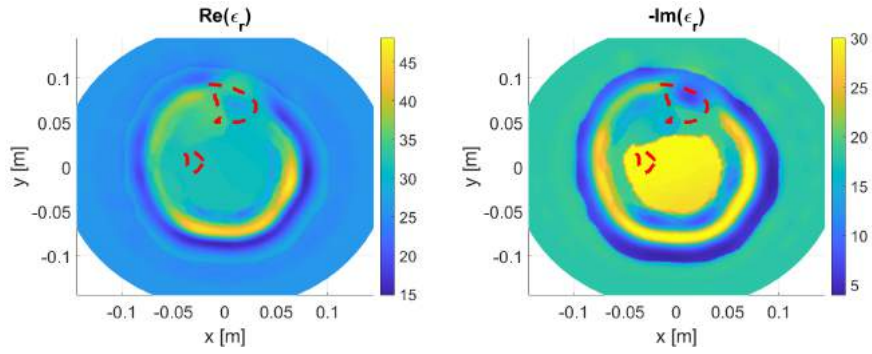


(d) Inhomogeneous background with skin-fat-muscle layer

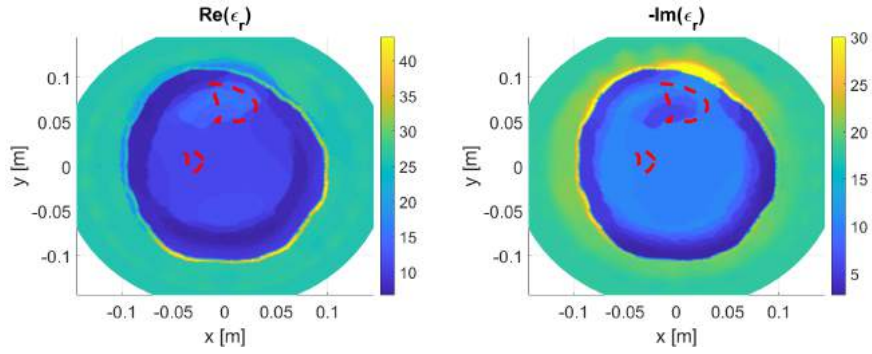
Figure 4.5: Incorporating prior info to enhance MRI model 1 reconstruction.



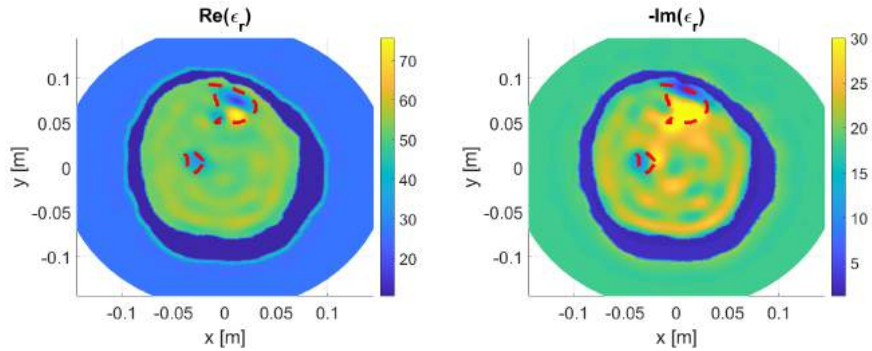
(a) Blind Inversion



(b) Inhomogeneous background with mid value layer



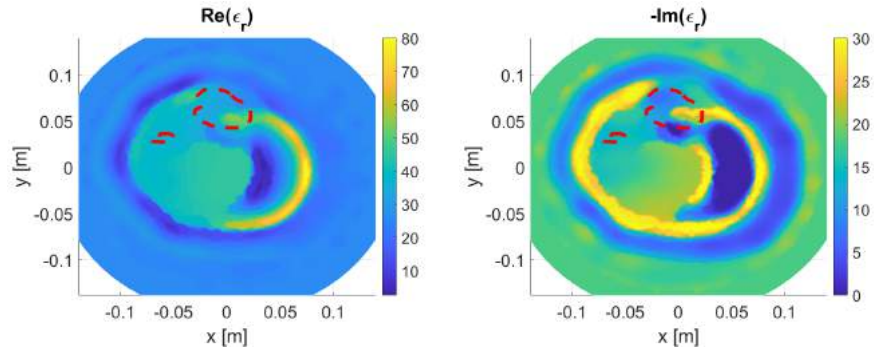
(c) Inhomogeneous background with skin-fat layer



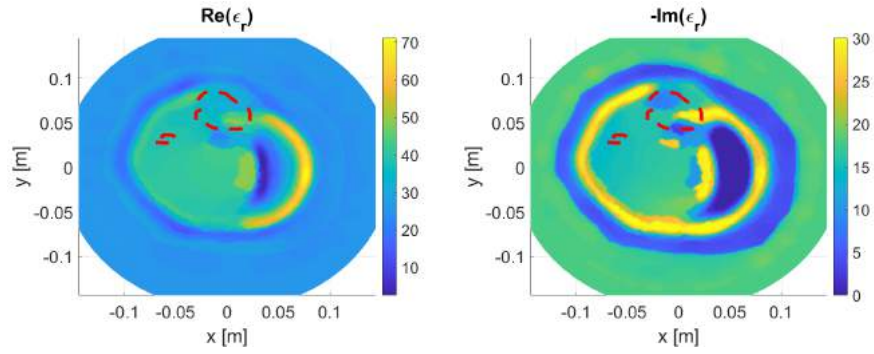
(d) Inhomogeneous background with skin-fat-muscle layer

Figure 4.6: Incorporating prior info to enhance MRI model 2 reconstruction.

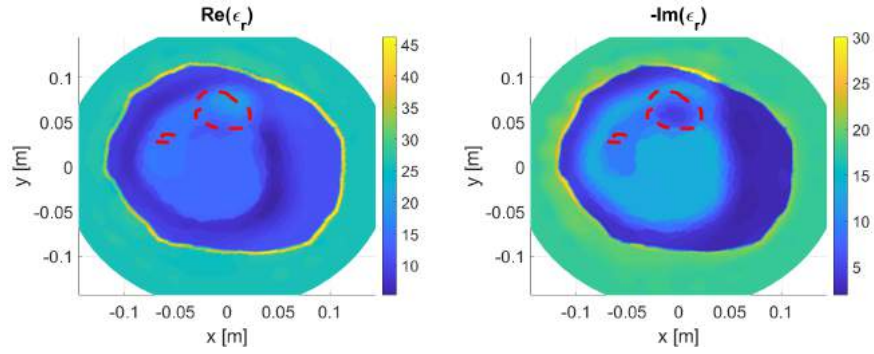




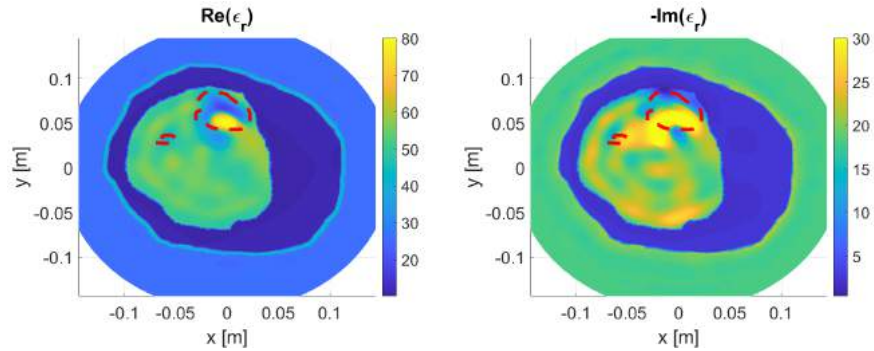
(a) Blind Inversion



(b) Inhomogeneous background with mid value layer



(c) Inhomogeneous background with skin-fat layer



(d) Inhomogeneous background with skin-fat-muscle layer

Figure 4.7: Incorporating prior info to enhance MRI model 3 reconstruction.

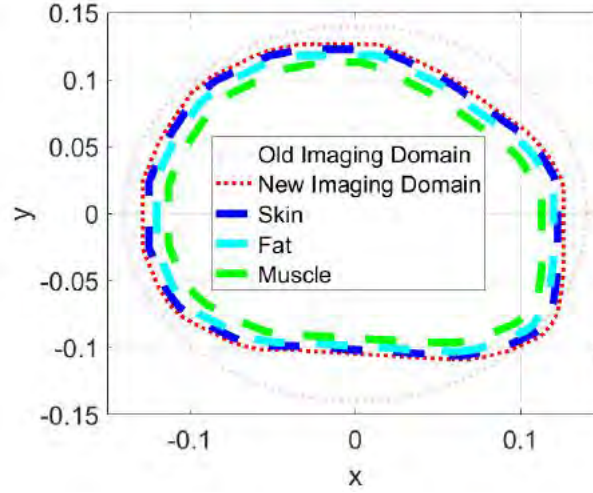


Figure 4.8: Old and new imaging domain boundaries for MRI model 1.

calculations complexity and time are reduced also when reducing the imaging domain area, as the number of unknowns to be estimated decreases.

In [30], the researchers used the resonant frequency measurements to estimate the boundaries of the OI and thus, reducing the imaging domain. However, this required additional usage of the operating antennas which resulted in having more calculations.

In this thesis, to prove the concept of using an OI-based imaging domain shape, the imaging domain boundary is determined using the MRI models outermost tissue, which is the skin. Figures 4.8, 4.12, and 4.13 show the new imaging domain for MRI model 1, 2, and 3, respectively. For the earlier blind inversions, the imaging domain was circular of radius 14 cm surrounding the OI. It should be noted that since the MRI image is usually not available in real practical MWT systems, in the next chapter a method to estimate the imaging domain boundary from blind inversions will be outlined.

For each MRI model, the inversion algorithm was allowed to run using the new OI-contour based imaging domain boundary with four scenarios of background, which were using an homogeneous background case and the three cases of using an inhomogeneous background discussed in Section 4.1. Figures 4.11, 4.12, and 4.13 show the inversion results for MRI models 1, 2, and 3, respectively. The antennas for all simulations were still located on a circle of radius 15 cm surrounding the OI. The analysis and discussion of results are done in Section 4.5.

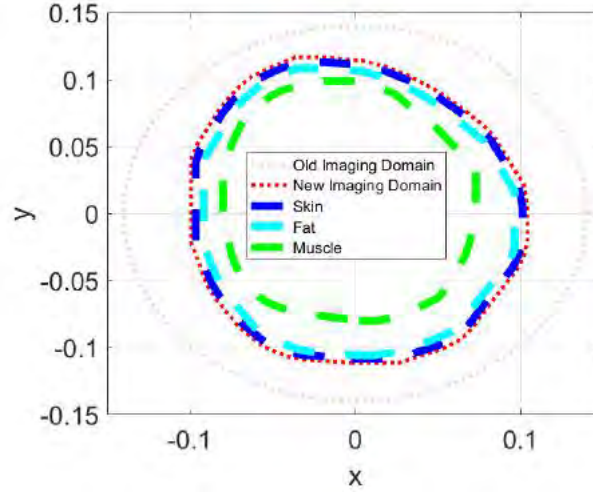


Figure 4.9: Old and new imaging domain boundaries for MRI model 2.

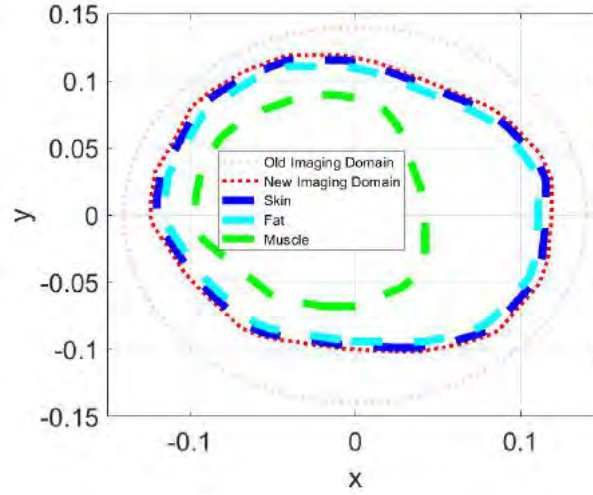


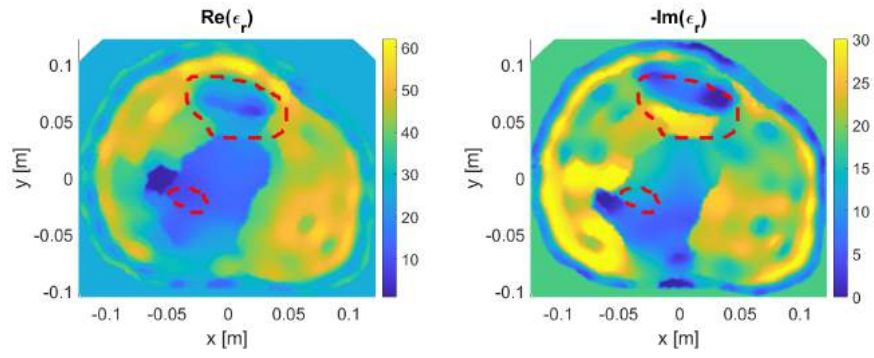
Figure 4.10: Old and new imaging domain boundaries for MRI model 3.

### 4.3. Relocating Antennas

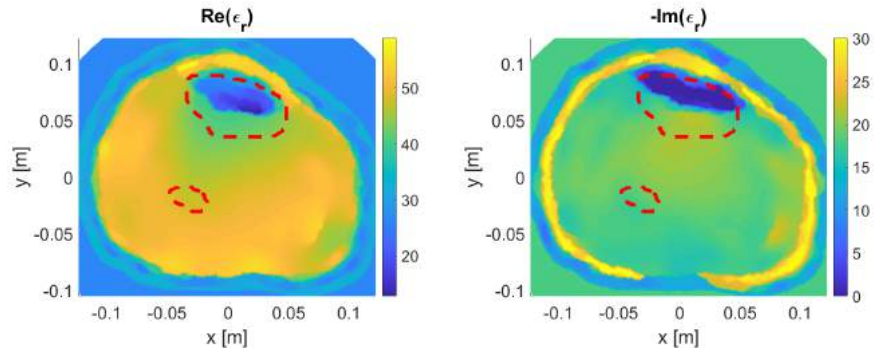
In this section, the location of antennas is changed to be surrounding the OI outermost contour in order to simulate an actual wearable system scenario. By having the antennas close to the OI, the loss of the transmitted or received signals to the matching medium is reduced as more EM energy is directed towards the OI itself or captured by the receiving antennas. Theoretically, this should improve the reconstruction results in MWT.

Varying the antennas' locations was previously discussed by [31] for localizing tumors using a MWT system designed for breast cancer detection. The location of

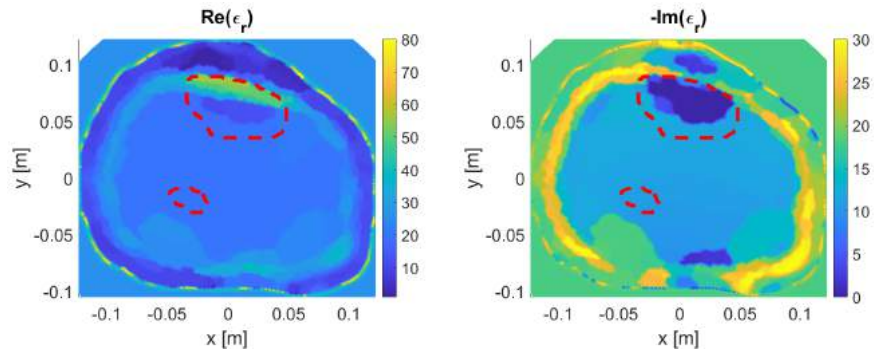




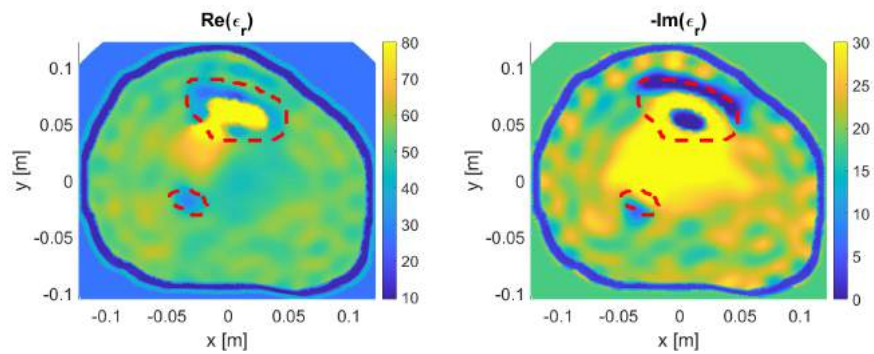
(a) Homogenous background



(b) Inhomogeneous background with mid layer

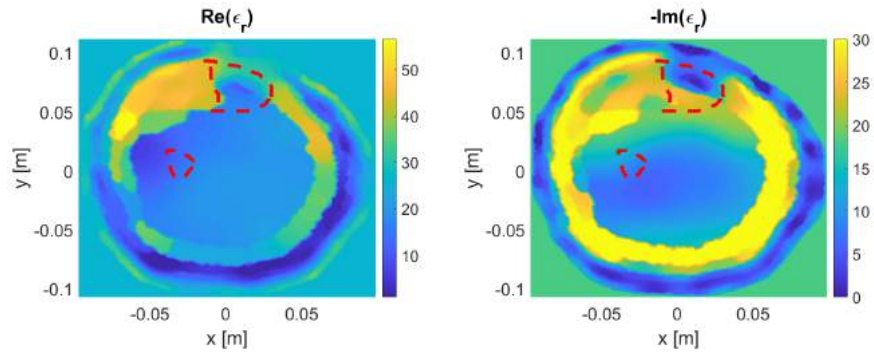


(c) Inhomogeneous background with skin-fat layer

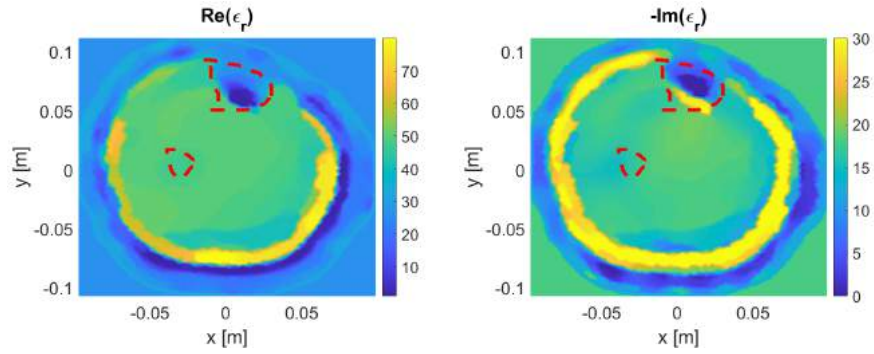


(d) Inhomogeneous background with skin-fat-muscle layer

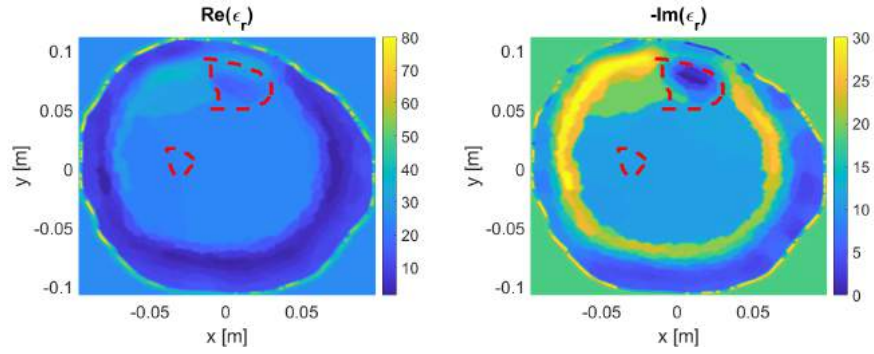
Figure 4.11: Varying imaging domain to enhance MRI model 1 reconstruction.



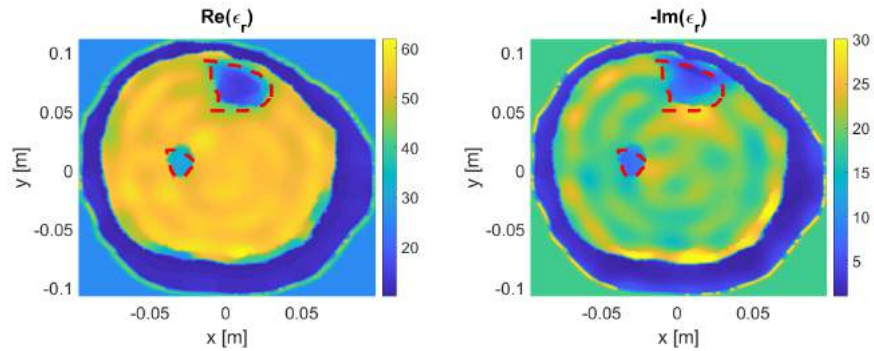
(a) Homogenous background



(b) Inhomogeneous background with mid layer

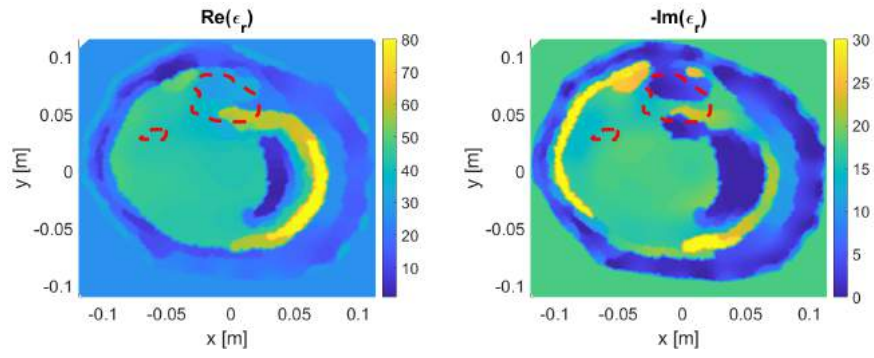


(c) Inhomogeneous background with skin-fat layer

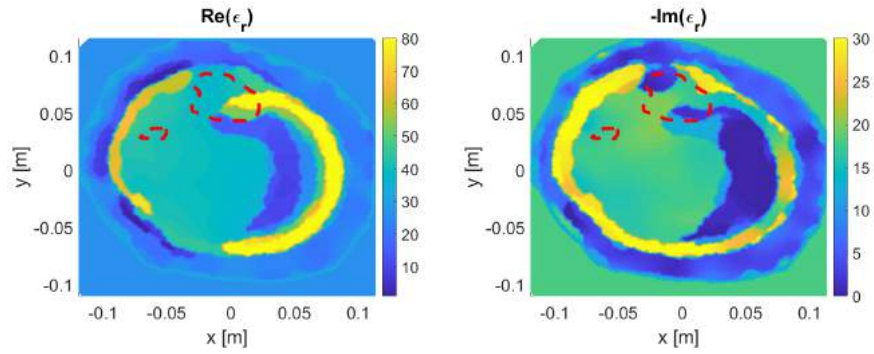


(d) Inhomogeneous background with skin-fat-muscle layer

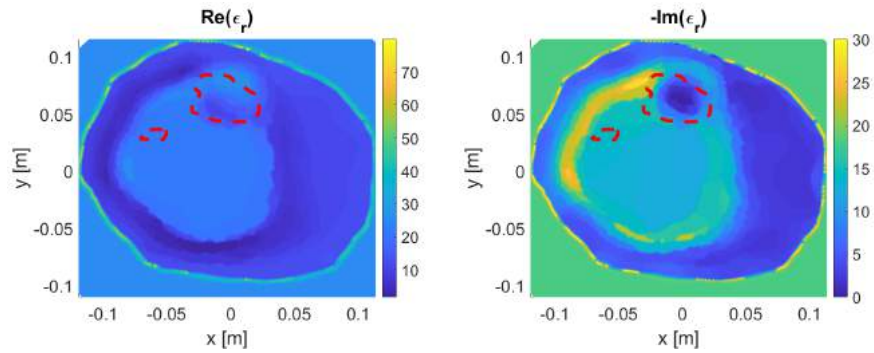
Figure 4.12: Varying imaging domain to enhance MRI model 2 reconstruction.



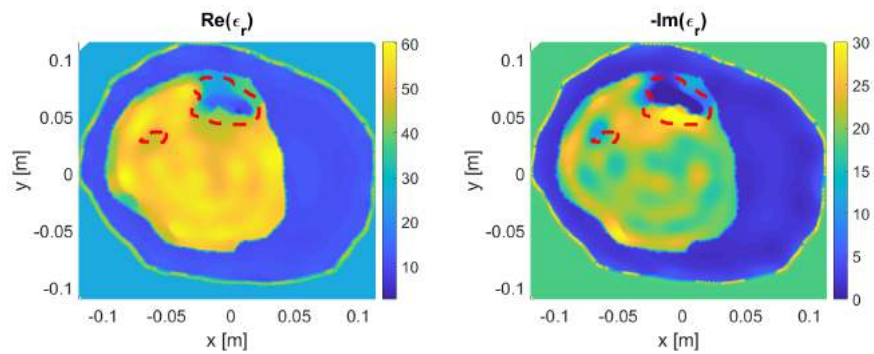
(a) Homogenous background



(b) Inhomogeneous background with mid layer



(c) Inhomogeneous background with skin-fat layer



(d) Inhomogeneous background with skin-fat-muscle layer

Figure 4.13: Varying imaging domain to enhance MRI model 3 reconstruction.

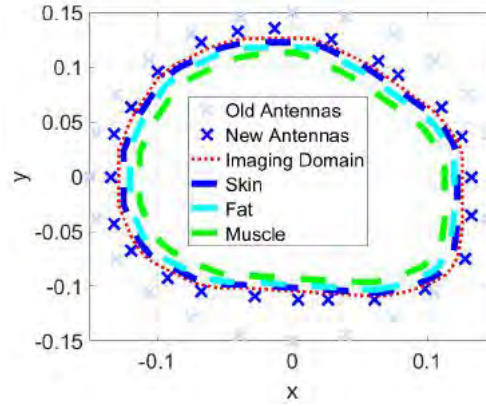


Figure 4.14: Old and new antennas' locations for MRI model 1.

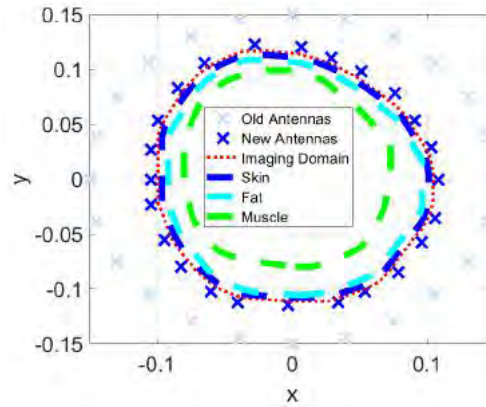


Figure 4.15: Old and new antennas' locations for MRI model 2.

the antennas were adjusted to surround the contour of a breast using a secondary ultrasound system. In [31], the results showed that by having the antennas located in a close distance from the OI improved tumor localization results, in comparison to having the antennas' on a circular surface.

In this thesis, the outermost layer within each MRI model is selected to provide the surface for the antennas' locations. To prevent the inclusion of antennas within the imaging domain, the antennas' surface was extruded slightly beyond the MRI model outermost contour. Figures 4.14, 4.15, and 4.16 show the old and new surfaces on which the antennas were located for MRI models 1, 2, and 3, respectively. It should be noted that for each case the antennas follow the the skin layer of the leg, which would be the case for a wearable MWT system.



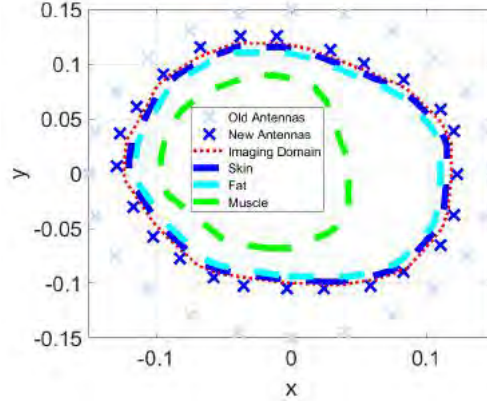


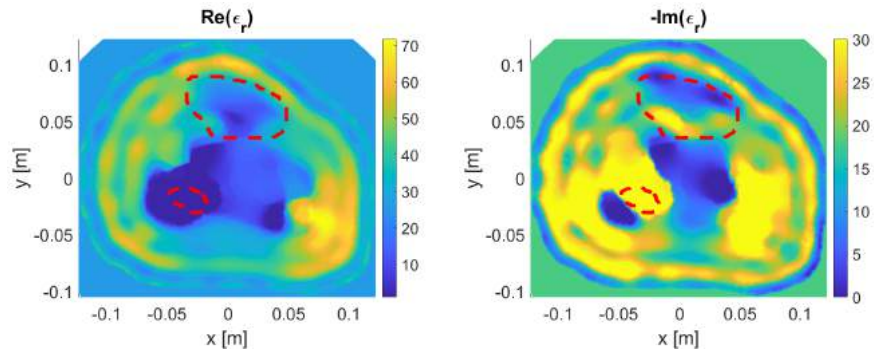
Figure 4.16: Old and new antennas' locations for MRI model 3.

Since the antennas' locations were changed, new synthetic data were obtained for each model by running the forward simulations again. Next, for each MRI model, the inversion algorithm was ran again for four background scenarios: homogeneous background and the three cases of inhomogeneous background. The FEM-CSI reconstructions are shown in Figures 4.17, 4.18, and 4.19 for MRI models 1, 2, and 3, respectively. The analysis and discussion of results are given in Section 4.5.

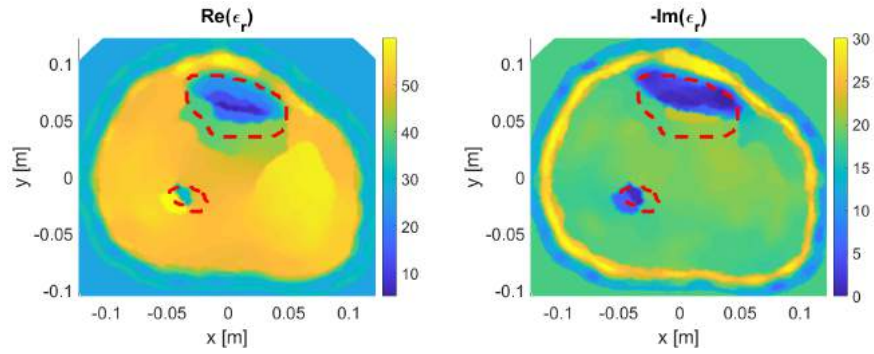
#### 4.4. Changing the Matching Medium

In this section, the effect of changing the type of matching medium is investigated. So far, for all the simulations done, the selected matching medium was a mixture of glycerin and water. This matching medium was used as it have been shown to be very effective in biomedical MWT applications as it reduces the reflections at the matching medium/skin interface. The disadvantage of this mixture is that it is liquid and will not be suitable for a wearable MWT applications.

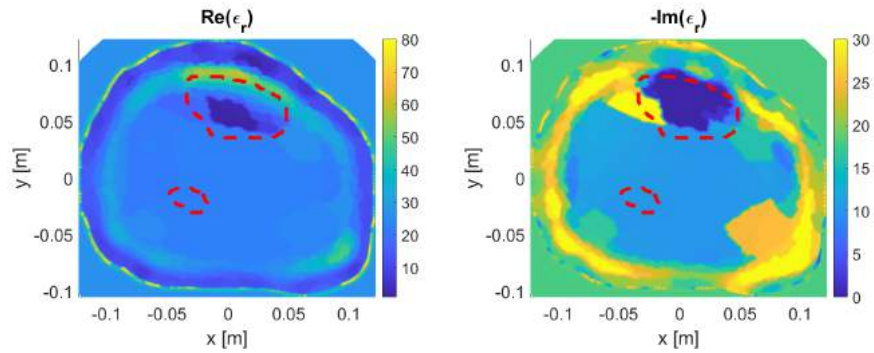
A commonly used matching medium for medical imaging purposes is the ultrasound gel. The ultrasound gel is aqueous, bacterio-static, non-sensitizing, and non-irritating. Further, since it is of a gel-form it can be easily applied and cleaned in a wearable MWT system. The world standard for ultrasound gels is the AquaSonic 100 [51]. There has been no previous research on the use of AquaSonic 100 ultrasound gels in microwave tomographic applications; thus it will be investigated as a matching medium in this thesis.



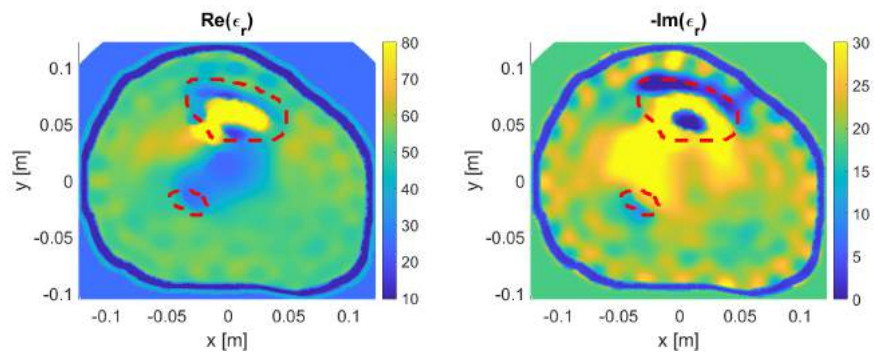
(a) Homogenous background



(b) Inhomogeneous background with mid layer

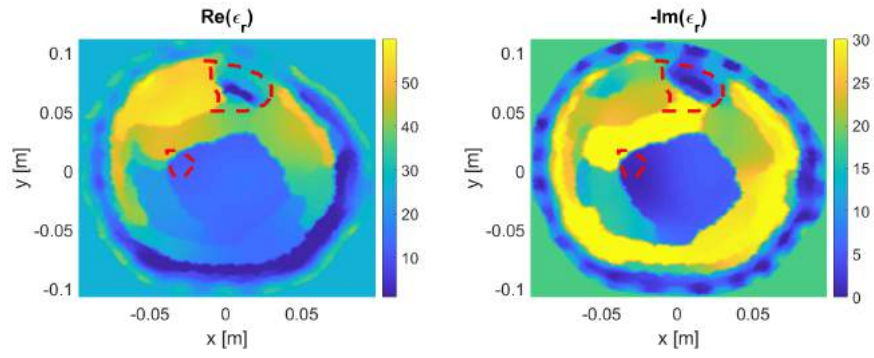


(c) Inhomogeneous background with skin-fat layer

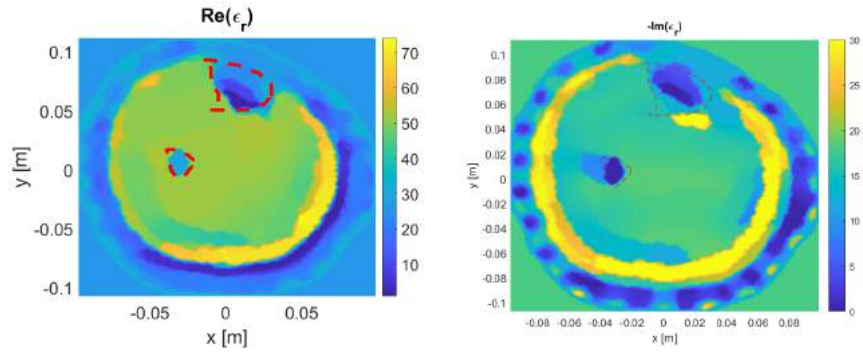


(d) Inhomogeneous background with skin-fat-muscle layer

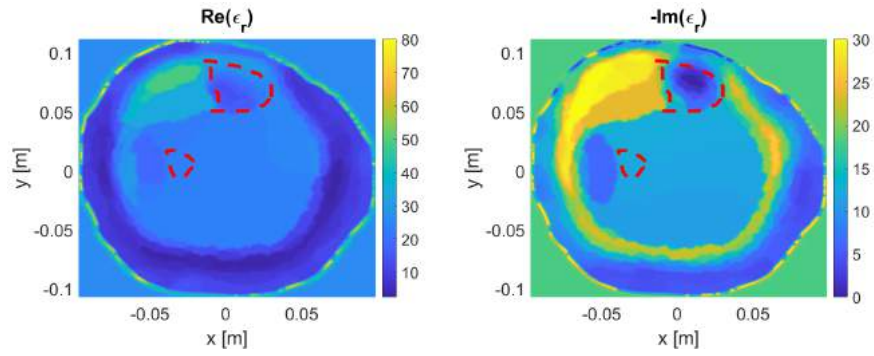
Figure 4.17: Changing location of antennas to enhance MRI model 1 reconstruction.



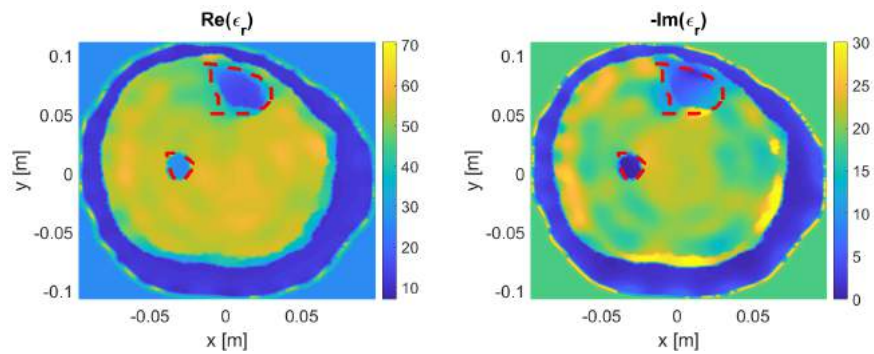
(a) Homogenous background



(b) Inhomogeneous background with mid layer

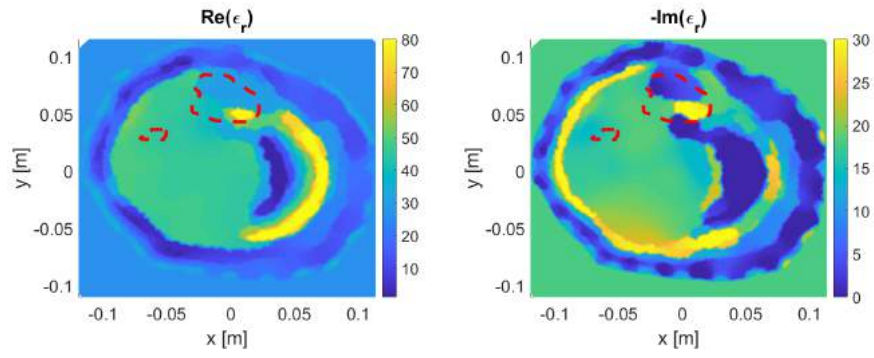


(c) Inhomogeneous background with skin-fat layer

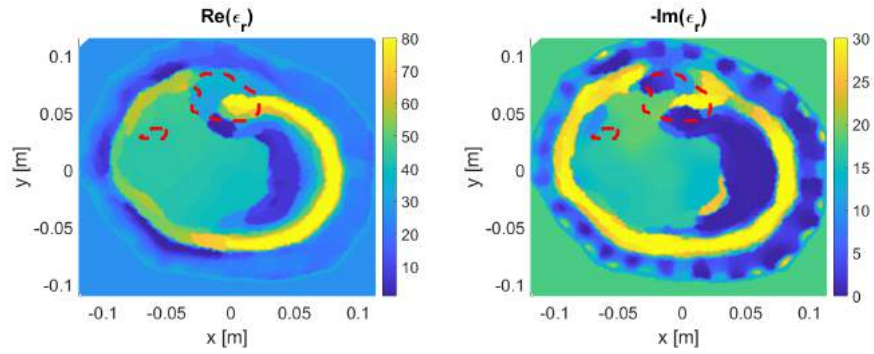


(d) Inhomogeneous background with skin-fat-muscle layer

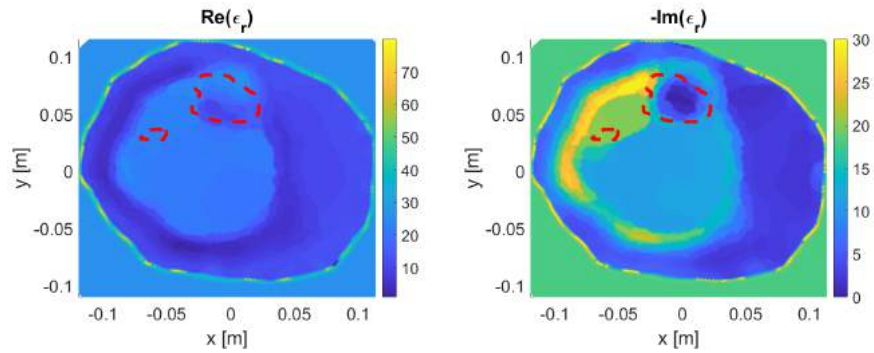
Figure 4.18: Changing location of antennas to enhance MRI model 2 reconstruction.



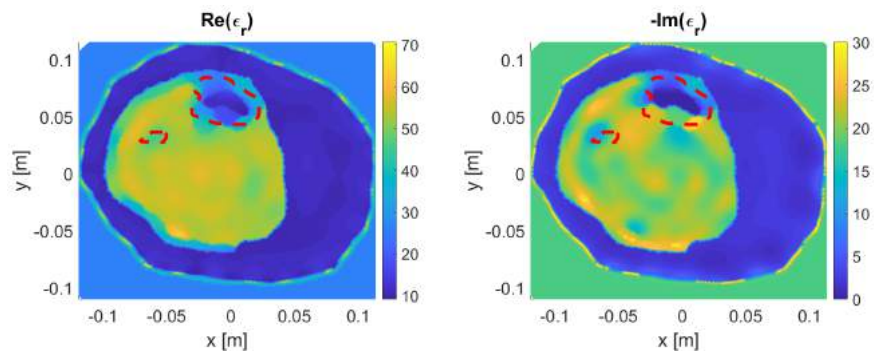
(a) Homogenous background



(b) Inhomogeneous background with mid layer



(c) Inhomogeneous background with skin-fat layer



(d) Inhomogeneous background with skin-fat-muscle layer

Figure 4.19: Changing location of antennas to enhance MRI model 3 reconstruction.



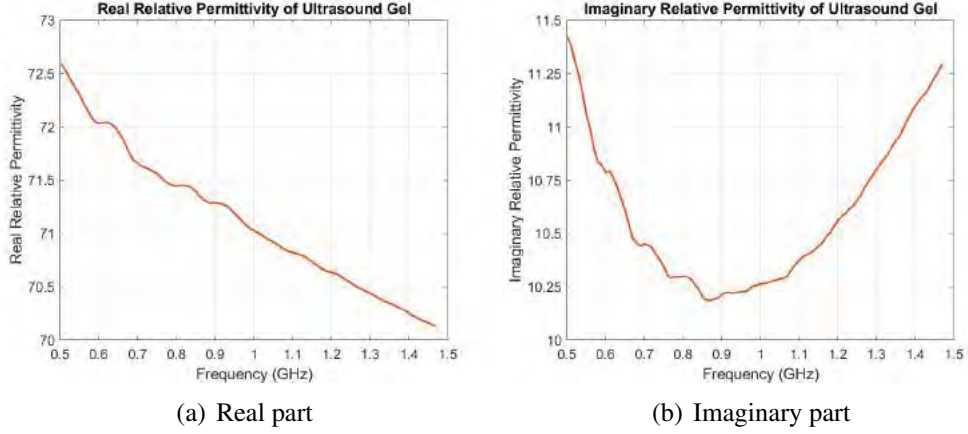


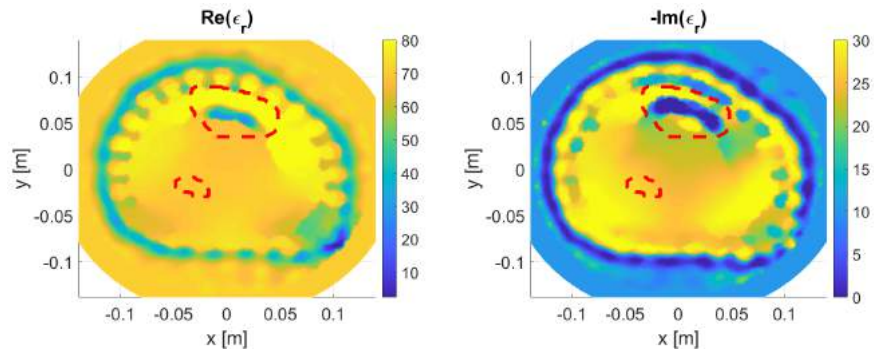
Figure 4.20: Relative permittivity values of AquaSonic 100 ultrasound gel.

To be able to use AquaSonic 100 as a matching medium, its electrical properties need to be known. This was not found in literature so it was measured in the microwave engineering lab at the American University of Sharjah using Keysight's N1501A Coaxial Dielectric Probe [52]. The procedure for performing the measurement is summarized in Appendix 7. The measured real and imaginary part of the relative permittivity for a frequency range of 0.5 – 1.5 GHz is shown in Fig. 4.20.

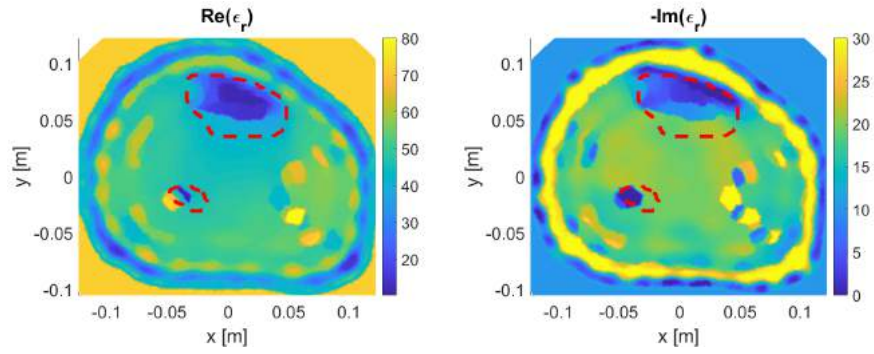
From Fig. 4.20, the value of the complex relative permittivity at 0.8 GHz is  $\epsilon_r = 71.4 - j10.3$  for the AquaSonic 100 ultrasound gel. Using this value of matching medium, the inversion algorithm was allowed to run again under the four background scenarios: homogeneous background and the three cases of inhomogeneous background. In these inversions, the modified imaging domain and antennas' locations were used based on the results of Section 4.2 and Section 4.3. Figures 4.21, 4.22, and 4.23 show the results for MRI models 1, 2, and 3, respectively. The analysis and discussion of results are given in Section 4.5.

#### 4.5. Analysis and Observations

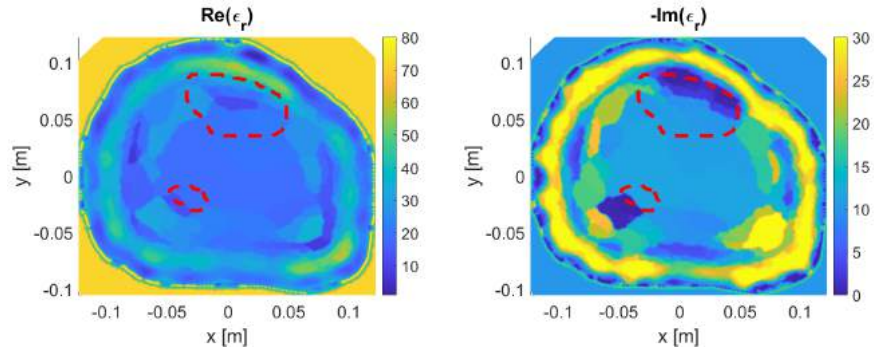
The incorporation of prior information resulted in an improved image reconstruction process. In all three scenarios, the reconstructed images became smoother and easier to analyze in terms of OI and bone locations. In the mid value layer inhomogeneous background scenario, there was no significant change in the reconstructed images compared to the skin-fat and skin-fat-muscle scenarios. In addition, the skin-fat-



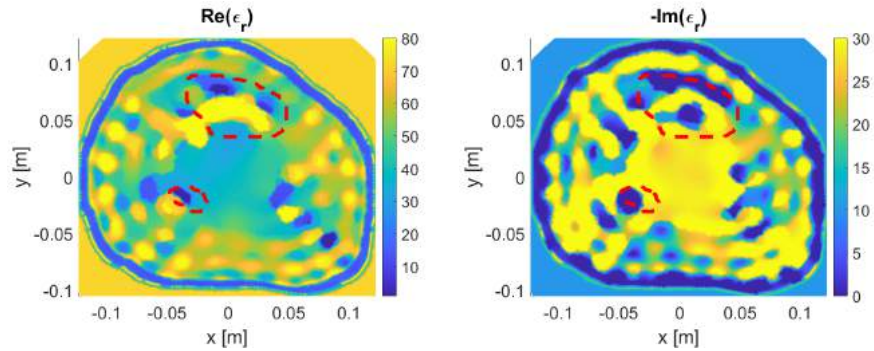
(a) Blind Inversion



(b) Inhomogeneous background with mid layer

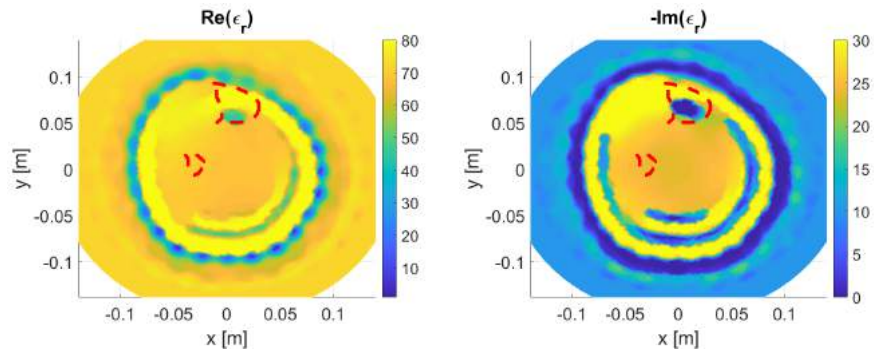


(c) Inhomogeneous background with skin-fat layer

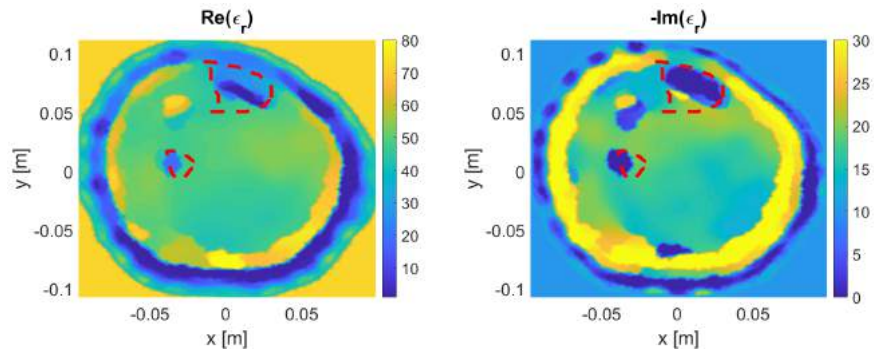


(d) Inhomogeneous background with skin-fat-muscle layer

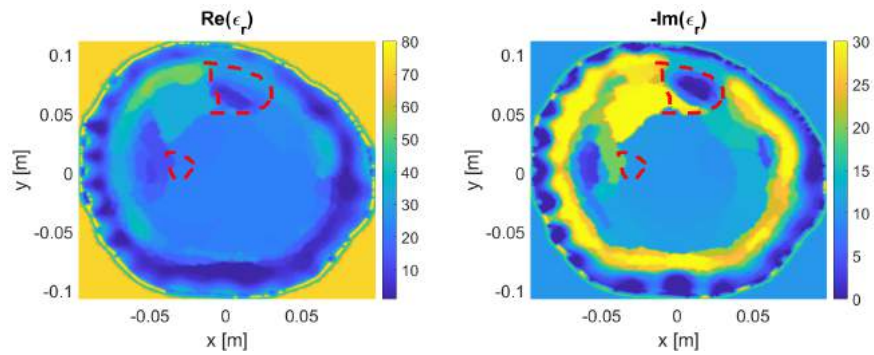
Figure 4.21: The effect of using ultrasound gel as matching medium for MRI model 1



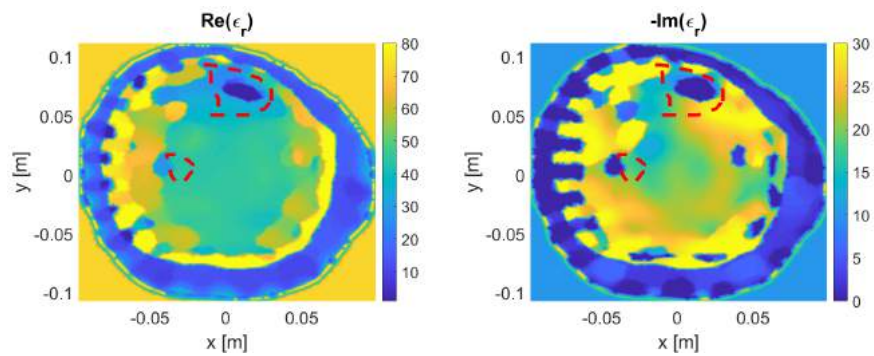
(a) Blind Inversion



(b) Inhomogeneous background with mid layer



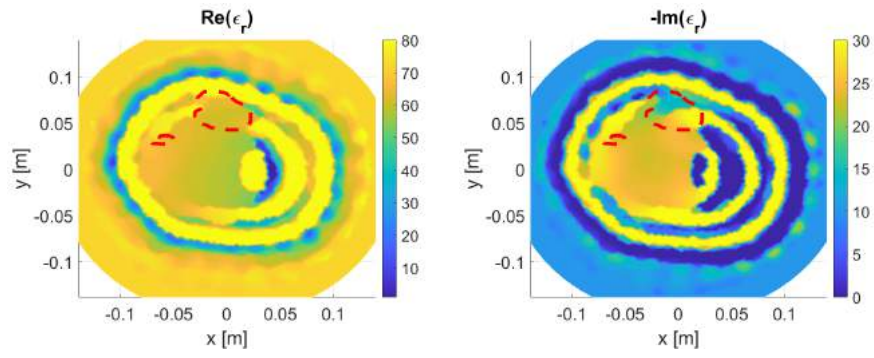
(c) Inhomogeneous background with skin-fat layer



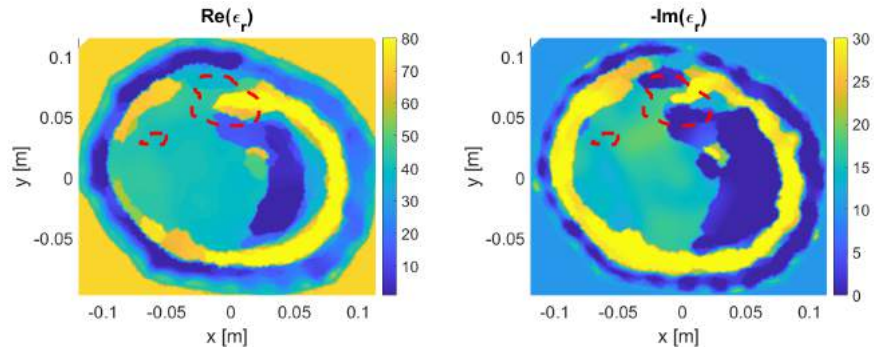
(d) Inhomogeneous background with skin-fat-muscle layer

Figure 4.22: The effect of using ultrasound gel as matching medium for MRI model 2

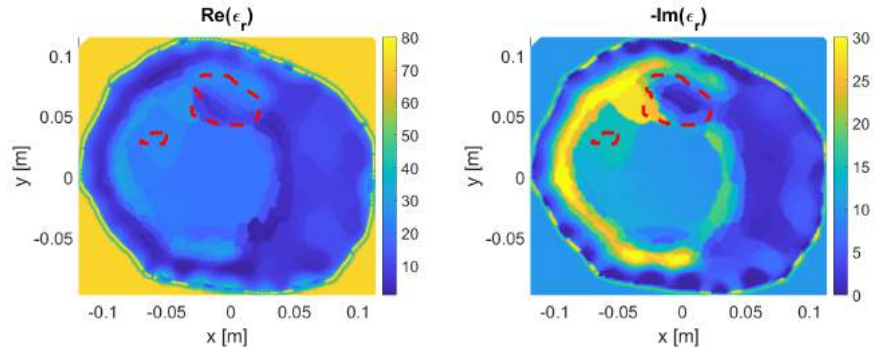




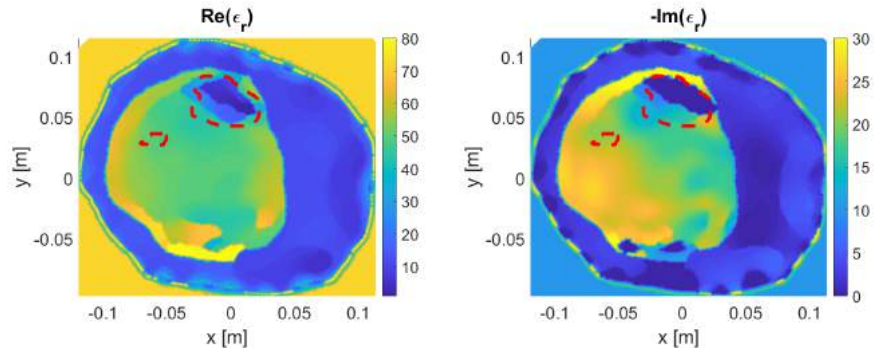
(a) Blind Inversion



(b) Inhomogeneous background with mid layer



(c) Inhomogeneous background with skin-fat layer



(d) Inhomogeneous background with skin-fat-muscle layer

Figure 4.23: The effect of using ultrasound gel as matching medium for MRI model 3

muscle scenario succeeded in locating the smaller bone which was missing in previous scenarios. However, it still not clear and ready for further analysis.

The change in the imaging domain boundaries added to the improvements discussed before. The mid value scenario provided better images that could be improved further in order to estimate the missing bone, the fibula. In addition, the location of both bones became clearer using the skin-fat-muscle inhomogeneous scenario. The change in imaging domain allowed for less regions to be reconstructed within the inversion image.

After varying the location of antennas, the image reconstruction process in all three models got improved. In addition, the location of the smaller bone, the fibula, got detected and reconstructed successfully in multiple inhomogeneous background scenarios. The best scenarios were the mid value and the skin-fat-muscle in terms of estimating bone size. The change in antennas locations suggests the possibility of using flexible antennas surrounding the OI preparing it for wearable applications.

The additional ultrasound gel provided good reconstruction process. The location of both bones was close to the actual model in the mid layer inhomogeneous scenario. The skin-fat and skin-fat-muscle provided a better reconstructed images, especially for the thick fat model; which is MRI model 3.

In all enhancement procedures, it can be easily noted that when having a thicker fat layer within the OI, it is better to use lower values of inhomogeneous background to obtain better bone localization. This can be seen in MRI model 3 throughout all enhancement procedures mentioned in previous sections.

To elaborate more on that, Tables 4.1, 4.2, and 4.3 show the mean value of the real part relative permittivity of the tibia and fibula bone for MRI models 1, 2, and 3, respectively. The process of extracting bones is discussed in details in Chapter 6. Each cell includes three values: the mean value of the relative permittivity ( $\epsilon_r^{\text{mean}}$ ), the standard deviation, and the relative percentage error (%error). The relative percentage error is calculated using the following equation,

$$\%error = \frac{\epsilon_r^{\text{mean}} - \epsilon_r^{\text{actual}}}{\epsilon_r^{\text{actual}}} \times 100. \quad (31)$$

Table 4.1: Bones mean value real part relative permittivity in MRI model 1.

	Homogeneous Background (Blind Inversion)	Inhomogeneous Background		
		Case I	Case II	Case III
		<i>mid value</i>	<i>skin-fat</i>	<i>skin-fat-muscle</i>
Circular Imaging Domain and Circular Antennas	16.57, 2.47 (27.43%)	25.72, 2.05 (97.87%)	5.71, 0.26 (-56.09%)	39.36, 3.92 (201.80%)
	Not Detected	Not Detected	Not Detected	38.32, 1.16 (194.74%)
Imaging Domain based on OI and Circular Antennas	15.58, 3.71 (19.84%)	18.45, 2.28 (41.89%)	12.21, 0.60 (-6.07%)	33.51, 6.14 (157.73%)
	Not Detected	Not Detected	Not Detected	33.00, 2.27 (153.88%)
Imaging Domain based on OI and Antennas based on OI	12.86, 3.07 (-1.11%)	12.21, 3.51 (-6.11%)	2.51, 2.08 (-80.70%)	31.75, 6.06 (144.26%)
	1.00, 0.01 (-92.31%)	30.80, 0.02 (136.94%)	Not Detected	27.11, 1.38 (108.53%)
Matching Medium (US)	41.39, 7.27 (218.39%)	13.07, 1.04 (0.53%)	14.82, 3.65 (13.98%)	14.62, 7.66 (12.49%)
	Not Detected	13.20, 4.16 (1.55%)	12.34, 0.02 (-5.06%)	2.63, 3.20 (-79.78%)

Table 4.2: Bones mean value real part relative permittivity in MRI model 2.

	Homogeneous Background (Blind Inversion)	Inhomogeneous Background		
		Case I	Case II	Case III
		<i>mid value</i>	<i>skin-fat</i>	<i>skin-fat-muscle</i>
Circular Imaging Domain and Circular Antennas	21.07, 1.06 (62.11%)	28.20, 1.07 (116.94%)	12.02, 1.05 (-7.56%)	24.60, 4.92 (89.24%)
	Not Detected	Not Detected	Not Detected	34.34, 1.63 (164.13%)
Imaging Domain based on OI and Circular Antennas	14.65, 1.91 (12.67%)	5.71, 4.67 (-56.08%)	17.30, 1.07 (33.10%)	15.04, 0.33 (15.69%)
	Not Detected	Not Detected	Not Detected	30.08, 0.39 (131.40%)
Imaging Domain based on OI and Antennas based on OI	6.73, 5.54 (-48.26%)	6.19, 4.09 (-52.42%)	14.99, 0.73 (-15.29%)	14.52, 0.34 (11.67%)
	Not Detected	28.57, 0.02 (119.77%)	18.64, 0.02 (43.37%)	26.37, 0.15 (102.84%)
Matching Medium (US)	48.25, 2.74 (271.12%)	4.23, 3.77 (-67.48%)	8.58, 2.04 (-34.02%)	1.01, 0.02 (-92.25%)
	Not Detected	18.85, 0.08 (45.02%)	15.26, 0.68 (17.40%)	27.82, 0.17 (114.03%)

Table 4.3: Bones mean value real part relative permittivity in MRI model 3.

	Homogeneous Background (Blind Inversion)	Inhomogeneous Background		
		Case I	Case II	Case III
		<i>mid value</i>	<i>skin-fat</i>	<i>skin-fat-muscle</i>
Circular Imaging Domain and Circular Antennas	30.81, 1.00 (137.01%)	32.02, 0.27 (146.29%)	12.36, 0.51 (-4.92%)	21.95, 2.56 (68.87%)
	Not Detected	Not Detected	Not Detected	Not Detected
Imaging Domain based on OI and Circular Antennas	28.01, 2.83 (115.47%)	34.71, 4.15 (167.02%)	12.64, 1.62 (-2.77%)	13.00, 2.35 (0.03%)
	Not Detected	Not Detected	Not Detected	Not Detected
Imaging Domain based on OI and Antennas based on OI	29.40, 1.31 (126.14%)	30.75, 4.27 (136.55%)	11.44, 1.57 (-11.98%)	12.05, 1.31 (-7.34%)
	Not Detected	44.50, 0.68 (242.28%)	Not Detected	47.57, 1.11 (265.92%)
Matching Medium (US)	Not Detected	33.74, 2.69 (159.52%)	8.70, 1.40 (-33.08%)	3.57, 1.60 (-72.56%)
	Not Detected	Not Detected	Not Detected	Not Detected

Here  $\epsilon_r^{\text{mean}}$  is the extracted mean value for the real part of the bones' relative permittivity and  $\epsilon_r^{\text{actual}}$  is the actual value for the real part of the bones' relative permittivity obtained from literature [5, 16]. When the reconstructed bones are over-estimated than the actual literature value, the relative percentage error is positive. On the other hand, when the reconstructed bones are under-estimated than the actual literature value,

the relative percentage error is negative. In the tables, the standard deviation reflects the amount of variations in data points within the extracted bones segments. Higher standard deviation value indicates that the mask used to extract bones could be smaller to cover bones only. This helps in the manual extraction process to be described in Chapter 6. If a bone is not clearly visible in the reconstruction process, it is marked as *Not Detected*.

It can be noted from the tables that the lowest relative percentage error occurred when relocating the imaging domain as well as the antennas to be surrounding the OI's outermost contour. In addition, the fibula bone becomes detectable as the imaging domain and the antennas are closer to the OI. The closest mean value of relative permittivity occurs when using the mid-value inhomogeneous background scenarios for MRI models 1 and 2. On the other hand, the skin-fat and skin-fat-muscle inhomogeneous background scenarios provided better reconstruction results for MRI model 3. The effect of the enhancement procedure is clearly shown when using the ultrasound gel matching medium, as the percentage error gets heavily reduced to below 100% in almost the three MRI models.

The following points can be concluded by the end of this chapter,

- The incorporation of prior information related to the structure and dielectric properties improves the reconstruction process in terms of having smoother boundaries.
- The less the imaging domain area, the better the reconstruction and the less the number of unknown mesh nodes.
- There is a possibility of changing the location of antennas to surround the OI boundaries and having much more efficient image reconstruction process, which helps when building a wearable system. The localization of bones and permittivity values extracted provided reliable results.
- The use of AquaSonic 100 ultrasound gel provided good reconstructed images, which is considered promising as it is the world standard for medical ultrasound imaging.

- When having a thick fat layer within the OI, it is better to use the skin-fat scenario as the Inhomogeneous background for better reconstruction in terms of both bone localization and relative permittivity values.

Considering these points, it is a challenge to obtain structural information about the OI and modify the imaging domain and antennas location in a real MWT configuration. In this chapter, the boundaries were determined using the actual MRI models; however, such models are not available when performing real MWT measurements without the usage of multiple imaging modalities. Therefore, the next chapter provides a complete procedure to extract structural information using only MWT reconstruction processes to overcome the issues discussed earlier.



## Chapter 5: Image Processing for Enhanced Reconstruction

In this chapter, a complete procedure of estimating the OI's structural information using an image processing technique is proposed and discussed. The procedure is based on the usage of k-means clustering technique applied to the blind inversion reconstructions of the relative complex permittivity images. The main goal of this section is to obtain structural information about the OI, thus, building the corresponding estimated models. The analysis and observations are provided by the end of the chapter to evaluate the results and compare it to the outcomes of the previous chapter in terms of the reconstruction results.

### 5.1. K-means Clustering

K-means clustering is an image processing technique based on S. Lloyd algorithm [53] that has been used commonly in the process of partitioning images and data sets. In this technique, the selected image is iteratively segmented into a certain number of clusters. Each cluster includes all the values within the image that are close to each other [54]. To elaborate more on that, the objective of the k-means clustering algorithm is to minimize the following function,

$$\operatorname{argmin}_{S_k} \sum_{k=1}^K \sum_{x \in S_k} \|x - \mu_k\|^2. \quad (32)$$

Here  $k$  is index of a cluster,  $K$  is the total number of clusters,  $S_k$  is the set of pixels within the  $k^{\text{th}}$  cluster of an image, and  $\|x - \mu_k\|^2$  is the Euclidean distance between a selected pixel  $x$  in  $S_k$  and a cluster centroid  $\mu_k$ . This Euclidean distance is given as,

$$\|x - \mu_k\|^2 = \sqrt{(x - \mu_k)^2}. \quad (33)$$

At the beginning, the algorithm assigns a cluster centroid uniformly at random from the set of pixels  $S$ . Then, the distance between each pixel and the centroid is

calculated and denoted as  $d(x_m, \mu_k)$ , where  $x_m$  is the initial selected pixel. The second centroid is calculated at random with a probability of,

$$P(\mu_k) = \frac{d^2(x_m, \mu_1)}{\sum_{i=1}^n d^2(x_i, \mu_1)}. \quad (34)$$

Here  $n$  is the total number of pixels at  $S$ . Then, each pixel distance is calculated from each cluster centroid and assigned to its nearest cluster. The selection of new cluster centroids keeps on changing iteratively with a probability of,

$$P(\mu_k) = \frac{d^2(x_m, \mu_p)}{\sum_{x \in C_k} d^2(x_h, \mu_p)}. \quad (35)$$

Here,  $C_k$  is the set of pixels within cluster  $k$  with centroid  $\mu_k$ . The algorithm stops when the iteration reaches the maximum number.

## 5.2. Structural Information Extraction Procedure

In the previous chapter, investigations were carried out on the effect of using the MRI models to incorporate prior information about the structure of the OI. However, in a real MWT configuration, the forward problem model boundaries, which are the actual OI boundaries, are not known. In addition, the knowledge about the structure of the OI is usually done by using multiple imaging modalities such as MRI or ultrasound [31] along with the MWT system. This is reflected in making the imaging process costly and time consuming.

Therefore, to obtain structural information about the OI being imaged, the blind inverted images are used to build an estimated model of the OI using k-means clustering. By taking a closer look into the results of the blind inversion algorithm, it can be noted that there are differences between layers within the OI in terms of permittivity values. Thus, k-means clustering could be useful in separating such layers and obtaining unique data points corresponding to their boundaries.

Several image segmentation techniques were tested beforehand including thresholding, region based, and clustering. However, the most reliable outcomes came from the k-means clustering algorithm. Within the k-means technique, images are automatically classified into regions/clusters based on their differences in data points values. This got an advantage for MWT images, as usually over- and under- estimations occur

for values with different layers within images. Therefore, thresholding or region based techniques would fail. In addition, different layers might overlap when reconstructing their dielectric profile images, which makes it even harder to predict a behavior of the imaging algorithm.

The complete procedure of image enhancement using k-means clustering is shown in Fig. 5.1.

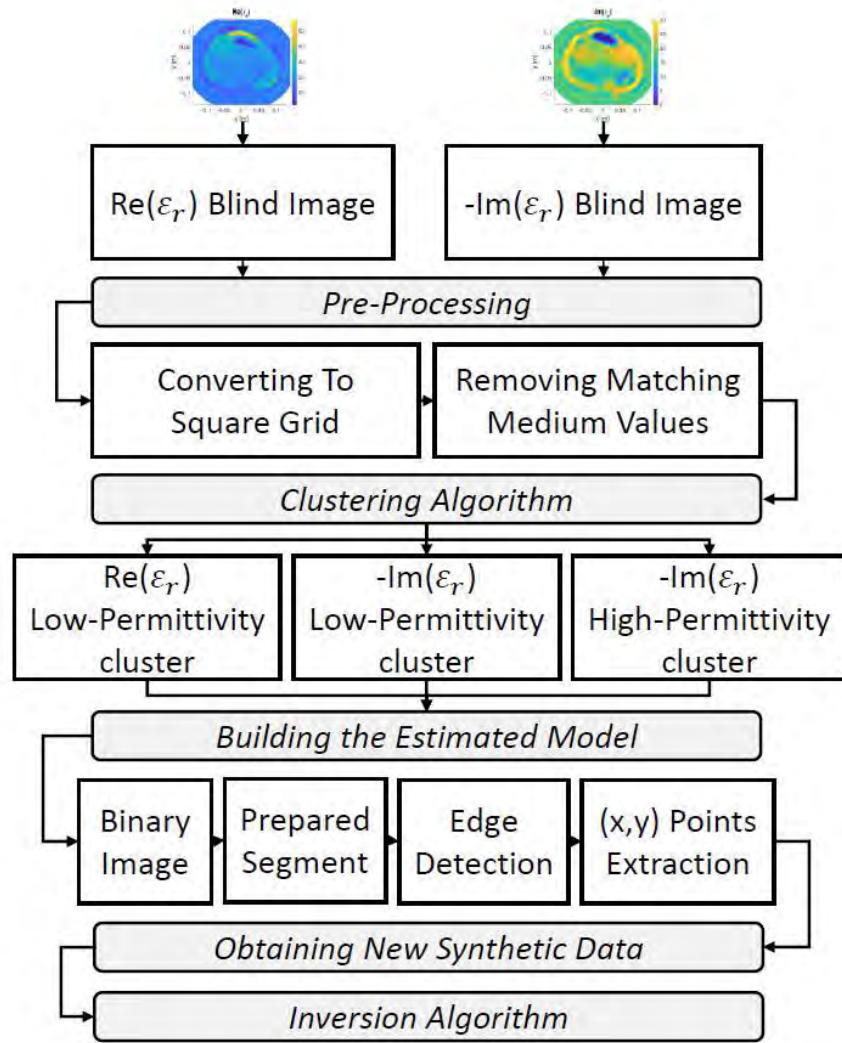


Figure 5.1: Reconstruction enhancement using k-means clustering algorithm complete procedure.

### 5.3. Pre-Processing

Before going further with the k-means algorithm, the reconstructed blind images should be modified such that it is suitable for the k-means functionality. First, all reconstructed images are converted from triangular mesh images to square grid images; k-means technique is designed square grid meshes. Secondly, all values corresponding to the surrounding matching medium are extracted based on the matching medium relative permittivity values.

**5.3.1. Conversion to a square grid.** In the inverse problem solving section, the contrast and contrast source calculations are done on the nodes of the triangles within each MRI model mesh. Therefore, values corresponding to the real and imaginary part of the relative complex permittivity within the reconstructed images can not be used directly in the clustering algorithm as they are required to be on a square grid. Therefore, the dielectric properties values on nodes are transformed to a square grid.

To do this, a function that is embedded within the FEM solver [46] is used, which creates a connectivity matrix that maps the values on the nodes of triangles to the locations at the square grid. This process is done using elemental basis functions of FEM to evaluate a variable  $\epsilon_r^p$ , which is the relative permittivity value at the  $p$  square grid pixel.

First the centroid of a square  $p$  in the grid is located within a triangle  $e$  in the 2D triangular mesh. This centroid has 2D coordinate  $(x^p, y^p)$ . Next, in terms of FEM,  $\epsilon_r^p(x^p, y^p)$  is calculated as,

$$\epsilon_r^p(x^p, y^p) = \sum_{l=1}^3 \epsilon_{r,l}^e \lambda_l^e(x^p, y^p). \quad (36)$$

Here  $l$  is the local number of the nodes within the selected triangle  $e$ ,  $\epsilon_{r,l}^e$  is the dielectric value on the node, and  $\lambda_l^e$  is the linear basis function and is given by,

$$\lambda_l^e(x^p, y^p) = \frac{1}{2A^e} (a_l^e + b_l^e x^p + c_l^e y^p) \quad (37)$$

where  $A^e$  is the area of the triangle, and  $a_l^e$ ,  $b_l^e$ , and  $c_l^e$  are triangle coefficients given as,

$$a_l^e = x_2^e y_3^e - y_2^e x_3^e \quad (38)$$

$$b_l^e = y_2^e - y_3^e \quad (39)$$

$$c_l^e = x_3^e - x_2^e \quad (40)$$

The coefficients of  $l = 1, 2$ , and  $3$  are calculated interchangeably. The area of the triangle shown in equation (37) is given by,

$$A^e = \frac{1}{2} \begin{vmatrix} 1 & x_1^e & y_1^e \\ 1 & x_2^e & y_2^e \\ 1 & x_3^e & y_3^e \end{vmatrix}. \quad (41)$$

Here  $x_{1,2,3}^e$  and  $y_{1,2,3}^e$  are the  $x$ - and  $y$ - coordinates of nodes in the selected triangle  $e$ .

These equations are used to find the value of the relative permittivity for each pixel in the square grid using the values of the relative permittivity on the nodes of the triangular mesh.

**5.3.2. Extraction of the matching medium.** After obtaining the square grid of pixels for the relative complex permittivity blind images, the matching medium values are extracted before applying any further calculations. The purpose of doing such step is to ensure that the k-means algorithm only includes the OI reconstructed relative permittivity values within its calculations of clusters. As the reconstructed images are always non-uniform and may over- or under- estimate the actual value of the relative permittivity, the extracted matching medium values are set to lie within a boundary limit of  $\{+4, -3\}$  from the actual value of the real part, and  $\{+4, -1\}$  from the actual value

of the imaginary part. The selection of an optimum boundary limit was determined after several trial and error tests; these selected ranges worked on every model efficiently.

The matching mediums used were 80:20 Glycerin/Water solution and Aqua-Sonic 100 ultrasound gel. The ranges of extracted values for Glycerin/Water mixture were of  $23 \leq \epsilon'_r \leq 30$  and  $17 \leq \epsilon''_r \leq 22$ . The ranges of extracted values for ultrasound gel were  $68.4 \leq \epsilon'_r \leq 75.4$  and  $10.3 \leq \epsilon''_r \leq 15.3$ .

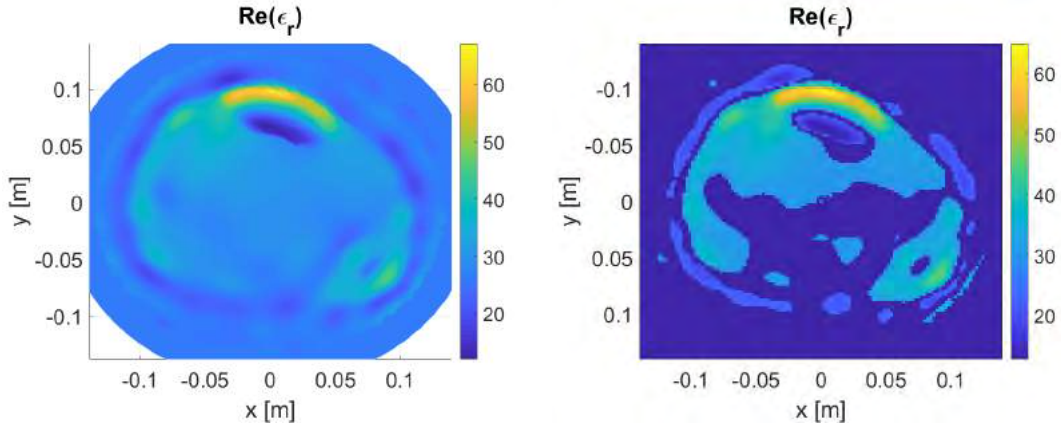
Figures 5.2 and 5.3 shows the extraction process for the three MRI models within the real and imaginary part using the Glycerin/Water solution. In addition, Figures 5.4 and 5.5 show the extraction process for the three MRI models using the ultrasound gel real and imaginary parts. The figures on the left column are the reconstructions, while the figures on the right are after conversion to a square grid and matching medium removal.

The extraction process successfully removed the pixels that are related to the matching medium. However, in some images, few pixels had relative permittivity values that are outside the boundary limit. In the next subsections, a detailed procedure on the removal of such parts from images is provided. In addition, some of the values that are related to the OI values were extracted. However, it is considered fine as the main objective of the whole procedure is to obtain boundaries of the layers regardless of the missing values inside them.

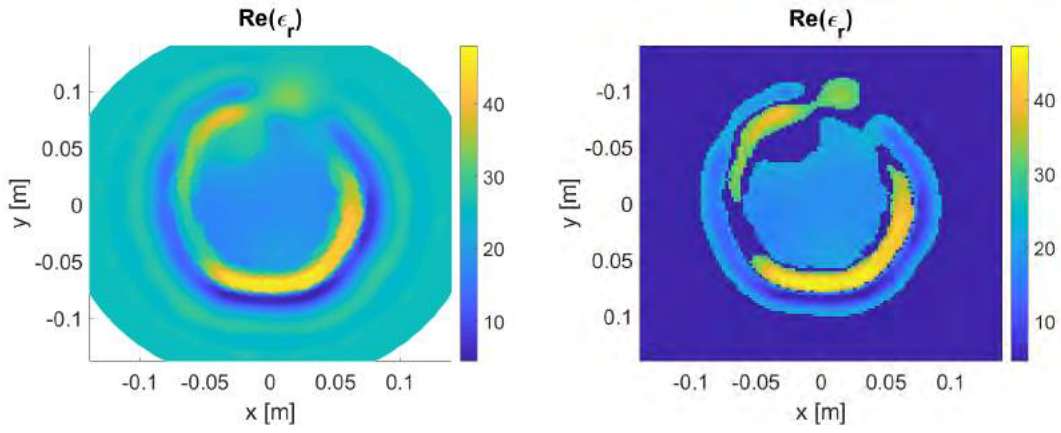
#### 5.4. Clustering Algorithm

After removing almost all relative permittivity pixels that correspond to the surrounding matching medium, boundaries of different layers become extractable. From the results provided in Section 5.3, it can be seen from the resulting figures that the removal of the matching medium resulted in having almost two regions. These regions are referred to as *Low-Permittivity* and *High-Permittivity* regions relative to their permittivity values of both real and imaginary parts. The *Low-Permittivity* region has values close to the fat and bone relative permittivity values. The *High-Permittivity* region has values close to the muscle and skin relative permittivity values. Therefore, the number of clusters,  $K$ , is set to be 2.

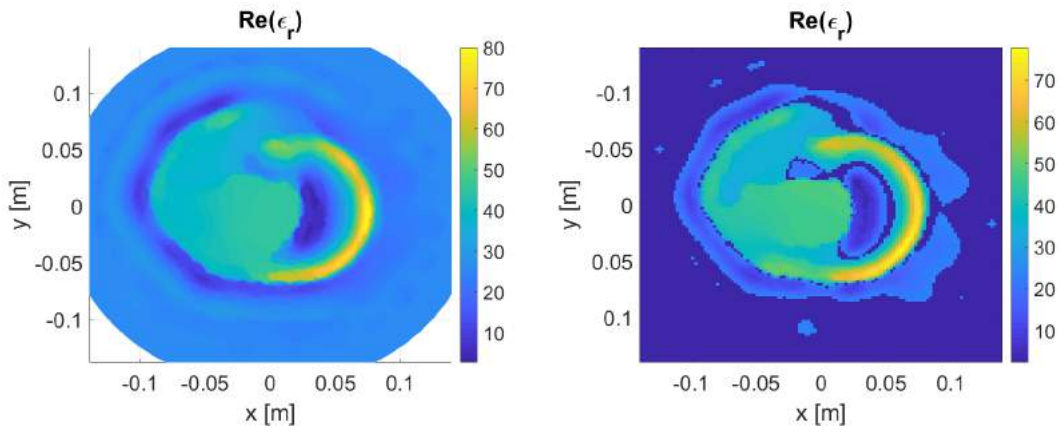
The *Low-Permittivity* and *High-Permittivity* regions extracted from the real part of the relative complex permittivity reconstructions are shown Fig. 5.6 using Glyc-



(a) MRI model 1

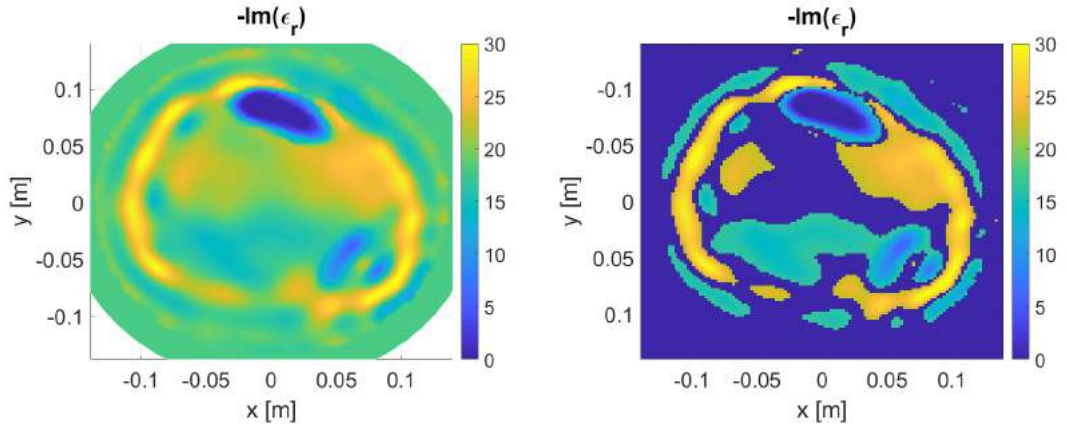


(b) MRI model 2

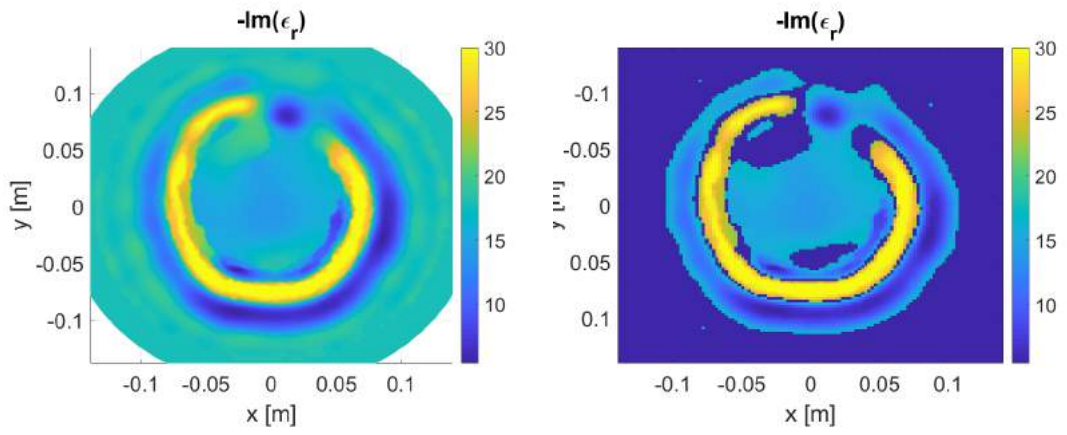


(c) MRI model 3

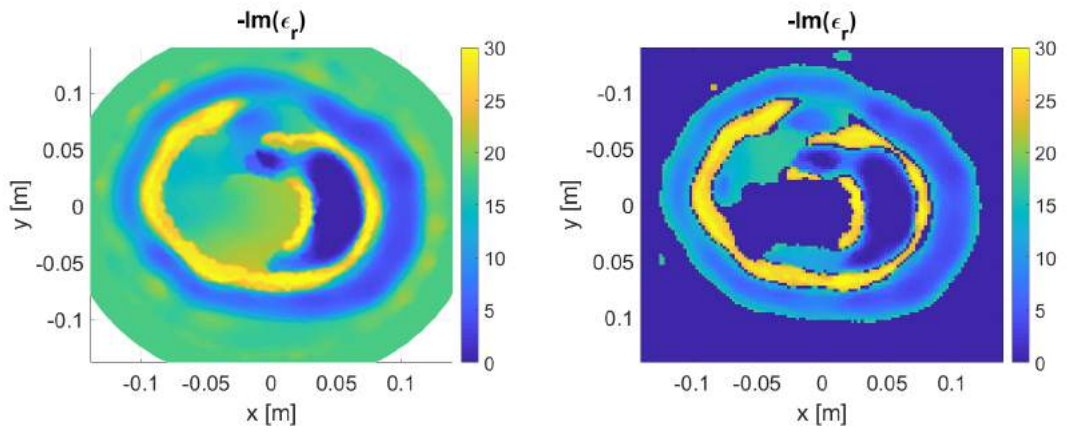
Figure 5.2: The extraction process of the Glycerin/Water matching medium real part values in MRI models 1, 2, and 3.



(a) MRI model 1



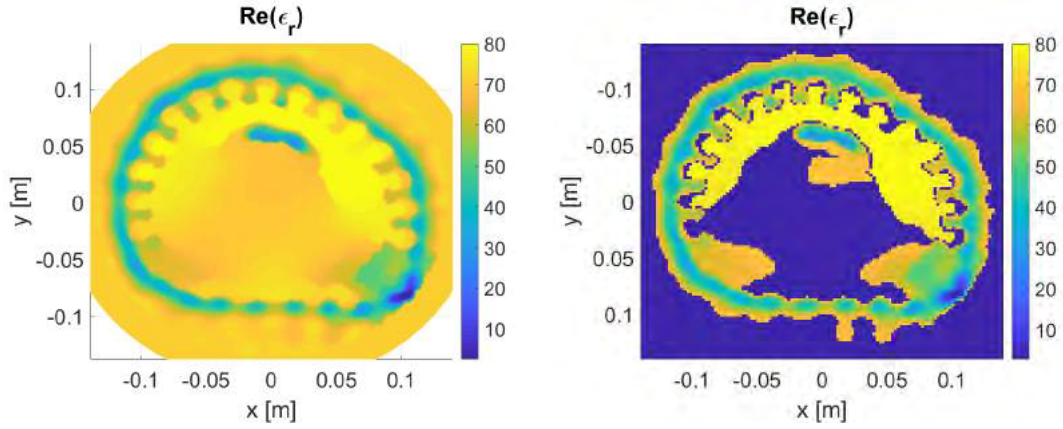
(b) MRI model 2



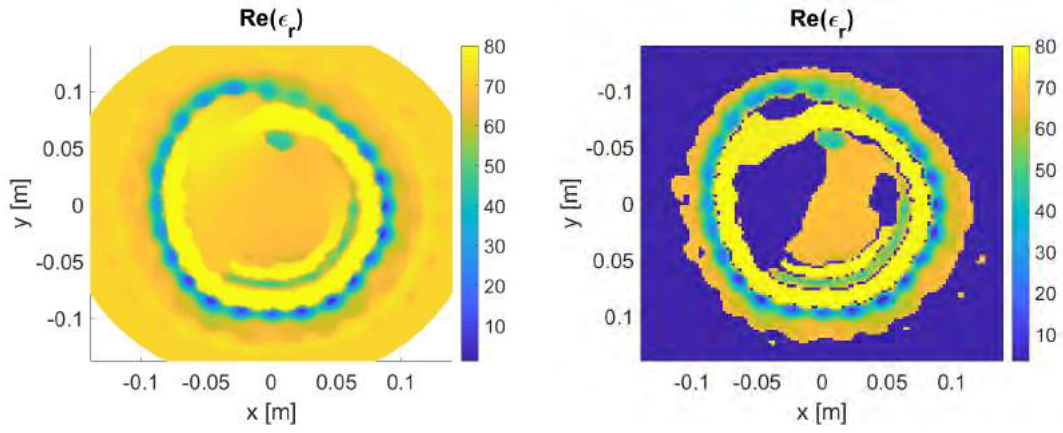
(c) MRI model 3

Figure 5.3: The extraction process of the Glycerin/Water matching medium imaginary part values in MRI models 1, 2, and 3.

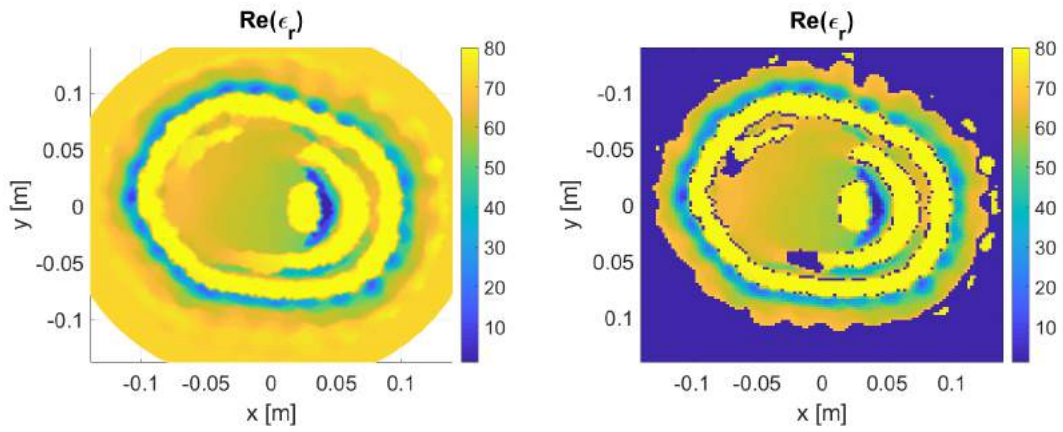




(a) MRI model 1

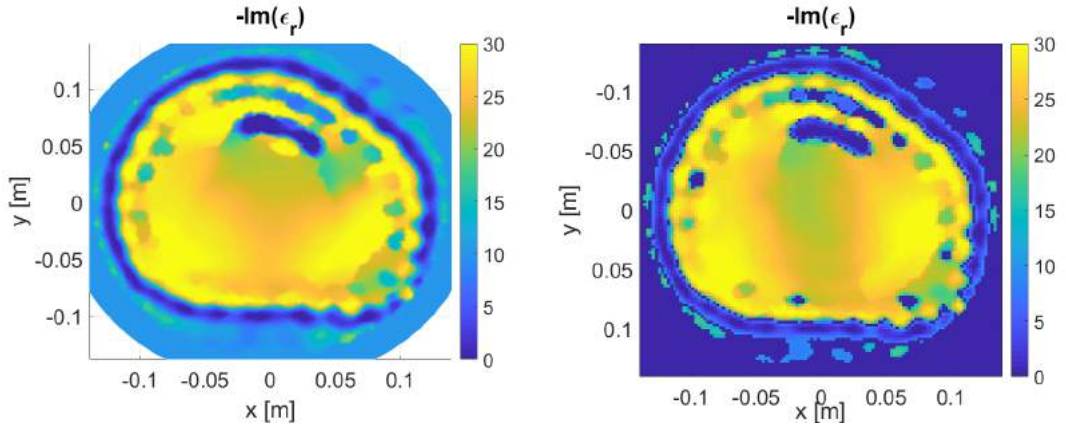


(b) MRI model 2

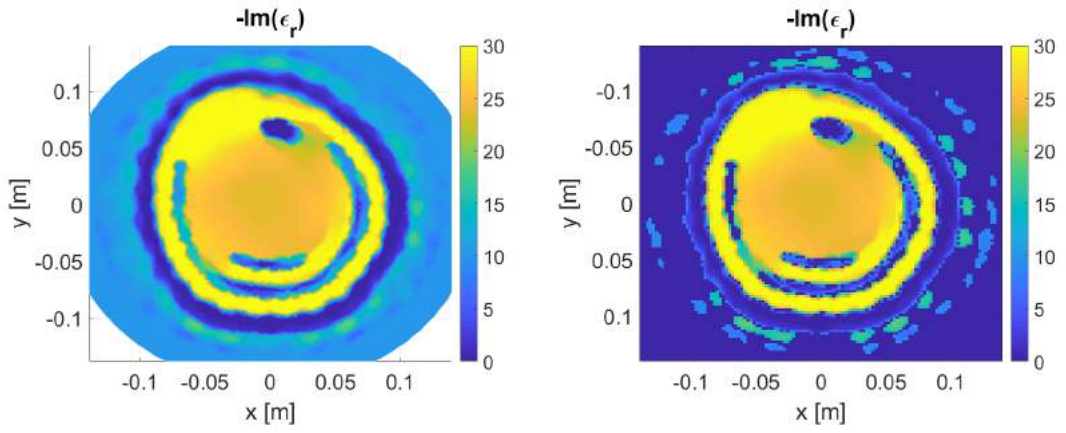


(c) MRI model 3

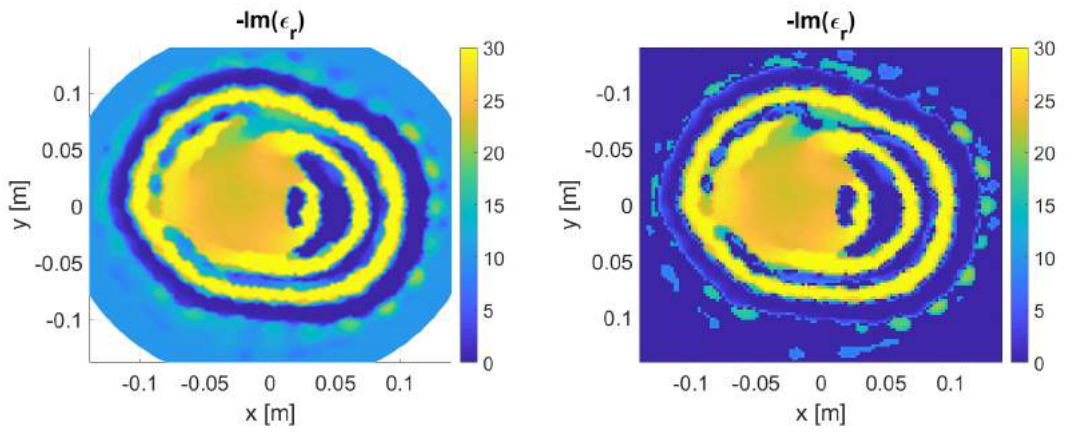
Figure 5.4: The extraction process of the ultrasound gel matching medium real part values in MRI models 1, 2, and 3.



(a) MRI model 1



(b) MRI model 2



(c) MRI model 3

Figure 5.5: The extraction process of the ultrasound gel matching medium imaginary part values in MRI models 1, 2, and 3.

erin/Water solution and Fig. 5.7 using ultrasound gel. The figures are for the three MRI models 1, 2, and 3.

From the acquired clusters, it can be seen that the *Low-Permittivity* cluster resulted in obtaining the fat layer segment correctly. However, the *High-Permittivity* cluster was not clearly segmenting the muscle layer in all MRI models. In addition, it included some values that are considered as underestimated matching medium values. Based on this, the algorithm is allowed to use the *Low-Permittivity* cluster only, which contains fat reconstructed boundaries, to build the estimated model. The outermost boundary of the OI, which is related to the skin, is determined by extruding the boundary location of the extracted fat layer outwards by a small value. This will represent the skin surrounding the fat layer, which is usually millimeters in thickness.

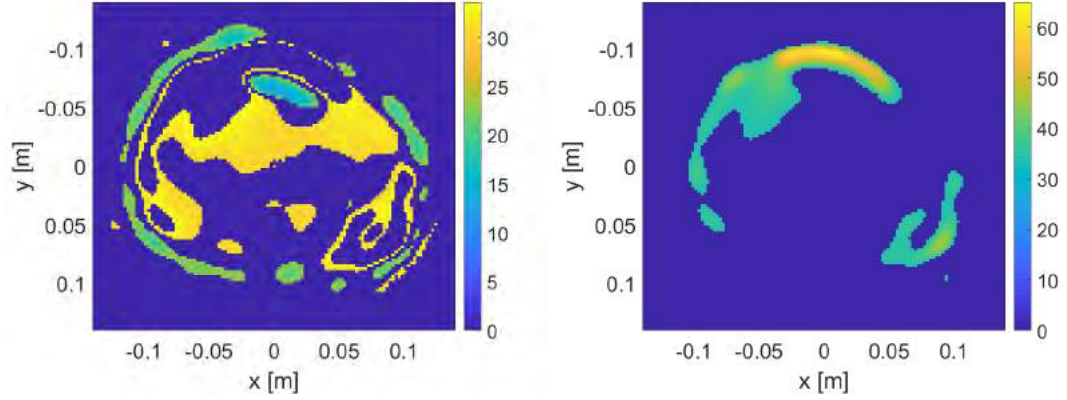
Further, the cluster technique described earlier is also applied on the imaginary part of the reconstructed images following the same procedure of obtaining the *High-Permittivity* and *Low-Permittivity* regions. The results are shown in Figures 5.8 and 5.9 for Glycerin/Water solution and ultrasound gel matching media, respectively.

The clustering of the imaginary part resulted in better segments for both fat and muscle. Unlike the real-part clustering, the imaginary-part clustering can be used to reconstruct both the structure of the fat and muscle regions. Thus, both *Low-Permittivity* and *High-Permittivity* regions are selected to build the estimated model.

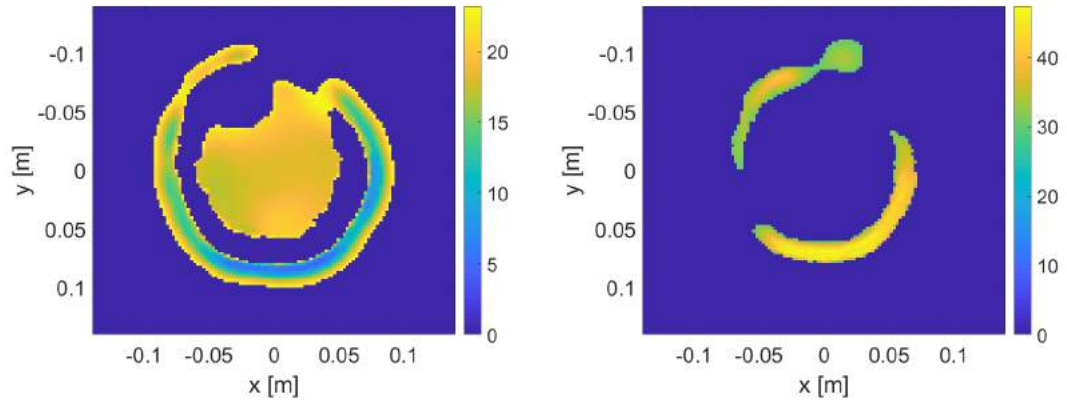
### **5.5. Building the Estimated Model**

In this section, selected k-means clusters are used to generate an estimated model of the original OI structure. Thus, acquiring structural information about layers within the OI being imaged.

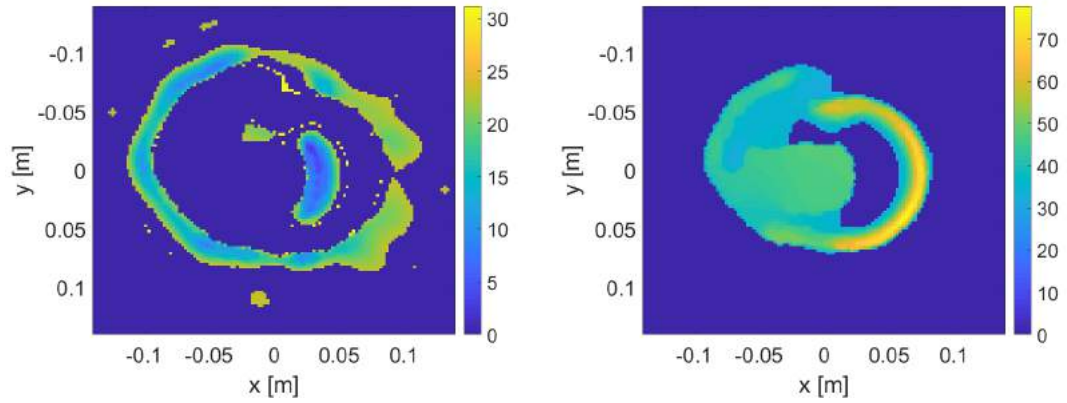
To achieve this, outermost boundaries of each cluster should be detected. This is done by creating a binary image using the clusters obtained from k-means algorithm. The binary image is generated as follows: in the output image containing k-means clusters, if a pixel in the square grid is in a k-mean cluster a values of '1' is assigned to it, otherwise it is assigned a value of '0'. The resulted binary images will include smaller clusters that are located near the main target segments, which are fat and muscle tissues; these smaller clusters are removed to ensure the extraction process includes only the fat and muscles segments. Next, edge detection is applied on the remaining segments to



(a) MRI model 1



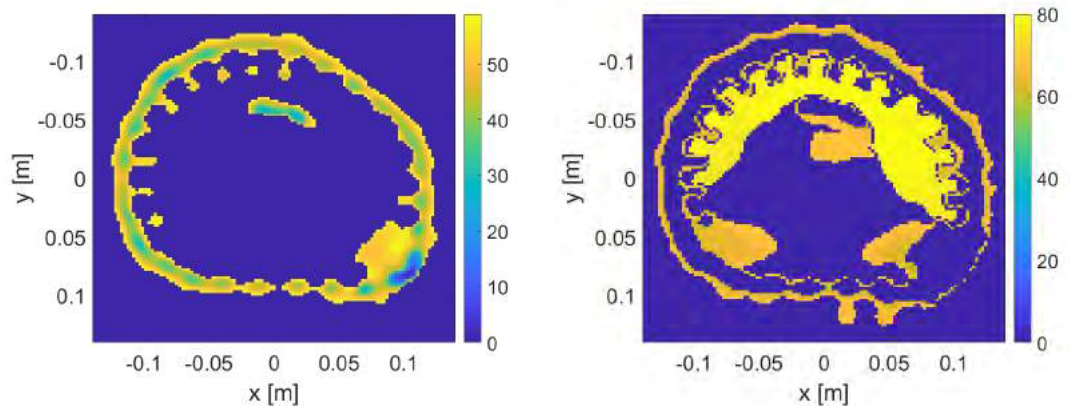
(b) MRI model 2



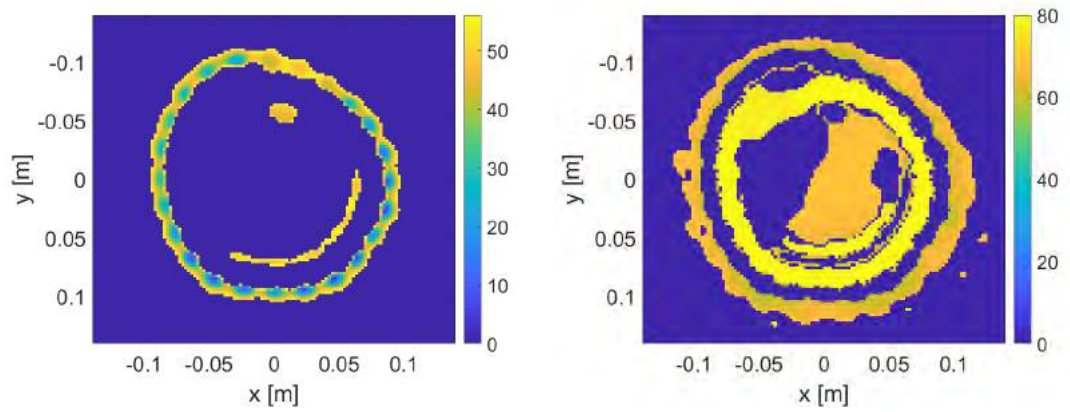
(c) MRI model 3

Figure 5.6: K-means clusters from the real part relative permittivity images in MRI models 1, 2, and 3 using Glycerin/Water solution (Left = *Low-Permittivity*, Right = *High-Permittivity*).

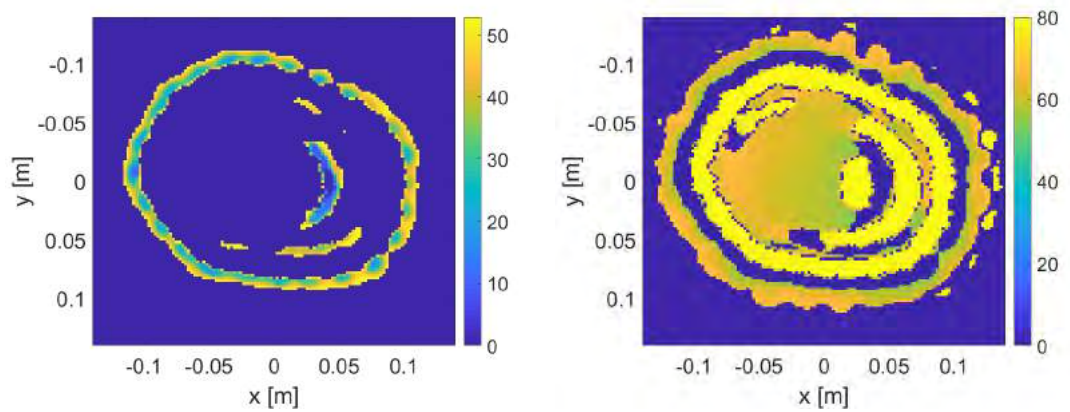




(a) MRI model 1

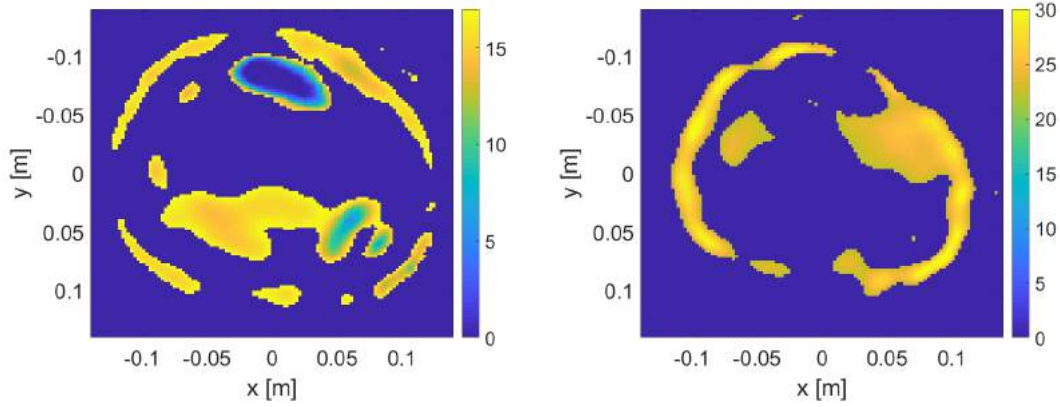


(b) MRI model 2

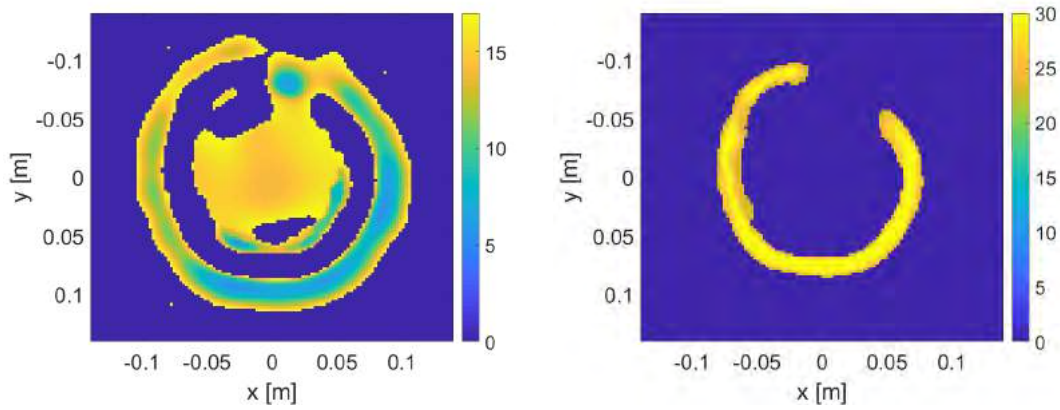


(c) MRI model 3

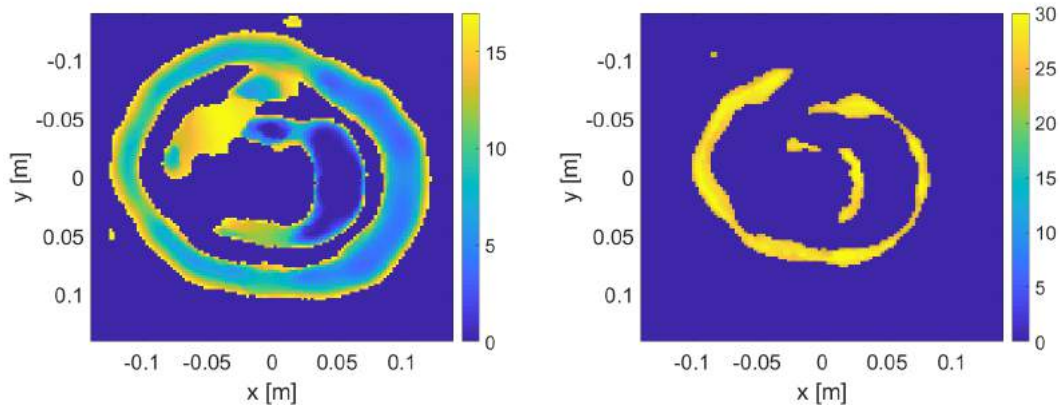
Figure 5.7: K-means clusters from the real part relative permittivity images in MRI models 1, 2, and 3 using ultrasound gel (Left = *Low-Permittivity*, Right = *High-Permittivity*).



(a) MRI model 1

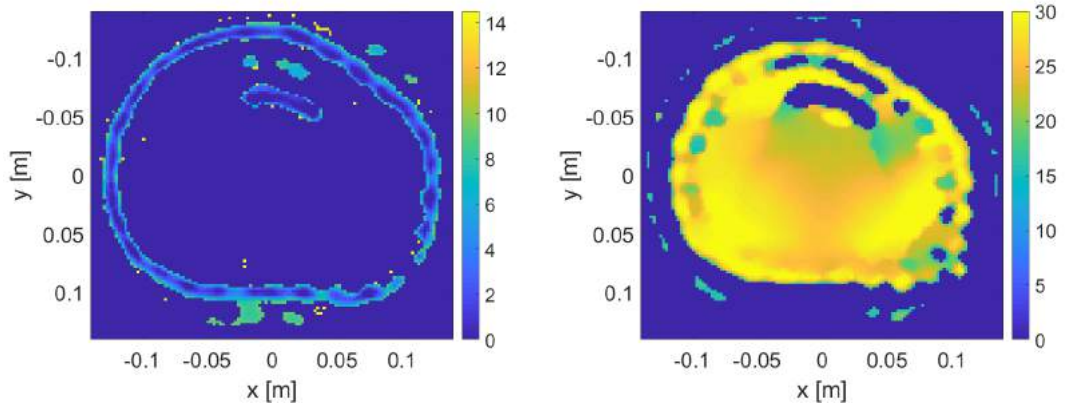


(b) MRI model 2

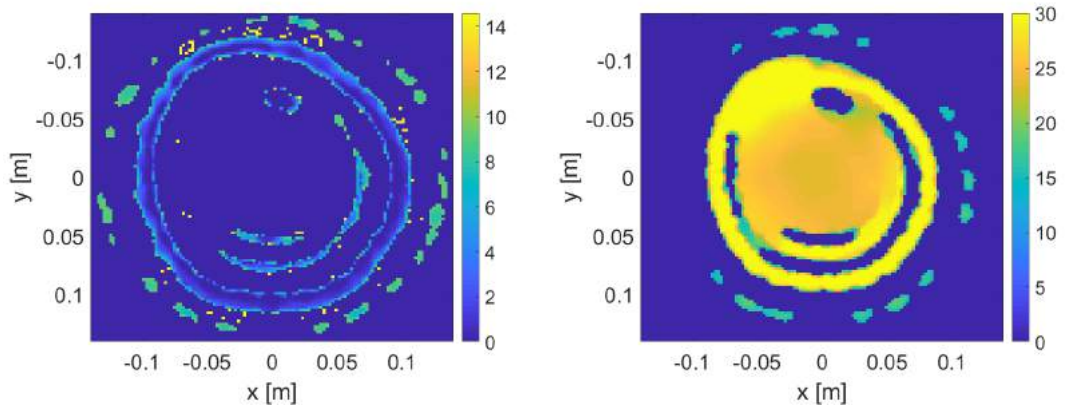


(c) MRI model 3

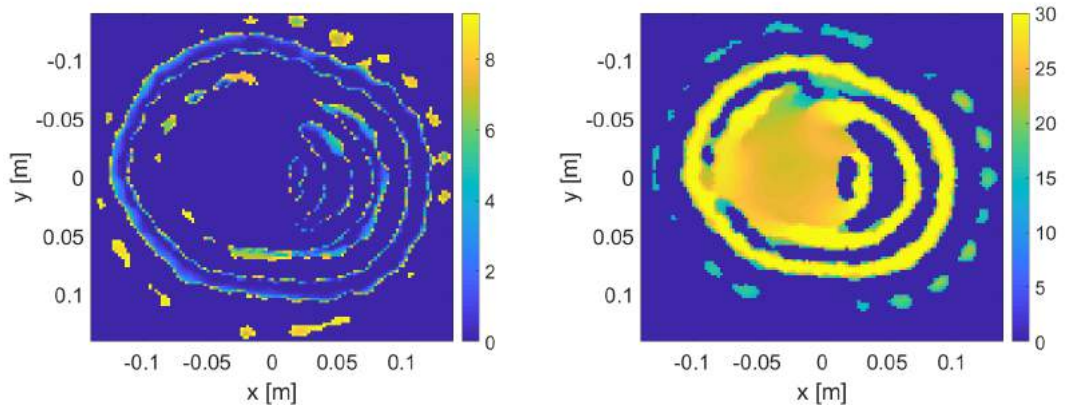
Figure 5.8: K-means clusters from the imaginary part relative permittivity images in MRI models 1, 2, and 3 using Glycerin/Water solution (Left = *Low-Permittivity*, Right = *High-Permittivity*).



(a) MRI model 1



(b) MRI model 2



(c) MRI model 3

Figure 5.9: K-means clusters from the imaginary part relative permittivity images in MRI models 1, 2, and 3 using ultrasound gel (Left = *Low-Permittivity*, Right = *High-Permittivity*).

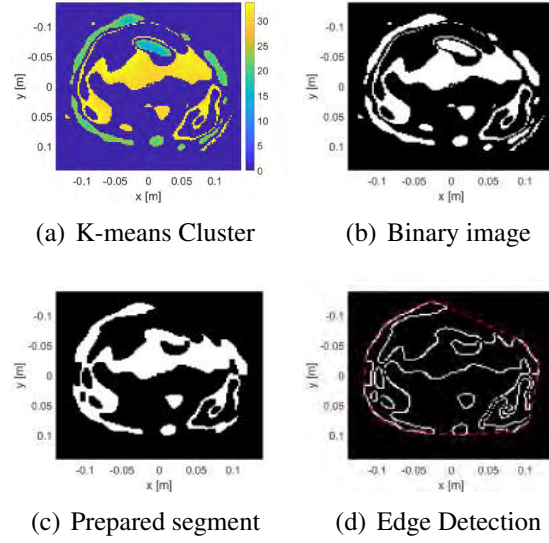


Figure 5.10: Extracting boundaries of the real part of relative permittivity *Low-Permittivity* cluster with Glycerin/Water solution for MRI model 1.

obtain the boundaries of both fat and muscle clusters. An edge detection algorithm implemented within the MATLAB's image processing toolbox was used [55]; in this algorithm the Canny edge detection algorithm was selected [56]. The discussion of the edge detection algorithm is beyond the scope of the thesis as more details can be found here [55, 56].

Figures 5.10, 5.11, and 5.12 show the procedure of obtaining real part relative permittivity *Low-Permittivity* cluster boundaries from MRI model 1, 2, and 3, respectively, for the Glycerin/Water solution, whereas Figures 5.13, 5.14, and 5.15 show the procedure for the ultrasound gel. In last image in each figure a dashed red line is shown to represent the outer estimated boundary.

The outer boundary, shown as dashed red line, is obtained as  $x$  and  $y$  points representing fat layer boundaries. These boundaries are to be used further to reconstruct the OI model.

For the imaginary part of the relative permittivity clusters, both the *Low-Permittivity* and *High-Permittivity* clusters boundaries, representing fat and muscle segments, were detected using the same procedure. Figures 5.16 and 5.17 show the final segment and outer boundary obtained after edge detection for MRI models 1, 2, and 3 using Glycerin/Water solution and ultrasound gel, respectively.



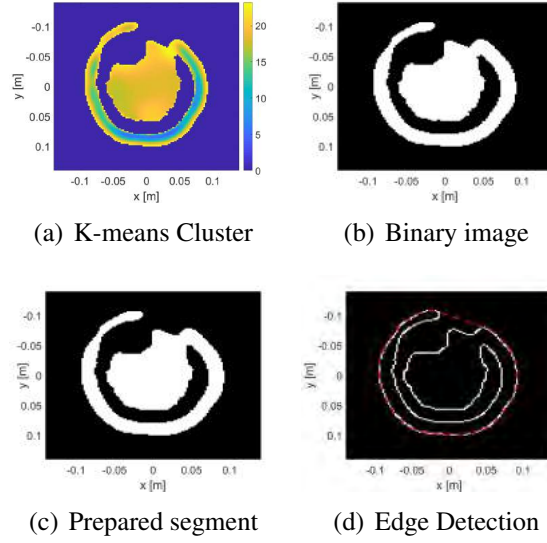


Figure 5.11: Extracting boundaries of the real part relative permittivity *Low-Permittivity* cluster with Glycerin/Water solution for MRI model 2.

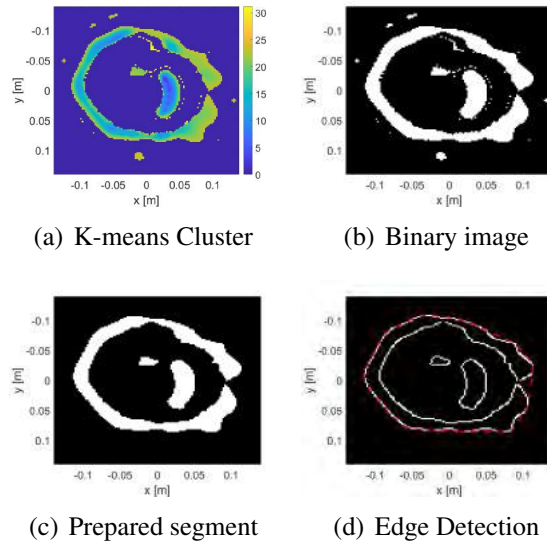


Figure 5.12: Extracting boundaries of the real part relative permittivity *Low-Permittivity* cluster with Glycerin/Water solution for MRI model 3.

Fig. 5.18 shows the boundaries of the the forward problem MRI models and the estimated models using both Glycerin/Water solution and ultrasound gel using the real-part clustering. In addition, the location of the imaging domain and antennas' locations are found using the outermost layer as previously done in Chapter 4.

Fig. 5.19 shows the boundaries of the forward problem MRI models and the estimated models using both Glycerin/Water solution and ultrasound gel using the imaginary-

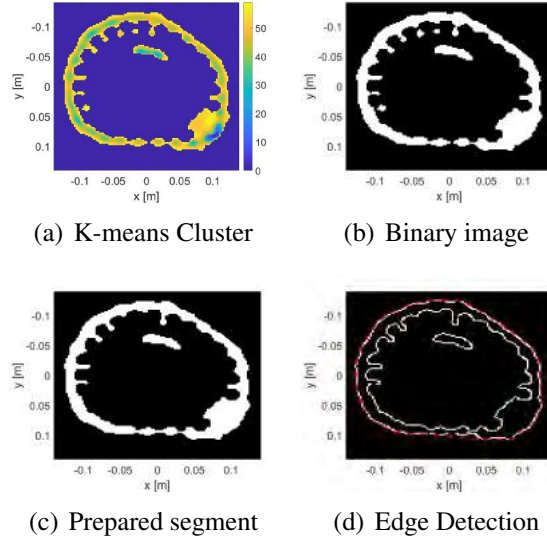


Figure 5.13: Extracting the boundaries of the real part relative permittivity *Low-Permittivity* cluster with ultrasound gel for MRI model 1.

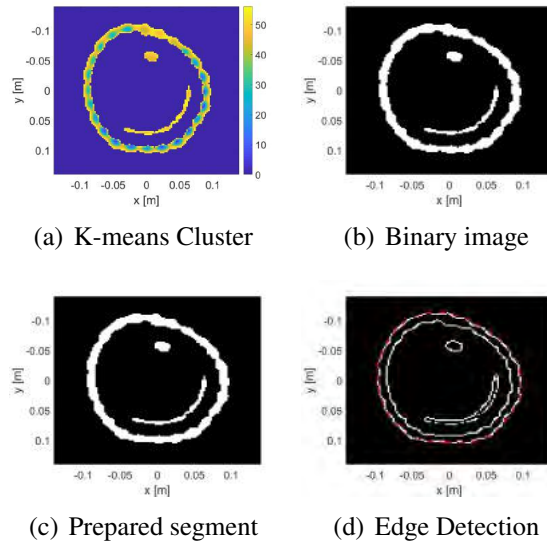


Figure 5.14: Extracting boundaries of the real part relative permittivity *Low-Permittivity* cluster with ultrasound gel for MRI model 2.

part clusters. In addition, the locations of the new imaging domain and antennas' locations are labeled.

## 5.6. Inversion Results

After building the estimated models using both real and imaginary parts of relative permittivity reconstructions, they are used as prior information related to the struc-

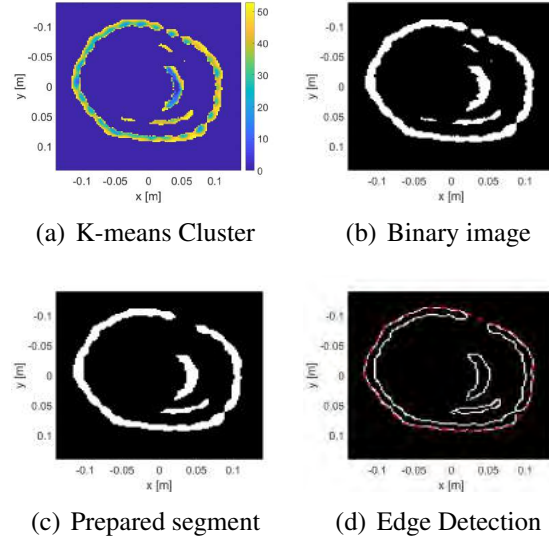
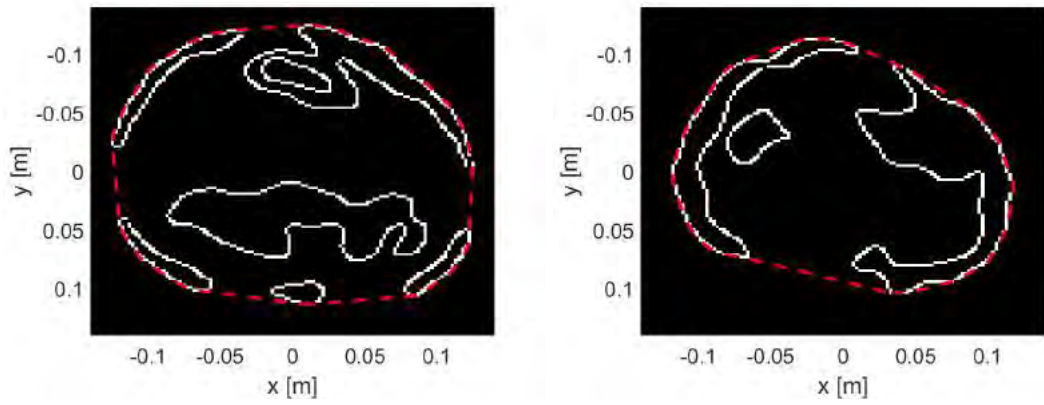


Figure 5.15: Extracting boundaries of the real part relative permittivity *Low-Permittivity* cluster with ultrasound gel for MRI model 3.

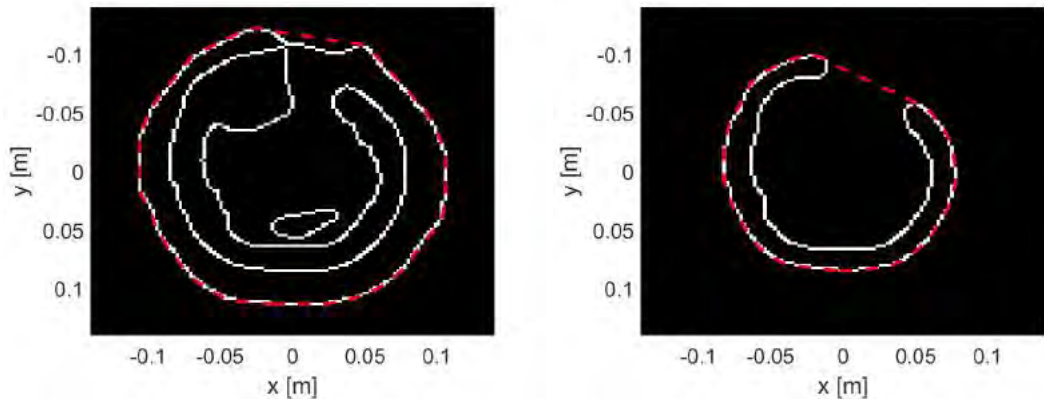
ture of the OI. For the estimated models obtained using the real-part clustering, two of the inhomogeneous background scenarios discussed in Section 4.1, are followed to incorporate prior information about the dielectric properties of layers. These scenarios are the mid-value layer and the skin-fat layer. For the imaginary-part clustering, these two prior information scenarios as well as the third inhomogeneous background using skin-fat-muscle are considered. Furthermore, as shown in Chapter 4, the best outcomes came when the imaging domain and the location of antennas were closer to the OI; thus, they are directly applied within the inversion algorithm, which is using the estimated models as inhomogeneous background.

Figures 5.20 and 5.21 show the inversion results of the real-part based clustering model using Glycerin/Water solution in MRI images 1, 2, and 3 with mid-value and skin-fat scenarios, respectively. In addition, Figures 5.22 and 5.23 show the results using the ultrasound gel matching medium.

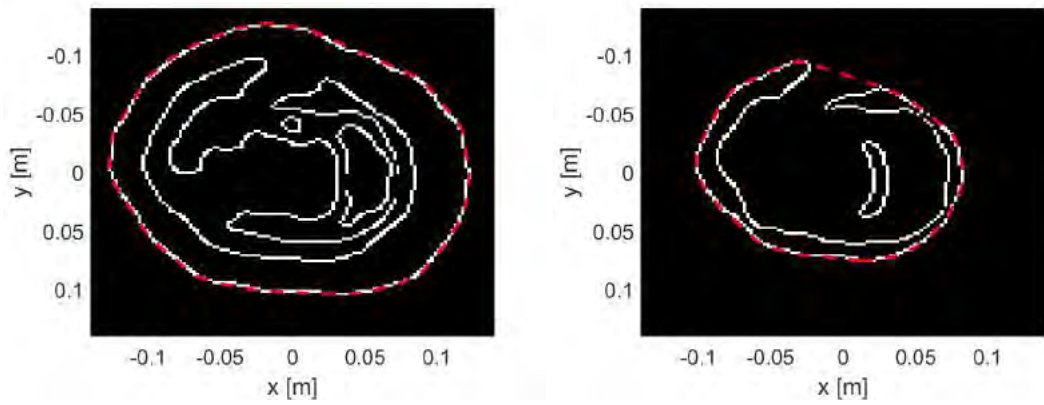
The results of the inversion using the imaginary-part based clustering model are shown in Fig. 5.24, 5.25, and 5.26 with mid-value, skin-fat, and skin-fat-muscle scenarios, respectively.



(a) MRI Image 1

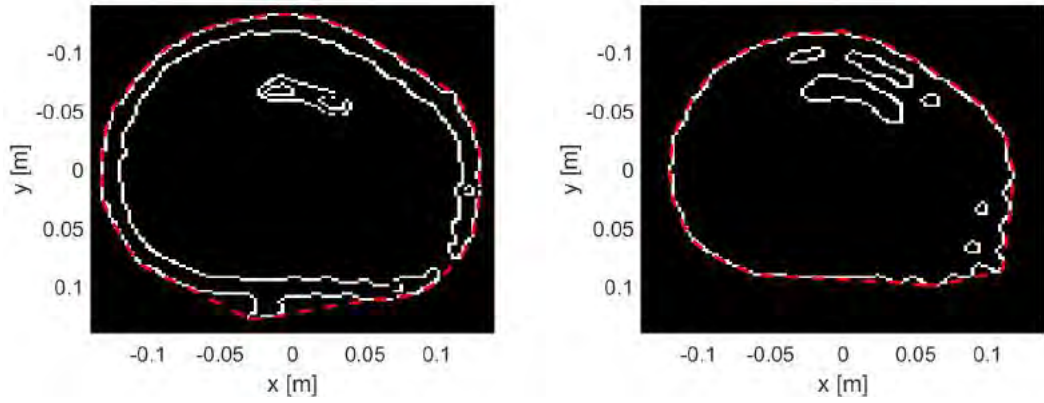


(b) MRI Image 2

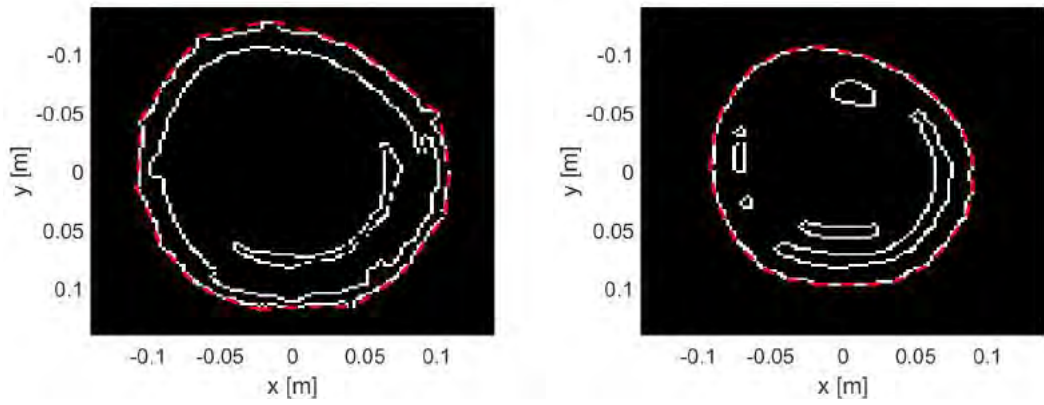


(c) MRI Image 3

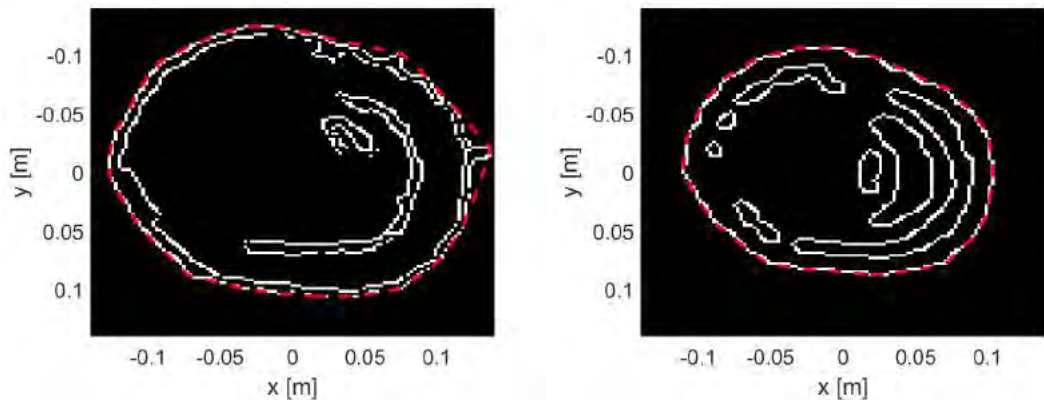
Figure 5.16: Extracting the boundaries of the imaginary part relative permittivity clusters with Glycerin/Water solution (Left = *Low-Permittivity*, Right = *High-Permittivity*).



(a) MRI Image 1



(b) MRI Image 2



(c) MRI Image 3

Figure 5.17: Extracting the boundaries of the imaginary part relative permittivity clusters with ultrasound gel (Left = *Low-Permittivity*, Right = *High-Permittivity*).



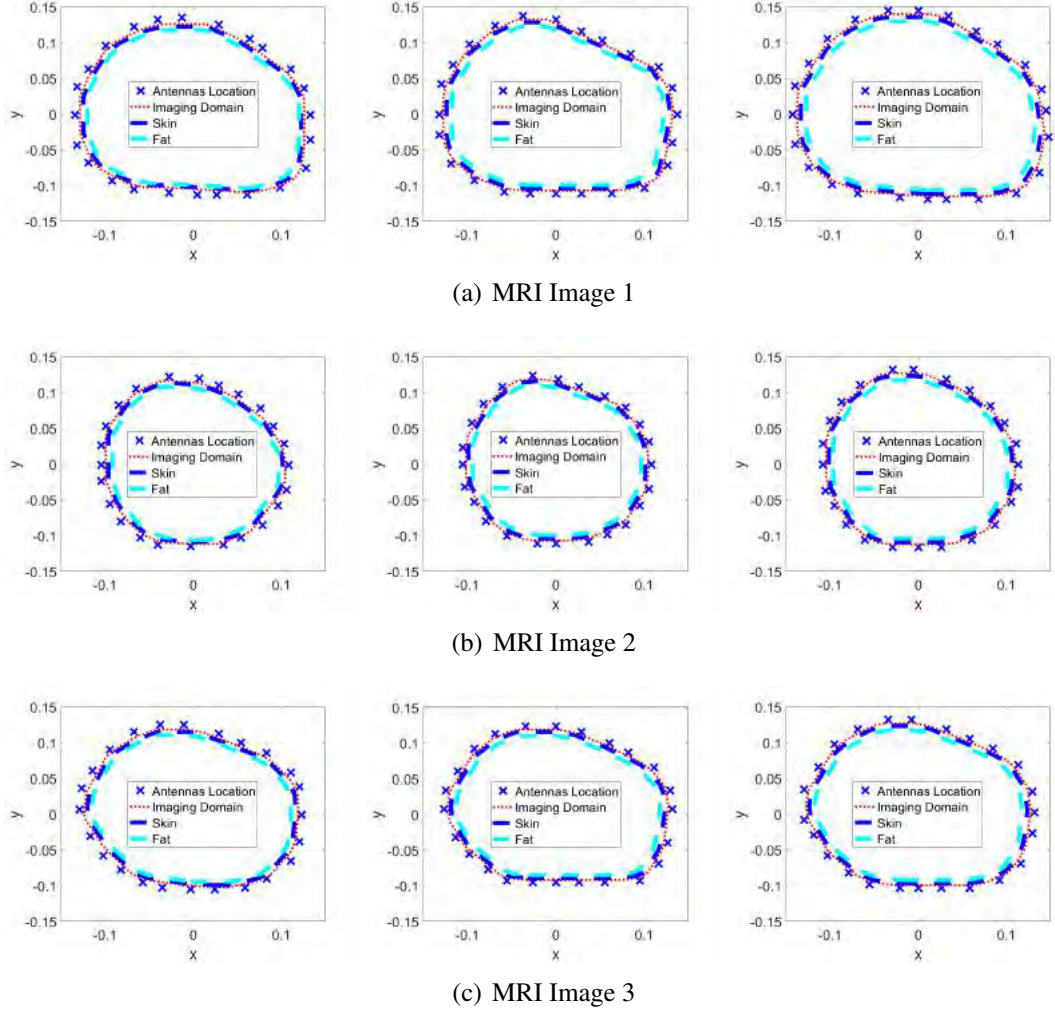


Figure 5.18: The boundary of the estimated model created using real part relative permittivity clusters along with new imaging domain and antennas location (Left = Forward problem MRI models, Middle = Glycerin/Water solution models, Right = Ultra-sound gel models).

## 5.7. Analysis and Observations

The inversion results using the real part relative permittivity models results in good reconstruction of both bones. For the mid-value inhomogeneous background scenario, the location of the two bones was detected in both Glycerin/Water solution and ultrasound gel inverted images. However, MRI model 3 did not provide efficient reconstructions in term of bone location and dielectric properties. This was overcome using the skin-fat scenario where tibia bone became detectable, as well as its dielectric properties values.

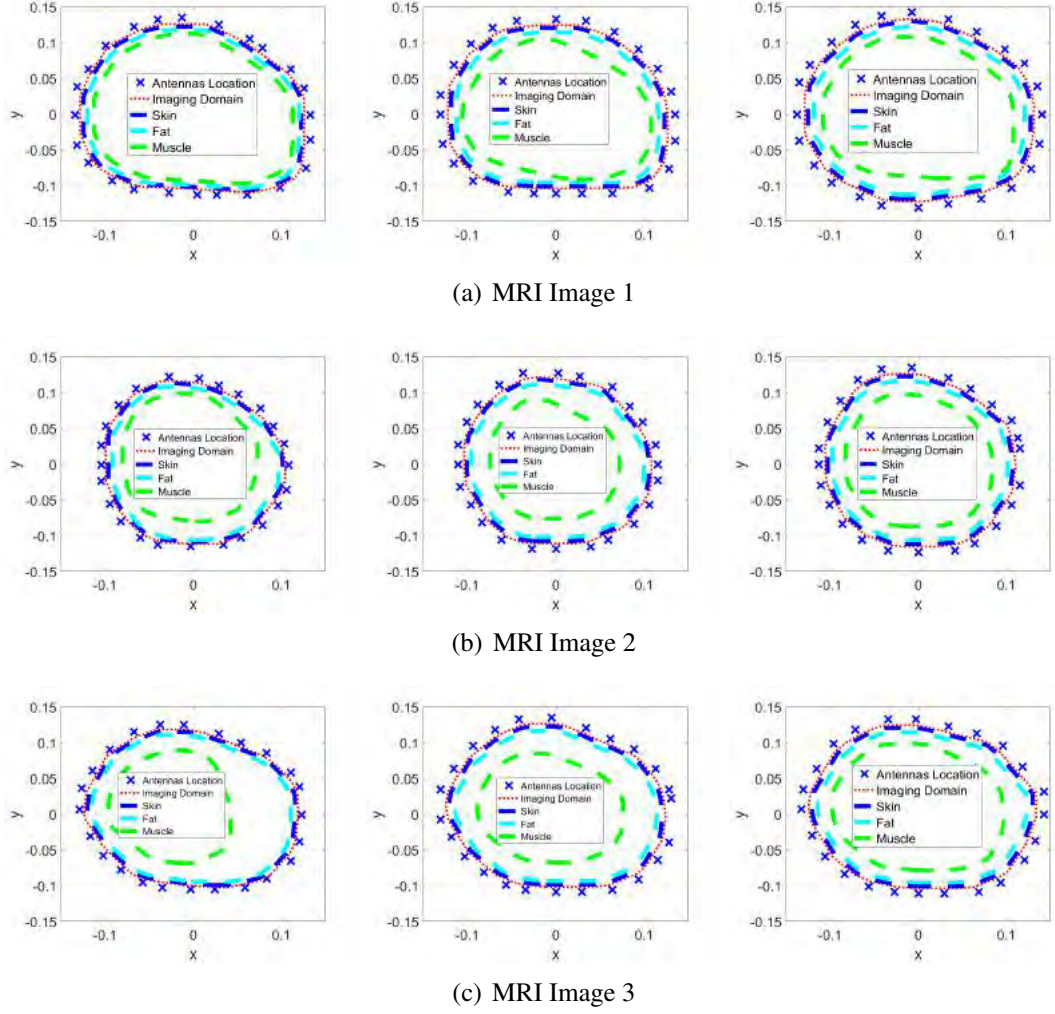
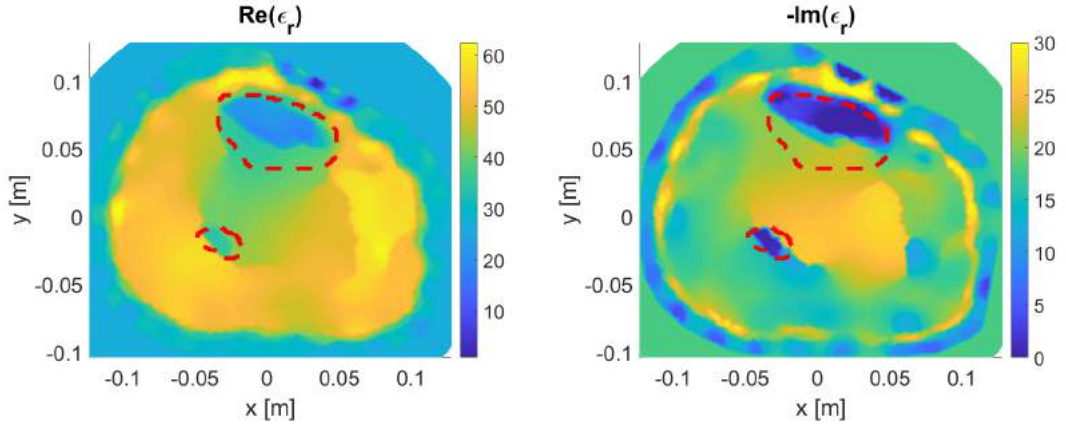


Figure 5.19: The boundary of the estimated model created using imaginary part relative permittivity clusters along with new imaging domain and antennas location (Left = Forward problem MRI models, Middle = Glycerin/Water solution models, Right = Ultrasound gel models).

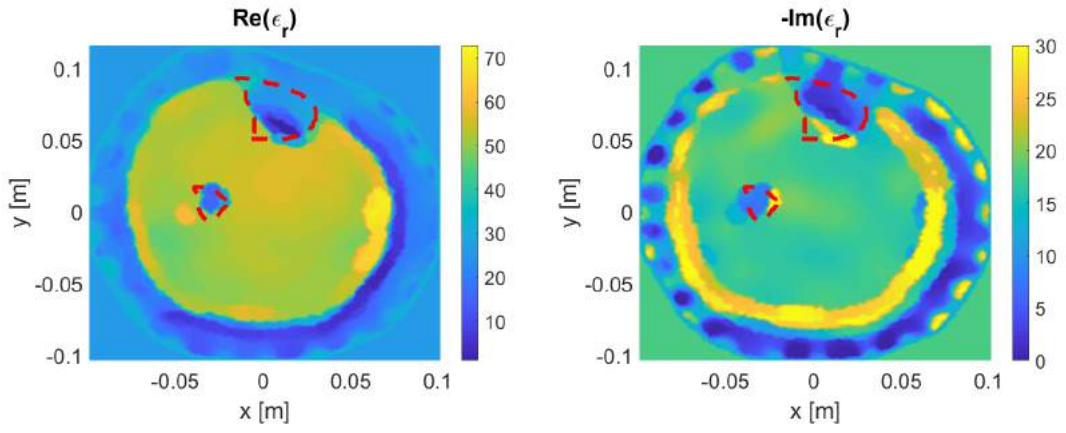
Using the imaginary-part relative permittivity clustering models resulted in obtaining almost the same outcomes as the previous real-part clustering models inversion. However, it can be seen that the imaginary-part overestimates regions, therefore, scenarios were less accurate compared to the real-part results. This is clearly seen in the skin-fat-muscle scenario, as the results were very poor due to the over estimation of muscle regions.

From this chapter the following points can be concluded,

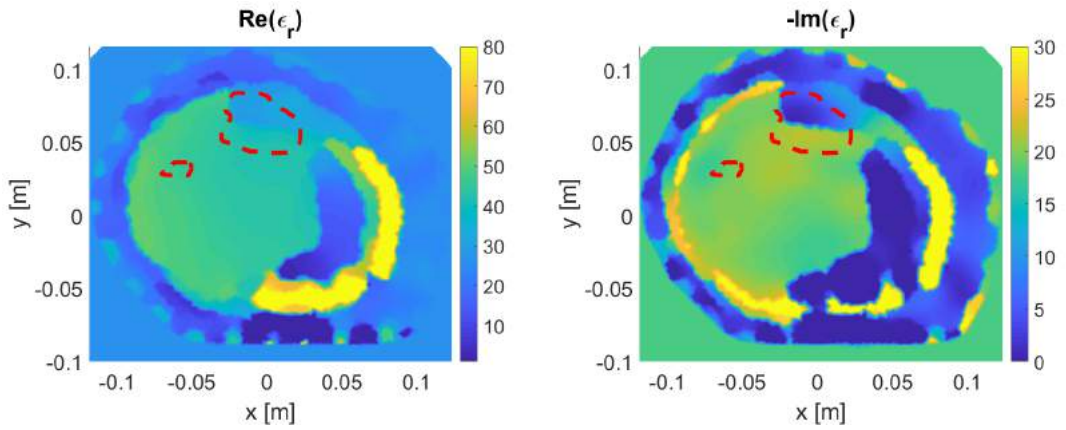
- Image processing techniques could be useful to obtain structural information about the OI being imaged.



(a) MRI Image 1



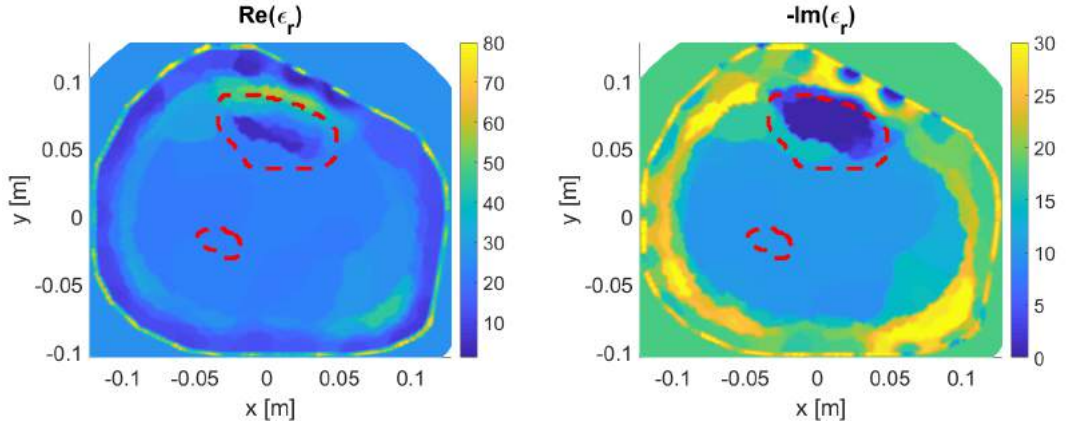
(b) MRI Image 2



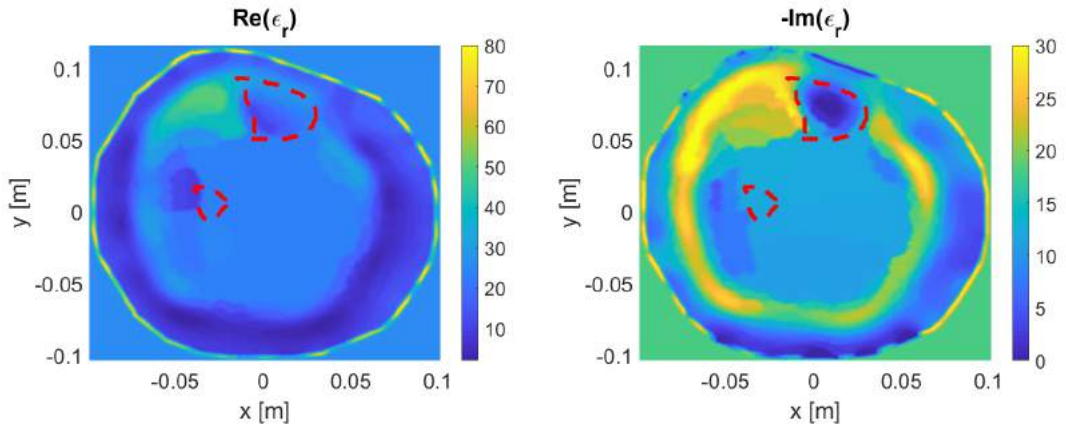
(c) MRI Image 3

Figure 5.20: Inversion results for the real-part based clustering model using the Glycerin/Water solution with mid-value inhomogeneous scenario.

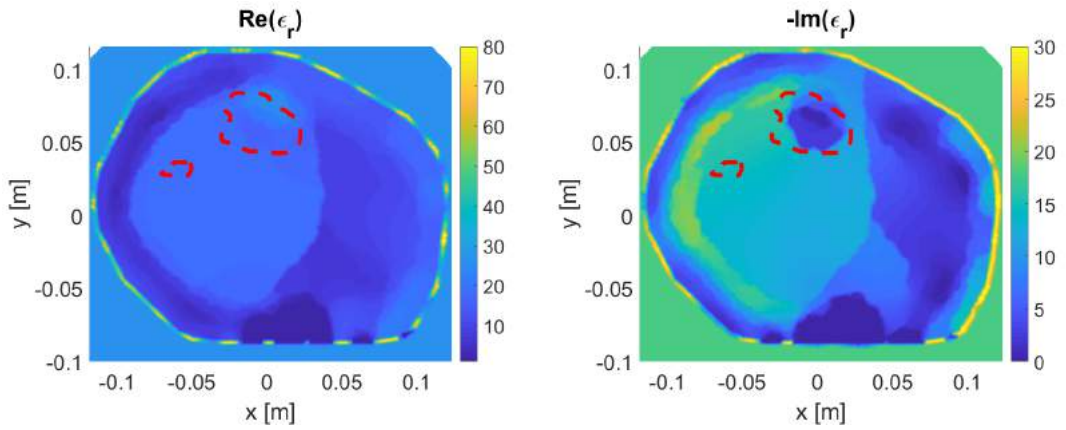




(a) MRI Image 1

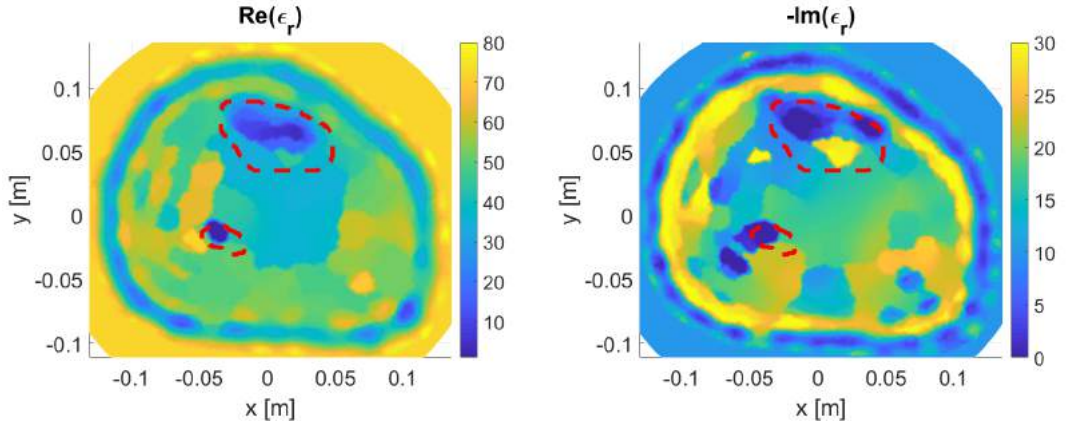


(b) MRI Image 2

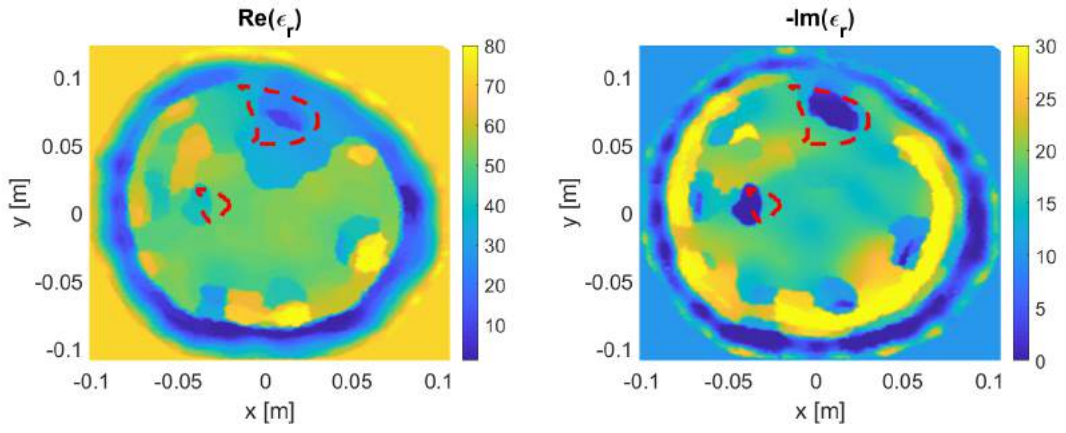


(c) MRI Image 3

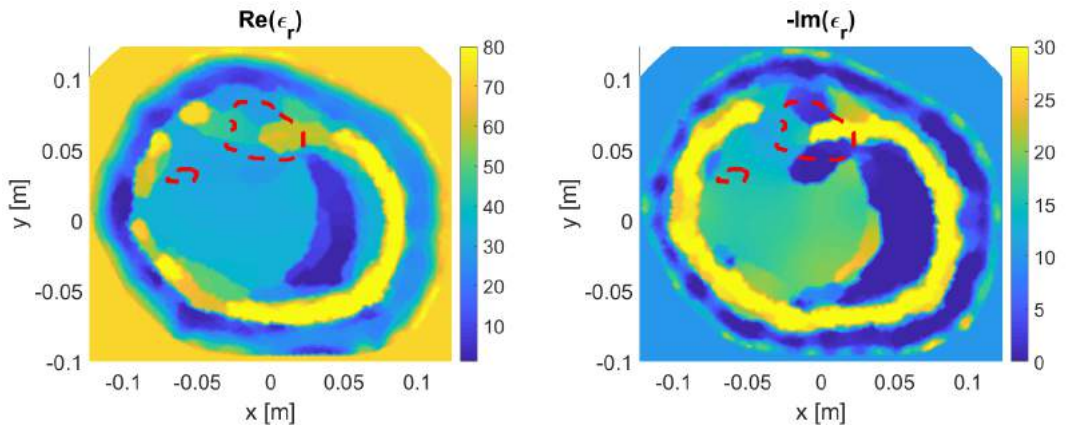
Figure 5.21: Inversion results for the real-part based clustering model using the Glycerin/Water solution with skin-fat inhomogeneous scenario.



(a) MRI Image 1

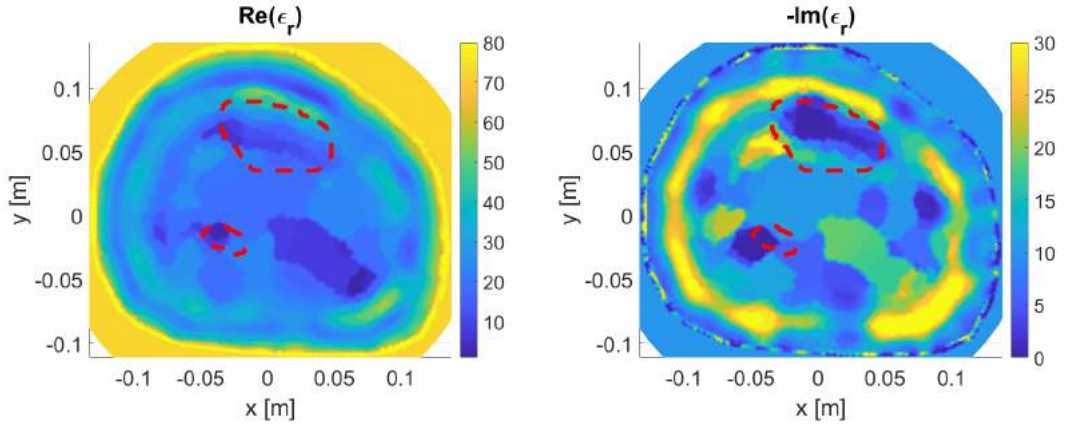


(b) MRI Image 2

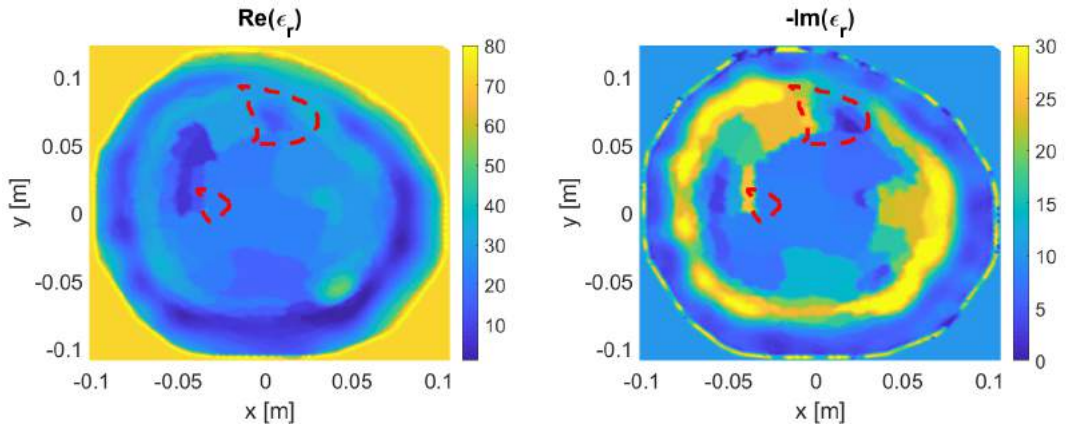


(c) MRI Image 3

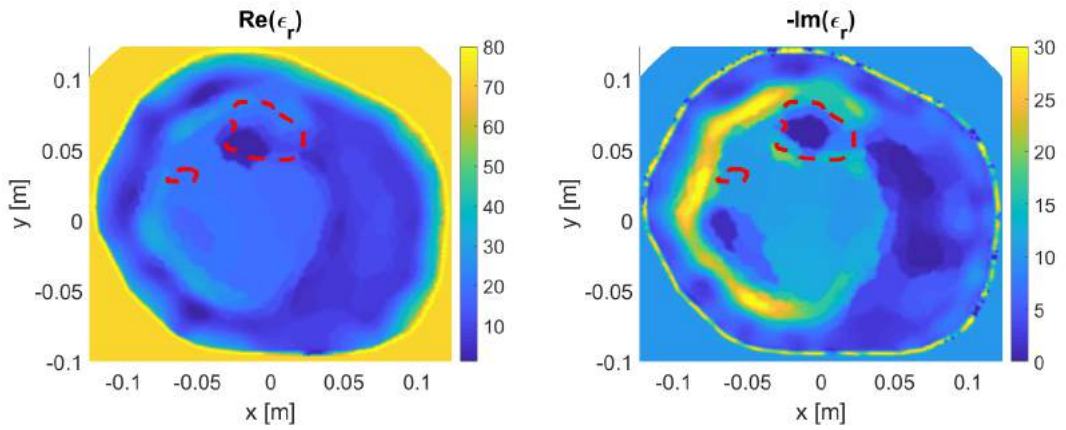
Figure 5.22: Inversion results for the real-part based clustering model using the ultrasound gel with mid-value inhomogeneous scenario.



(a) MRI Image 1



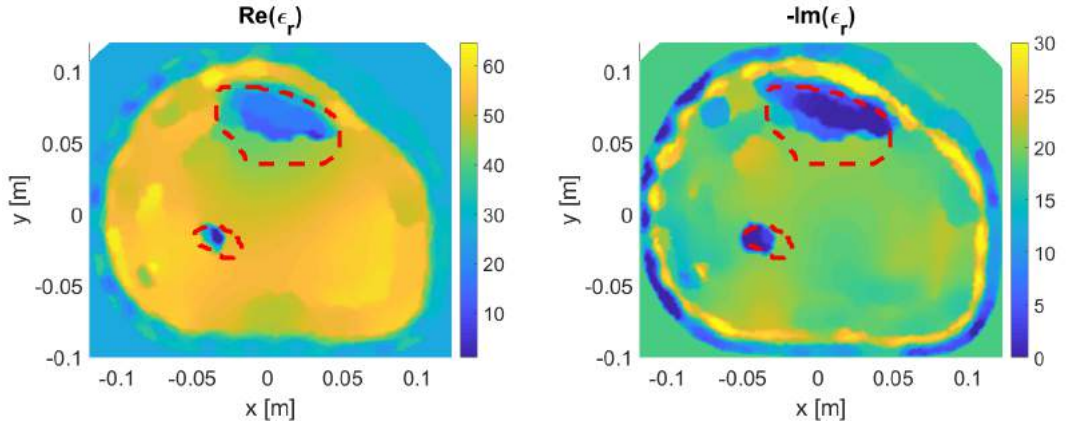
(b) MRI Image 2



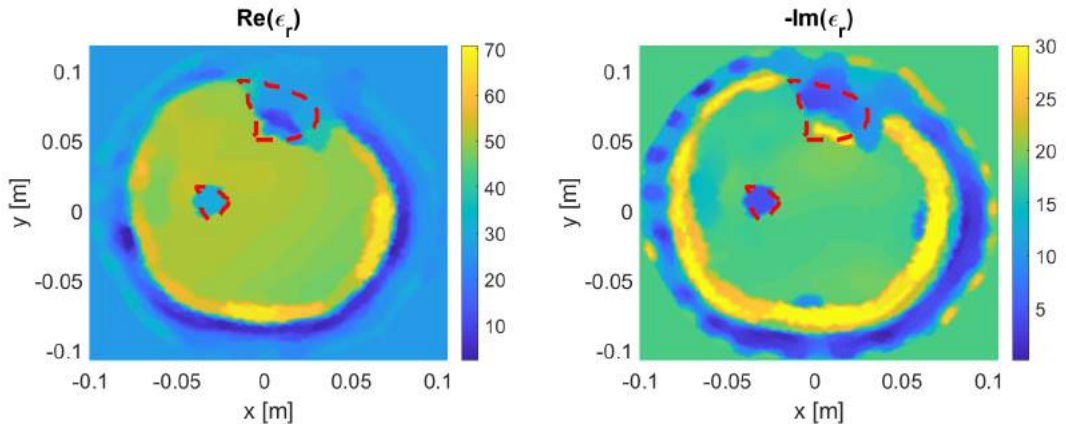
(c) MRI Image 3

Figure 5.23: Inversion results for the real-part based clustering model using the ultrasound gel with skin-fat inhomogeneous scenario.

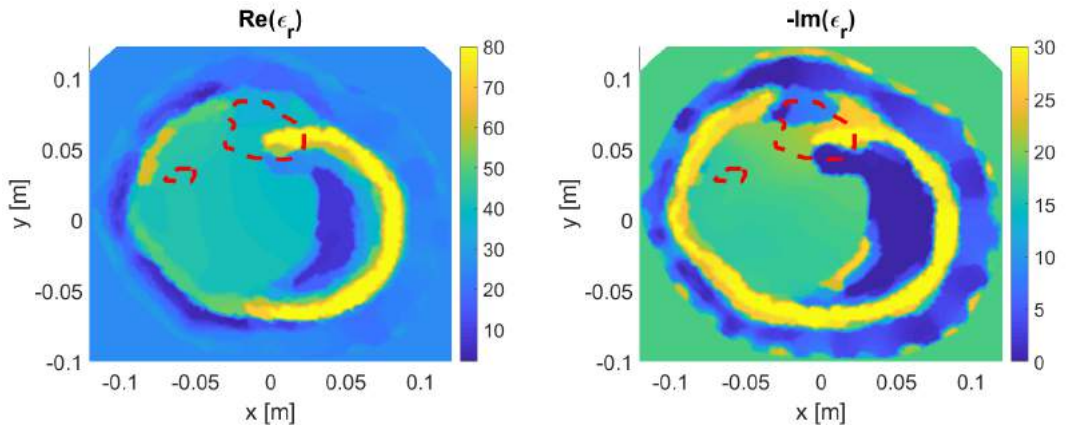




(a) MRI Image 1

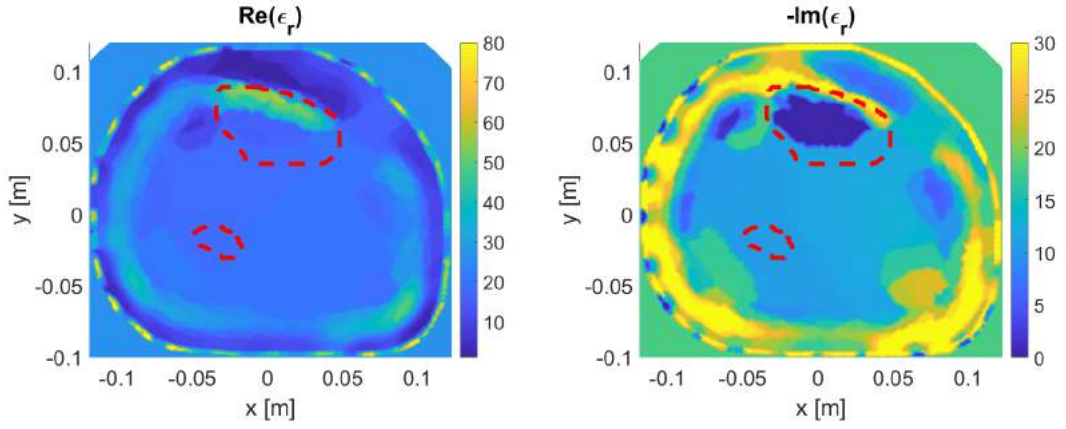


(b) MRI Image 2

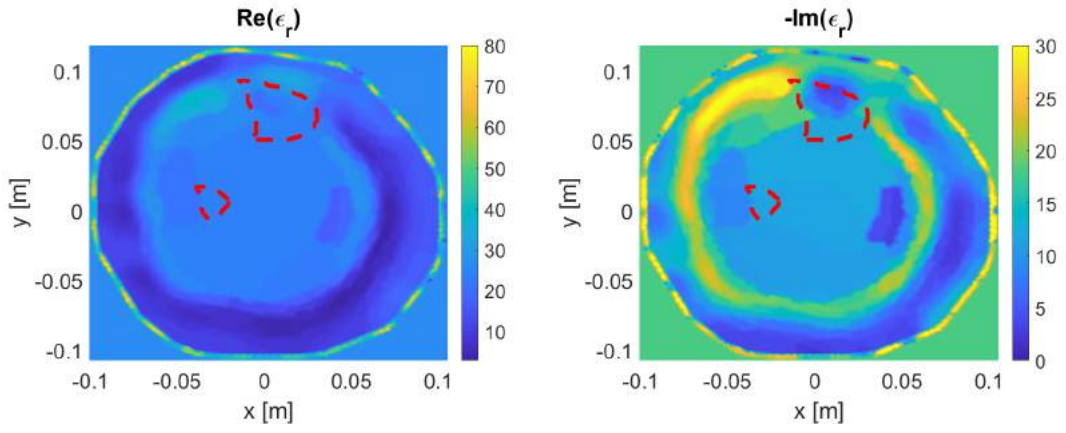


(c) MRI Image 3

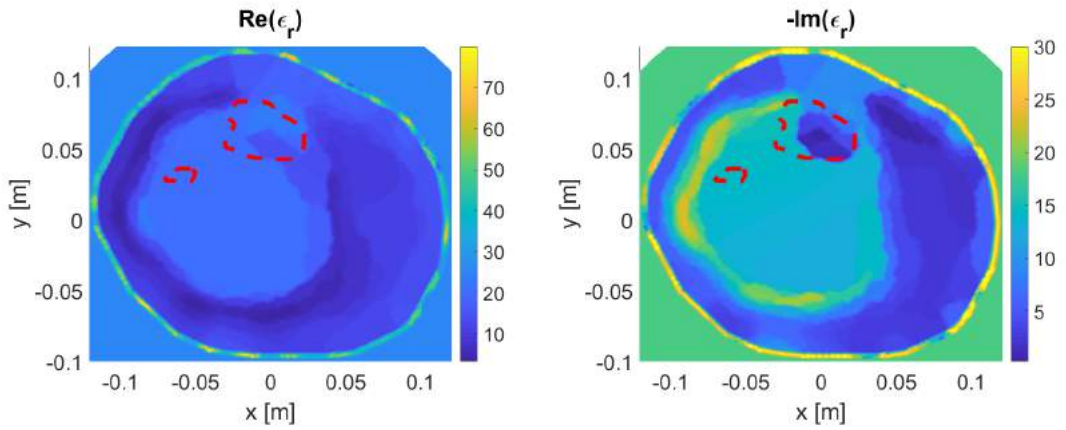
Figure 5.24: Inversion results for the imaginary-part based clustering model using the Glycerin/Water solution with mid-value inhomogeneous scenario.



(a) MRI Image 1

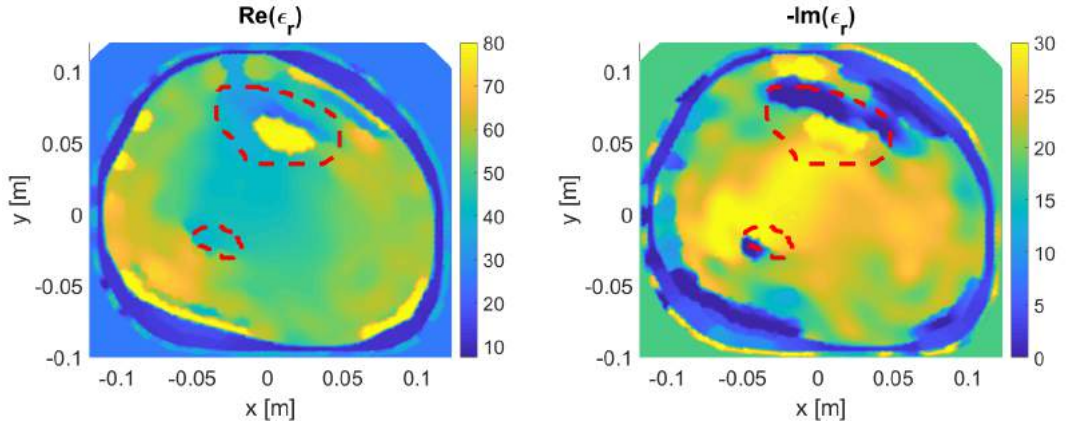


(b) MRI Image 2

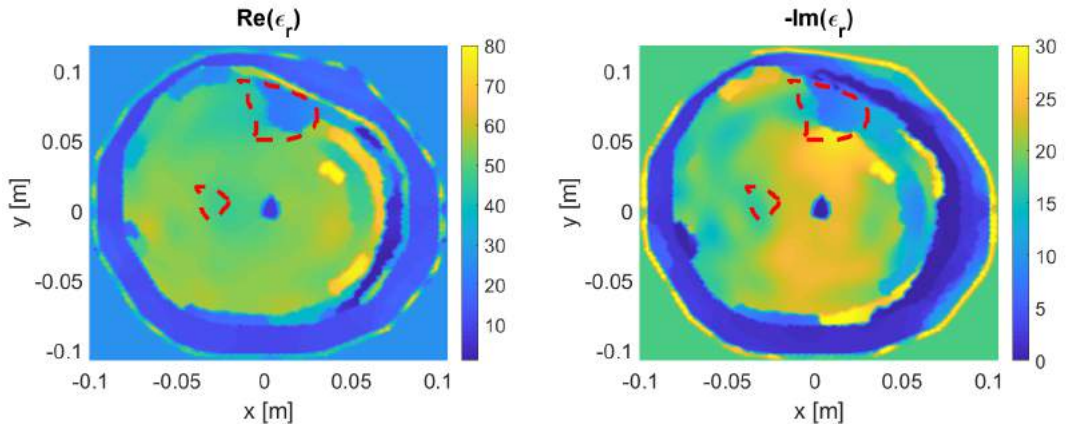


(c) MRI Image 3

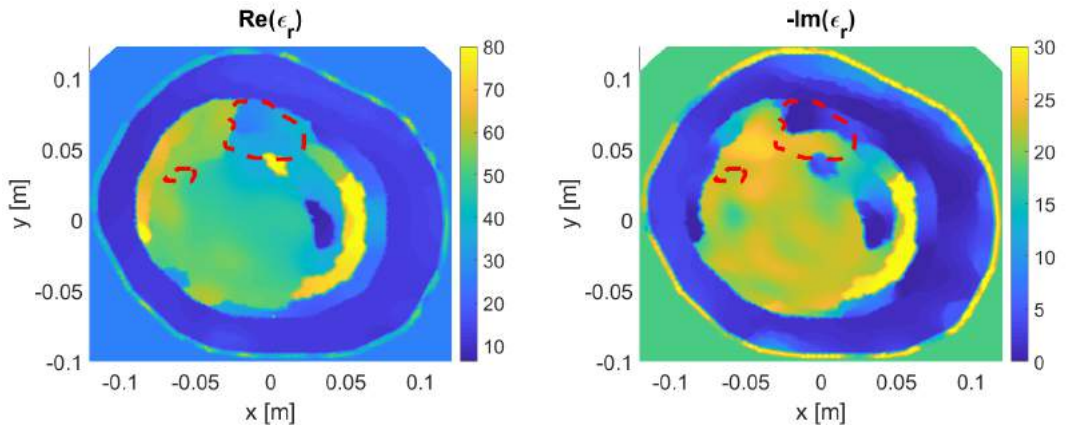
Figure 5.25: Inversion results for the imaginary-part based clustering model using the Glycerin/Water solution with skin-fat inhomogeneous scenario.



(a) MRI Image 1



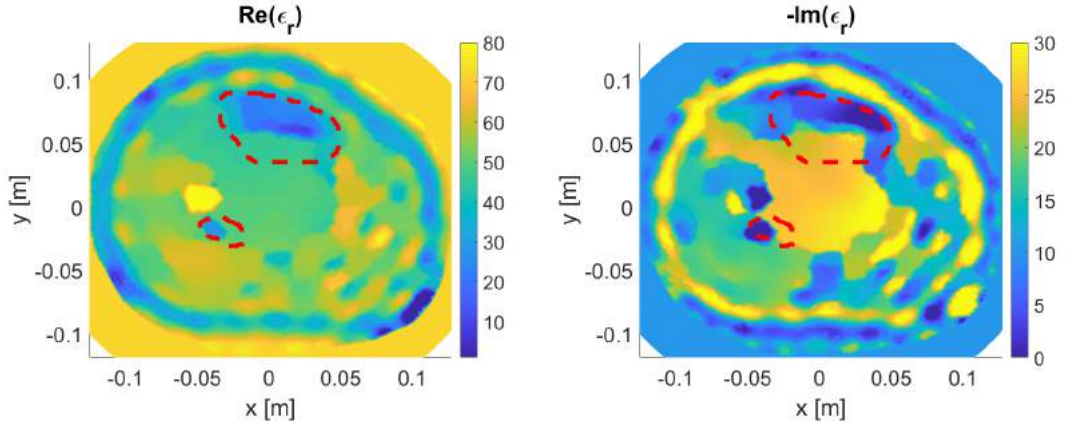
(b) MRI Image 2



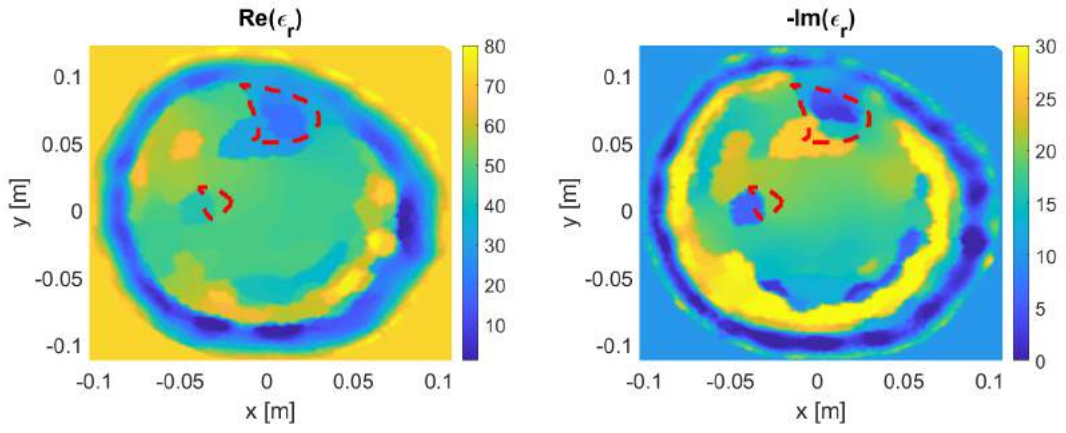
(c) MRI Image 3

Figure 5.26: Inversion results for the imaginary-part clustering model using the Glycerin/Water solution with skin-fat-muscle inhomogeneous scenario.

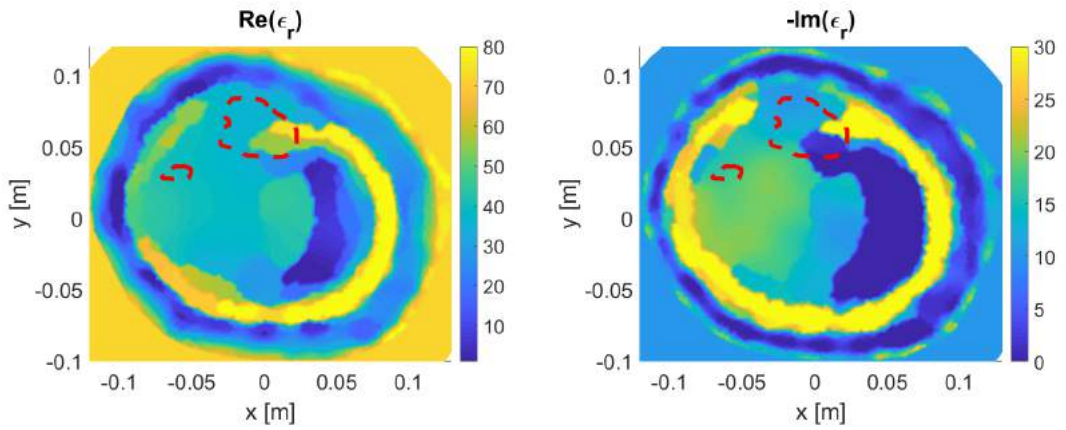




(a) MRI Image 1

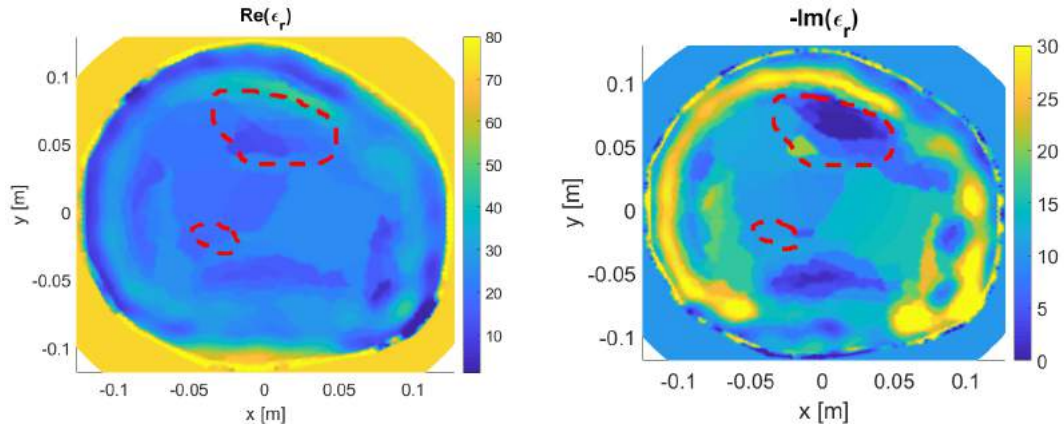


(b) MRI Image 2

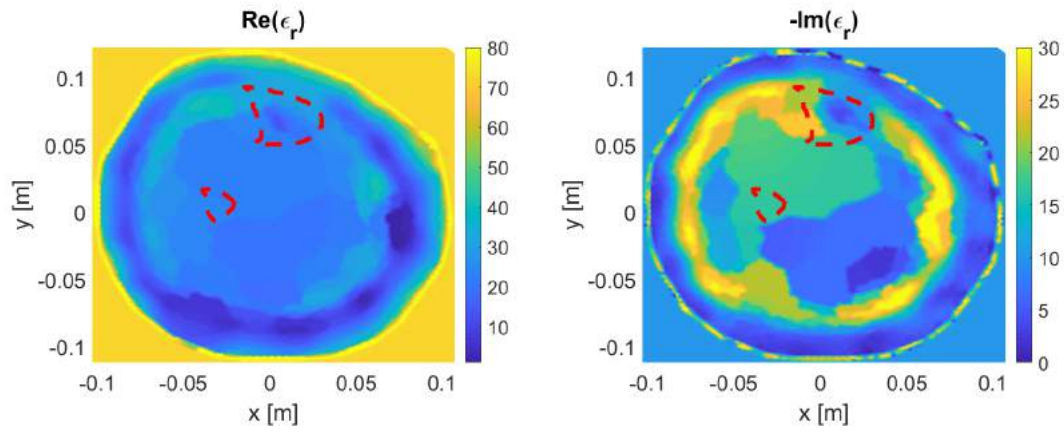


(c) MRI Image 3

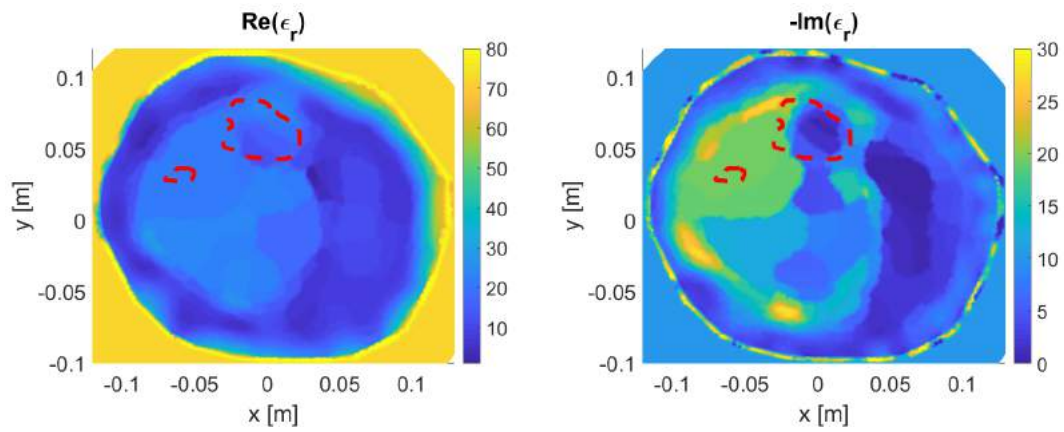
Figure 5.27: Inversion results for the imaginary-part clustering model using the ultrasound gel with mid-value inhomogeneous scenario.



(a) MRI Image 1



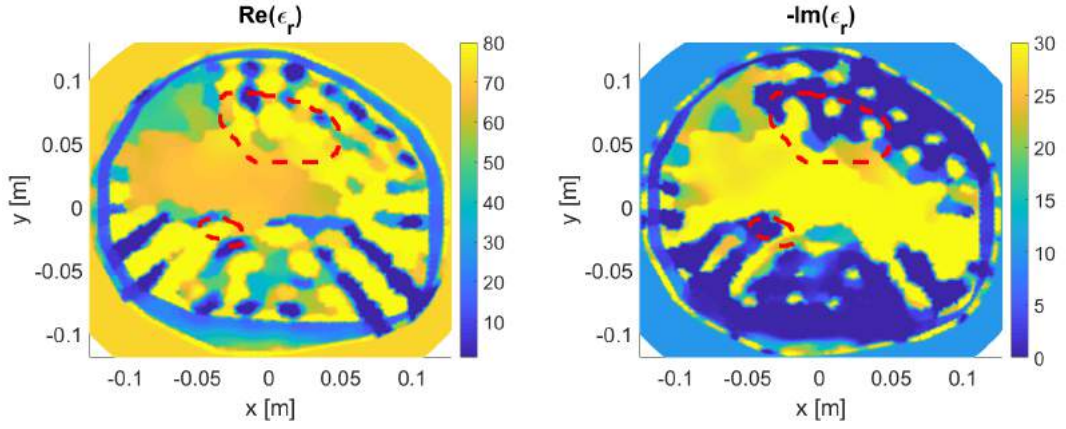
(b) MRI Image 2



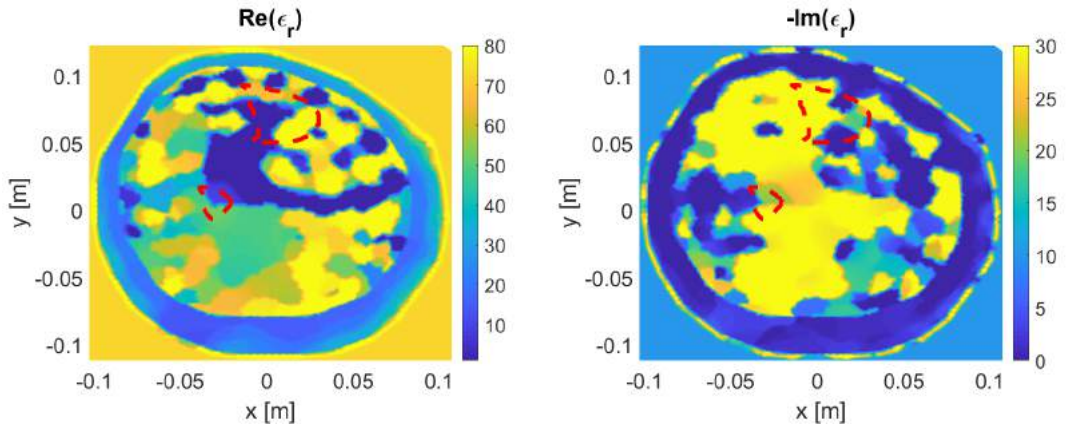
(c) MRI Image 3

Figure 5.28: Inversion results for the imaginary-part clustering model using the ultrasound gel with skin-fat inhomogeneous scenario.

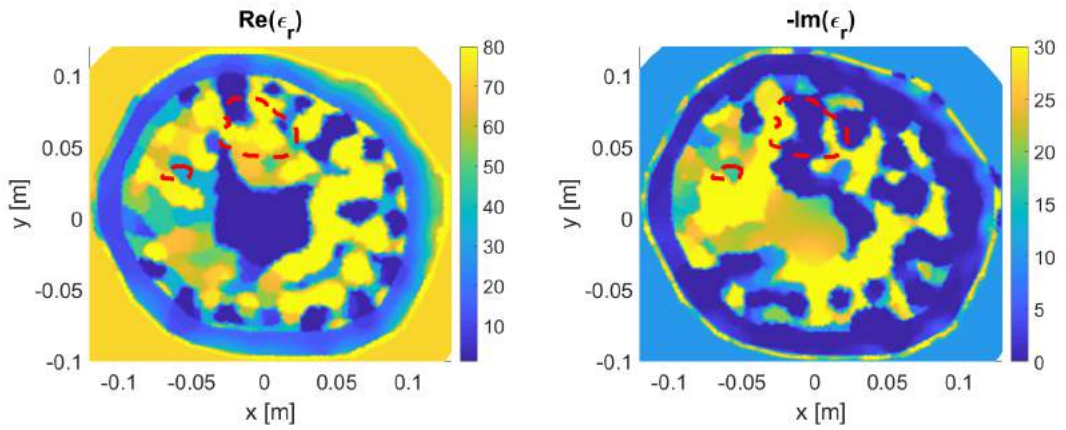




(a) MRI Image 1



(b) MRI Image 2



(c) MRI Image 3

Figure 5.29: Inversion results for the imaginary-part based clustering model using the ultrasound gel with skin-fat-muscle inhomogeneous scenario.

- Both real and imaginary parts of the reconstructed relative permittivity can be used to build an estimated structural model of the OI, however, it is recommended to use the real-part model due to proper estimations.
- The results of the inversion algorithm suggest that using mid-value inhomogeneous scenario could be useful for skin to mid fat leg models, while skin-fat is recommended for thick fat scenarios.
- The use of skin-fat-muscle requires accurate localization of boundary points related to each layer, as any over-estimations could result in poor reconstructed images.

Considering these points, and as the process of imaging human bones has been enhanced, the evaluation of bone health is required. However, it is considered a challenge to build the estimated model, as for each BVF scenario, the reconstructed images are going to differ. This is going to be investigated in the next chapter.

## Chapter 6: Analysis on Bone Health Monitoring

In this chapter, the effect of varying bone density is investigated. Five BVF scenarios are taken into consideration to represent various bone health conditions. For the five BVF variations, the blind inversion is applied for each scenario. Each blind inversion is used to build the corresponding estimated models of the OI using the clustering technique described in Chapter 5. Then, statistical analysis on the results is applied to explore the feasibility of using MWT in bone health monitoring.

### 6.1. Bone Density Variations

As previously shown in Chapter 3, variations in the bone volume fraction (BVF) will cause changes to the overall dielectric properties of bones; a decrease in the density of bones results in an increase in the dielectric properties. Therefore, MWT can be used to detect such differences. In addition to the three BVF cases chosen in Section 3.3, two additional scenarios are added to improve the quality of the analysis. Based on values shown [1], the five bone BVF scenarios and their corresponding relative complex permittivity values are,

- Healthy Bone:  $\epsilon_r = 13 - j3.0$ ,
- Bone with 0.45 BVF:  $\epsilon_r = 14 - j3.05$ ,
- Bone with 0.35 BVF:  $\epsilon_r = 16 - j3.1$ ,
- Bone with 0.25 BVF:  $\epsilon_r = 18 - j3.2$ ,
- Bone with 0.1 BVF:  $\epsilon_r = 23 - j3.4$ .

A bone with 0.5 BVF is selected as an example of a healthy bone case. In addition, a bone with 0.1 BVF is a scenario with a severe bone density loss. In the case of Vitamin D deficiency, the actual bone condition is unknown. Therefore, each bone scenario goes initially through the blind inversion process described in Chapter 3. Figures 6.1 and 6.2 show, respectively, the relative complex permittivity blind inversion reconstructions using the 80:20 Glycerin/Water solution and the ultrasound gel mediums for the five BVF scenarios from MRI model 1. Figures 6.3 and 6.4 show the results from MRI model 2. Figures 6.5 and 6.6 show the results from MRI model 3.

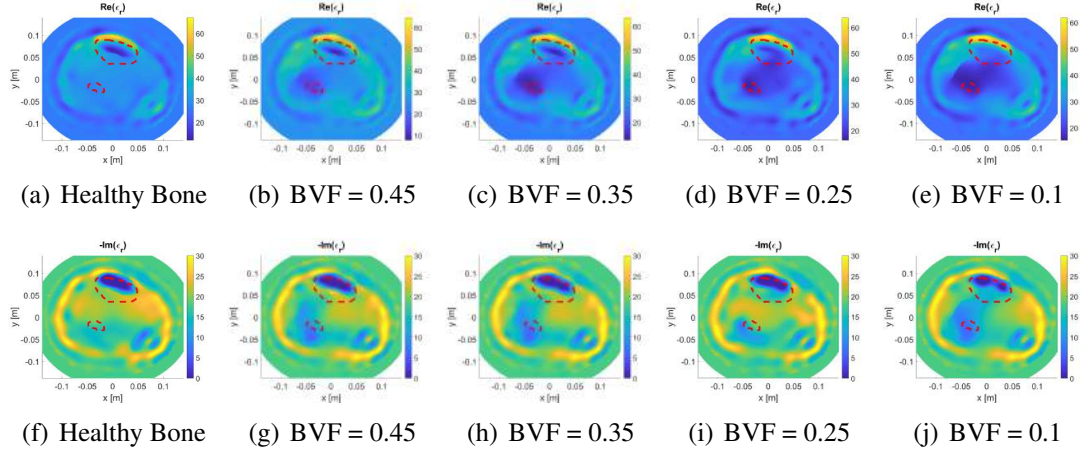


Figure 6.1: MRI model 1: The real and imaginary components of the relative permittivity reconstructions using Glycerin/Water solution.

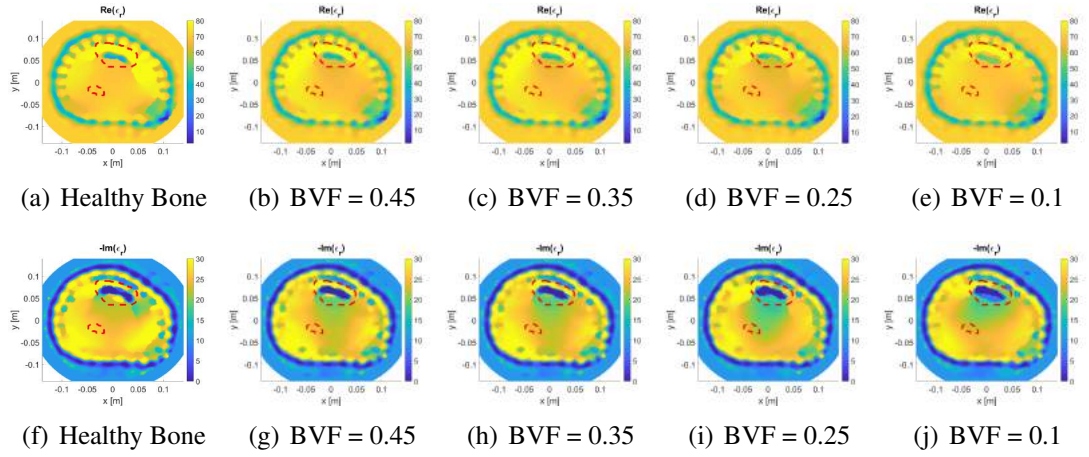


Figure 6.2: MRI model 1: The real and imaginary components of the relative permittivity reconstructions using ultrasound gel.

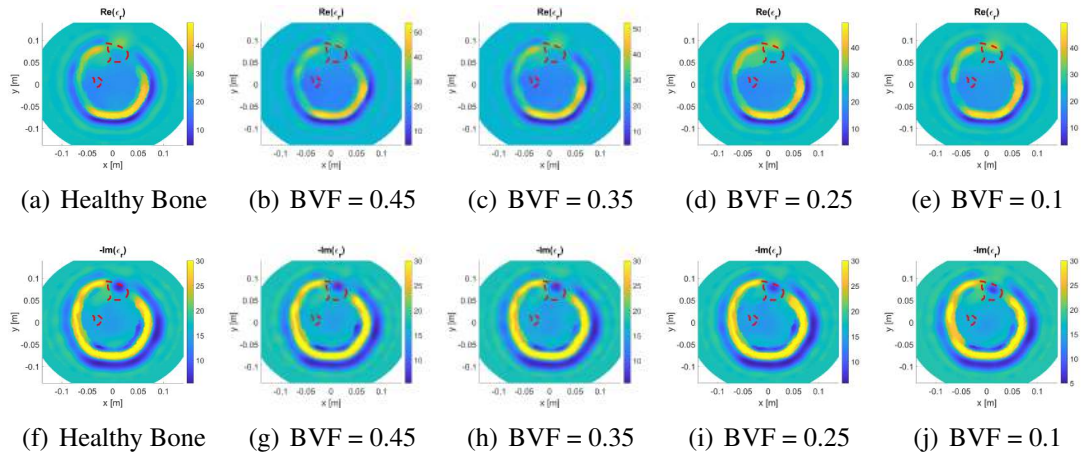


Figure 6.3: MRI model 2: The real and imaginary components of the relative permittivity reconstructions using Glycerin/Water solution.



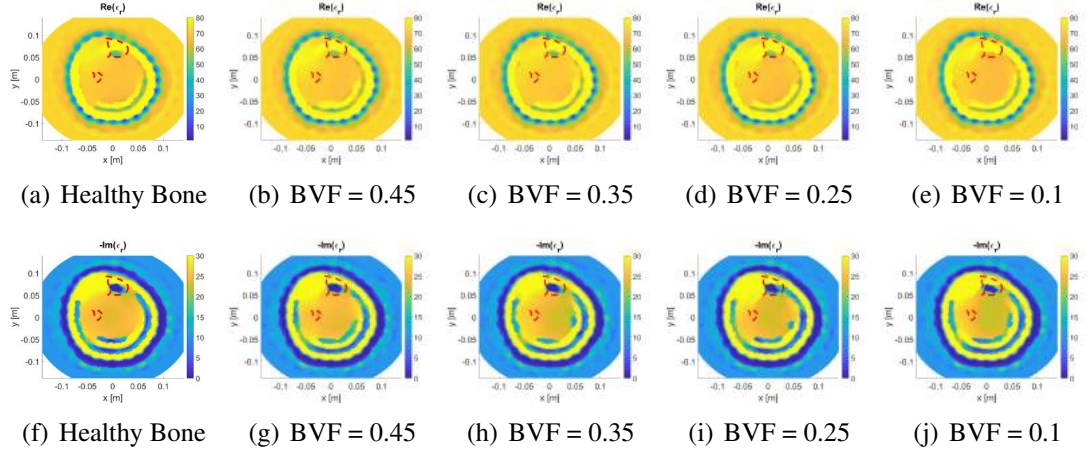


Figure 6.4: MRI model 2: The real and imaginary components of the relative permittivity reconstructions using ultrasound gel.

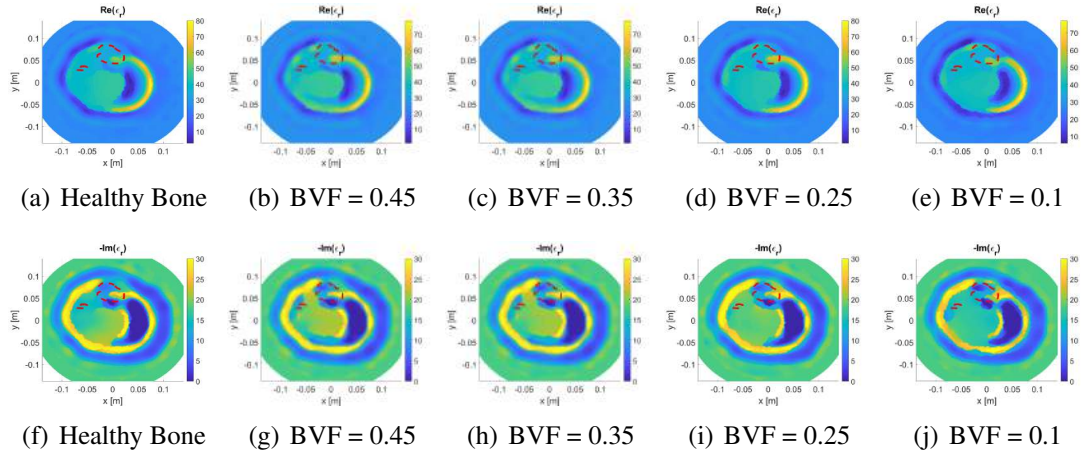


Figure 6.5: MRI model 3: The real and imaginary components of the relative permittivity reconstructions using Glycerin/Water solution.

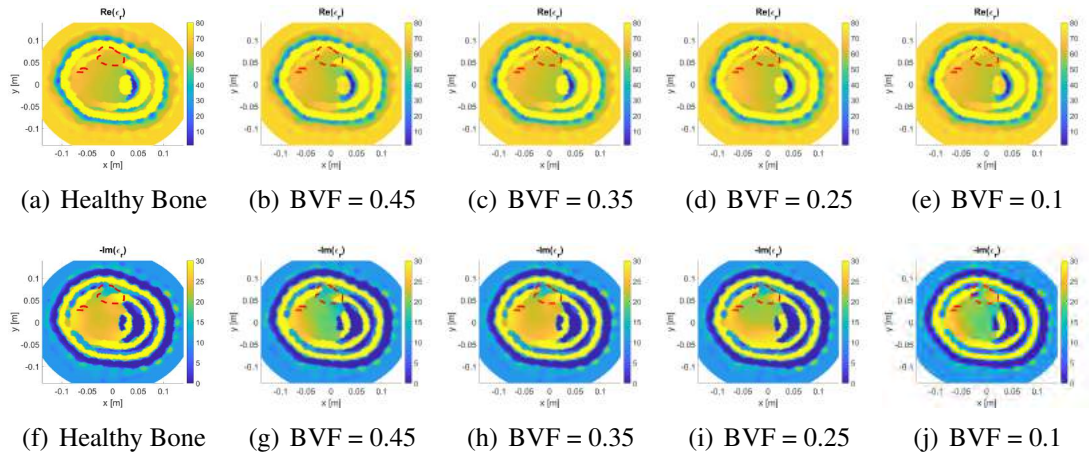


Figure 6.6: MRI model 3: The real and imaginary components of the relative permittivity reconstructions using ultrasound gel.

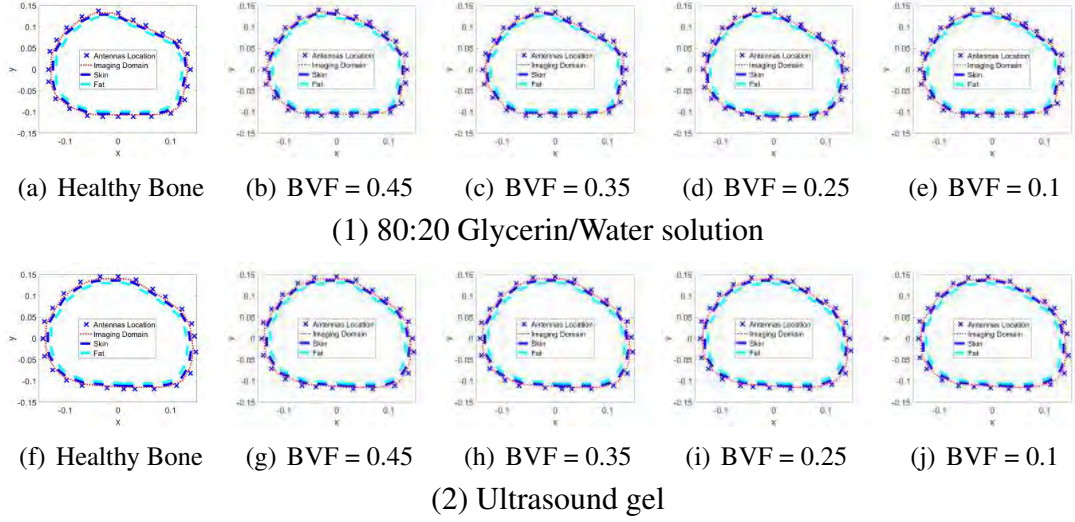


Figure 6.7: MRI model 1: The real-part based clustering estimated models.

## 6.2. Building the Estimated Models

The next step after performing the blind inversions is to use the reconstruction results to extract structural information about the leg. An estimated model for each scenario is built from the blind inversion images following the procedure detailed in Chapter 5. This is done for each BVF case separately to investigate the possibility of building the estimated models for unknown health conditions. Each estimated model is considered as the OI boundaries for the use within the inhomogeneous background inversion scenarios. Figures 6.7, 6.8, and 6.9 show the results of building MRI model 1, 2, and 3 estimated models, respectively, based on using the real part of relative permittivity reconstructions. The figures show the results of using two matching media: Glycerin/Water solution and Ultrasound gel.

The imaginary-part based clusters were also used for each scenario to reconstruct the estimated models. Figures 6.10, 6.11, and 6.12 show the results of building MRI models 1, 2, and 3 estimated models, respectively, using the imaginary-part based clustering for Glycerin/Water solution and ultrasound gel.

## 6.3. Enhanced Inversion Results

As previously recommended in Chapter 5, the real-part based clustering estimated models are preferred to be used as they do not overestimate regions of the OI. Therefore, each MRI estimated model using the real-part based clustering is used

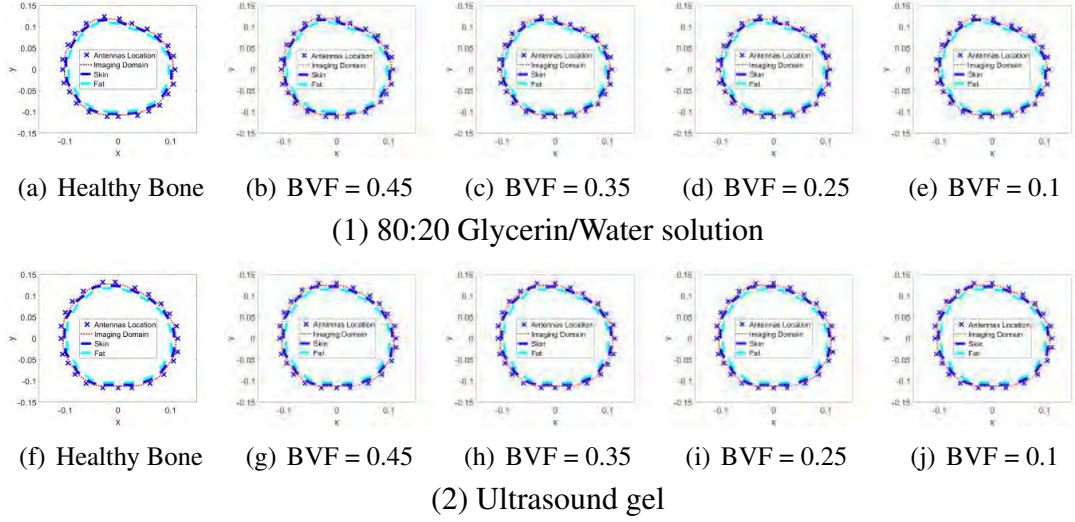


Figure 6.8: MRI model 2: The real-part based clustering estimated models.

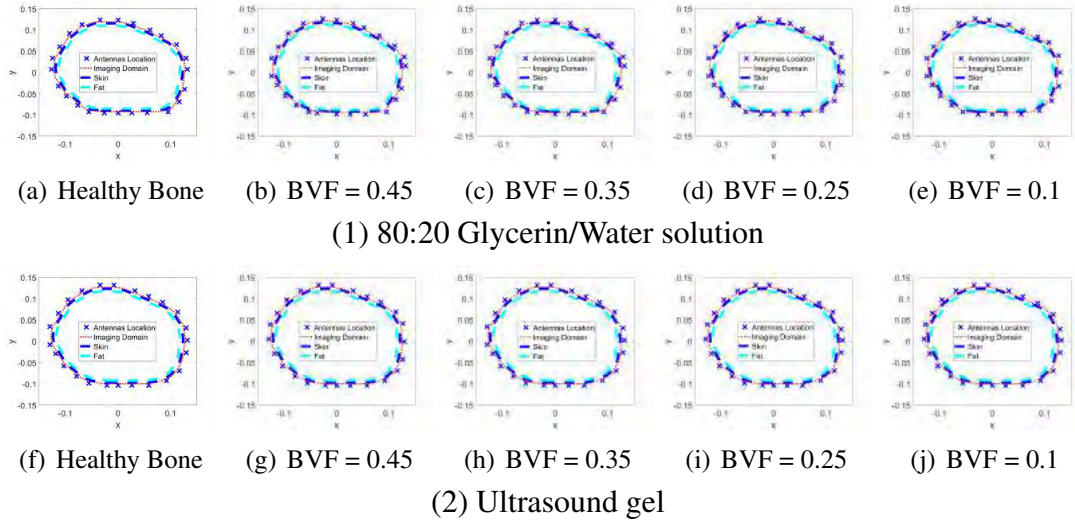


Figure 6.9: MRI model 3: The real-part based clustering estimated models.

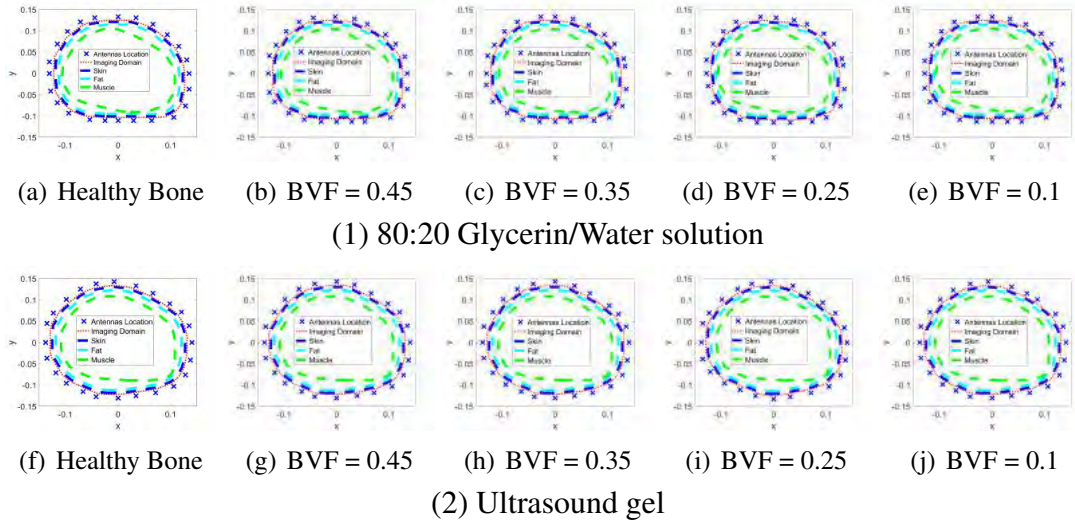


Figure 6.10: MRI model 1: The imaginary-part based clustering estimated models.



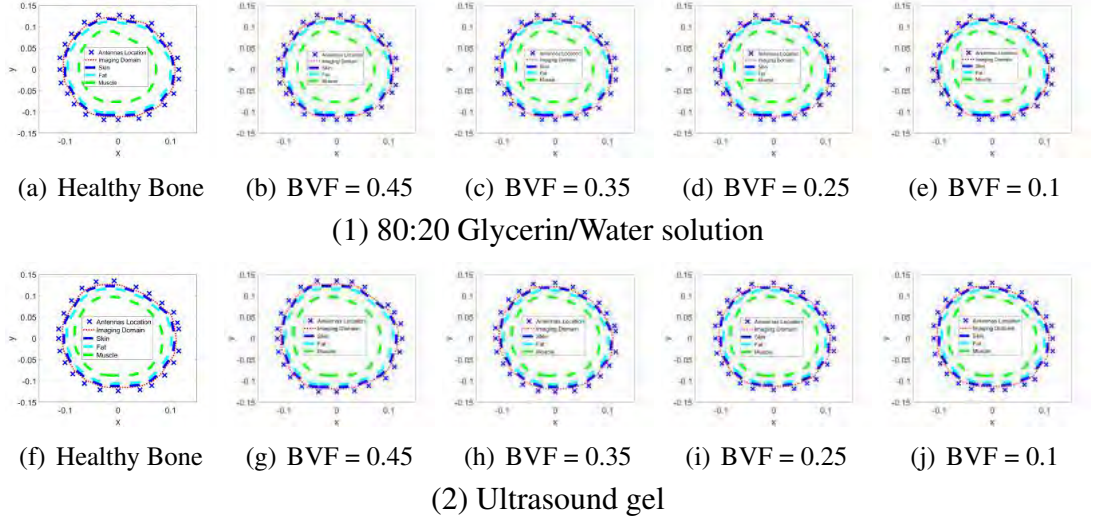


Figure 6.11: MRI model 2: The imaginary-part based clustering estimated models.

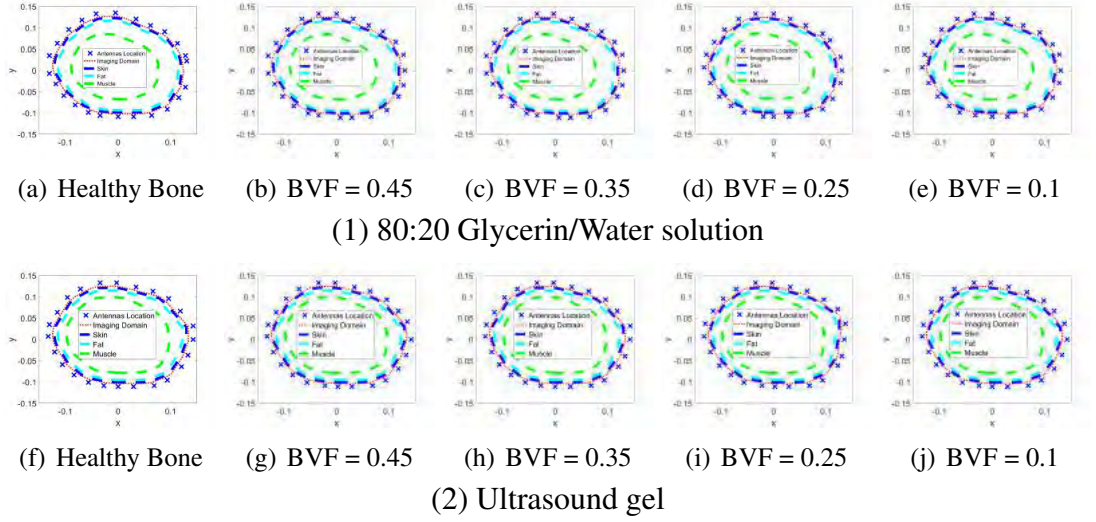


Figure 6.12: MRI model 3: The imaginary-part based clustering estimated models.

within the inversion algorithm using different inhomogeneous background scenarios. MRI model 1 inversion results using the real-part based clustering estimated model are shown in Figures 6.13, 6.14, 6.15, and 6.16. MRI model 2 inversion results using the real-part based clustering estimated model are shown in Figures 6.17, 6.18, 6.19, and 6.20. MRI model 3 inversion results using the real-part based clustering estimated model are shown in Figures 6.21, 6.22, 6.23, and 6.24.



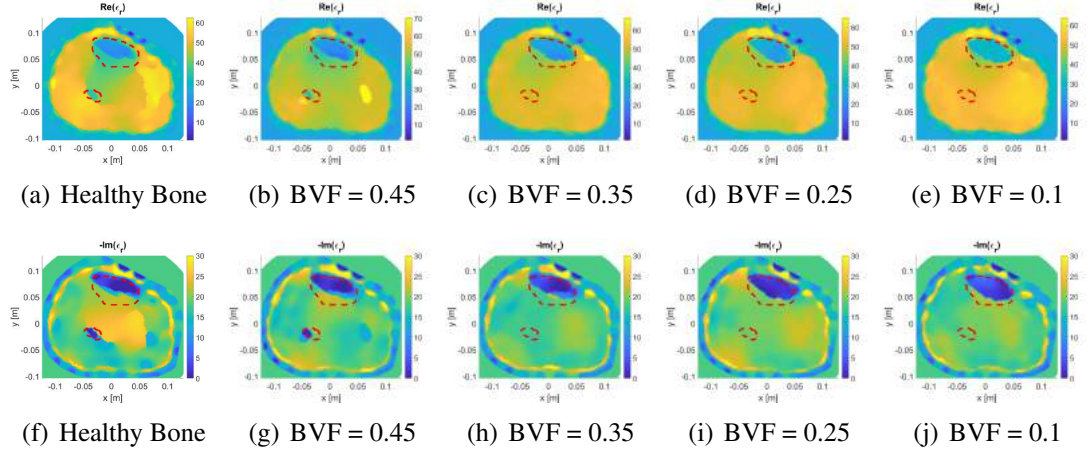


Figure 6.13: MRI model 1: The mid-value inversion results using the real-part based clustering estimated model for 80:20 Glycerin/Water solution.

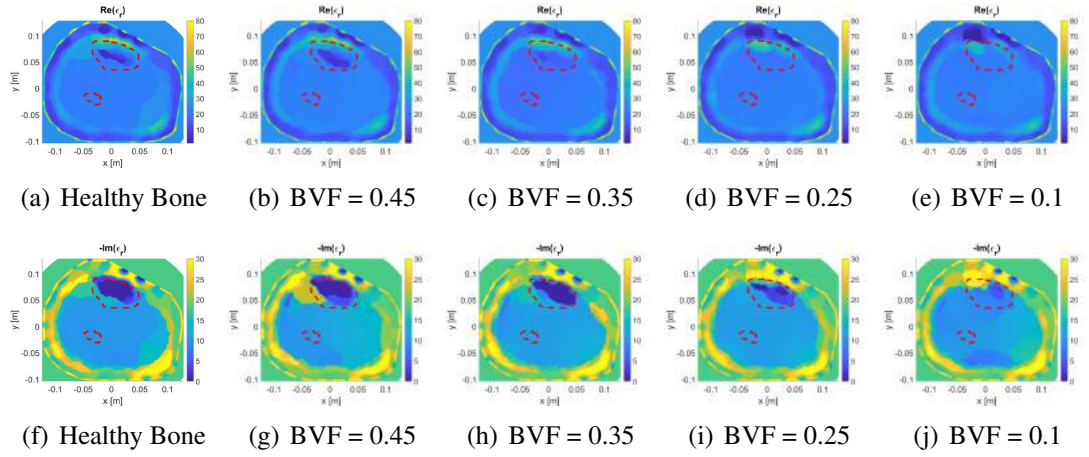


Figure 6.14: MRI model 1: The skin-fat inversion results using the real-part based clustering estimated model for 80:20 Glycerin/Water solution.

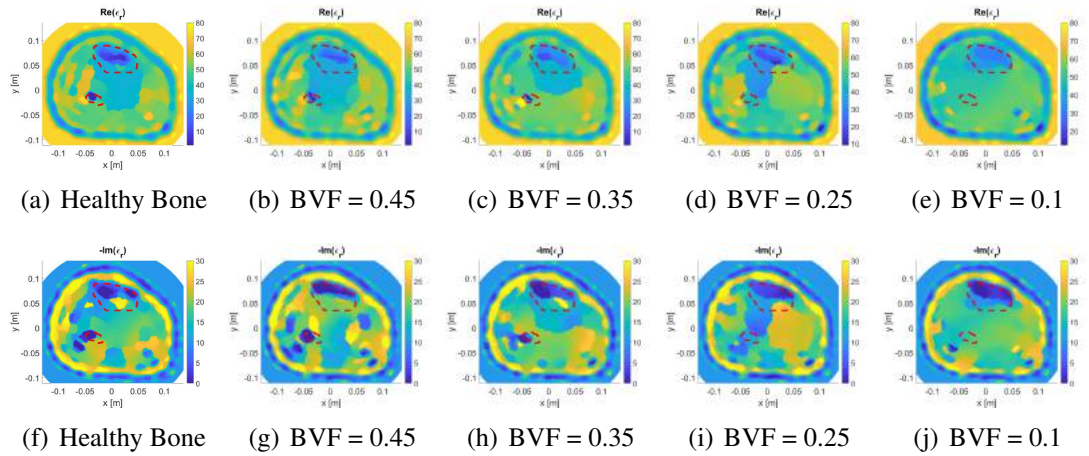


Figure 6.15: MRI model 1: The mid-value inversion results using the real-part based clustering estimated model for ultrasound gel.

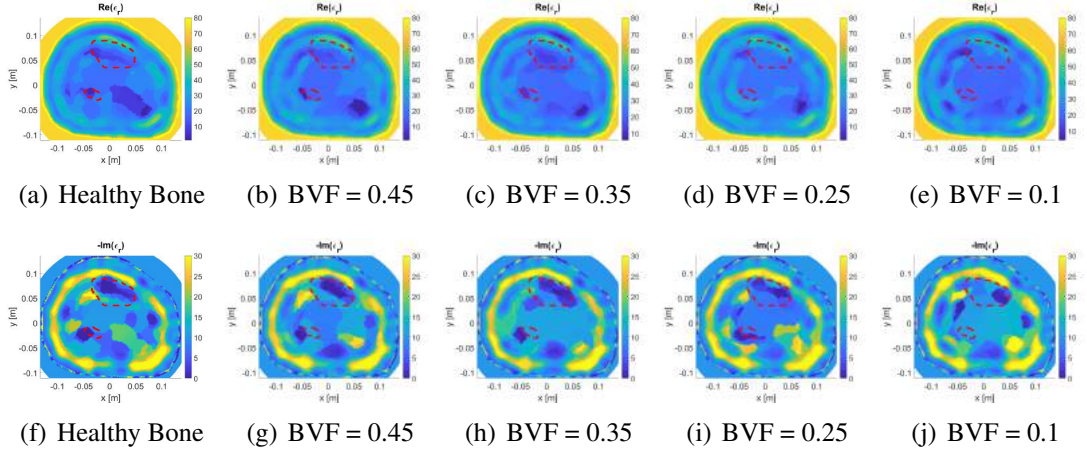


Figure 6.16: MRI model 1: The skin-fat inversion results using the real-part based clustering estimated model for ultrasound gel.

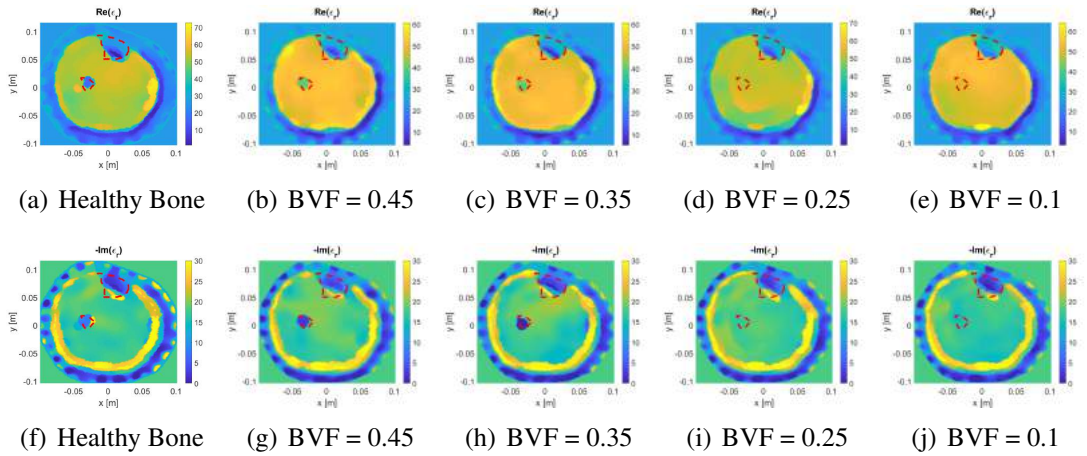


Figure 6.17: MRI model 2: The mid-value inversion results using the real-part based clustering estimated model for 80:20 Glycerin/Water solution.

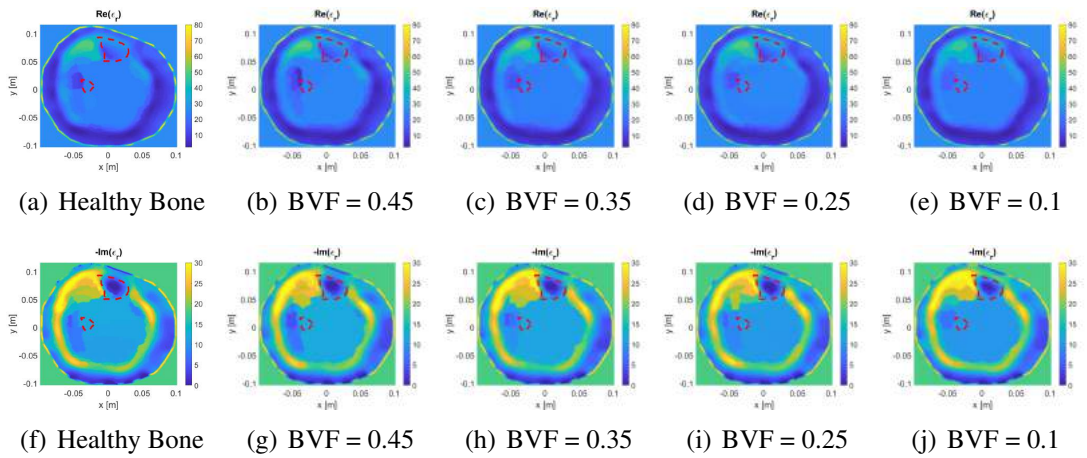


Figure 6.18: MRI model 2: The skin-fat inversion results using the real-part based clustering estimated model for 80:20 Glycerin/Water solution.



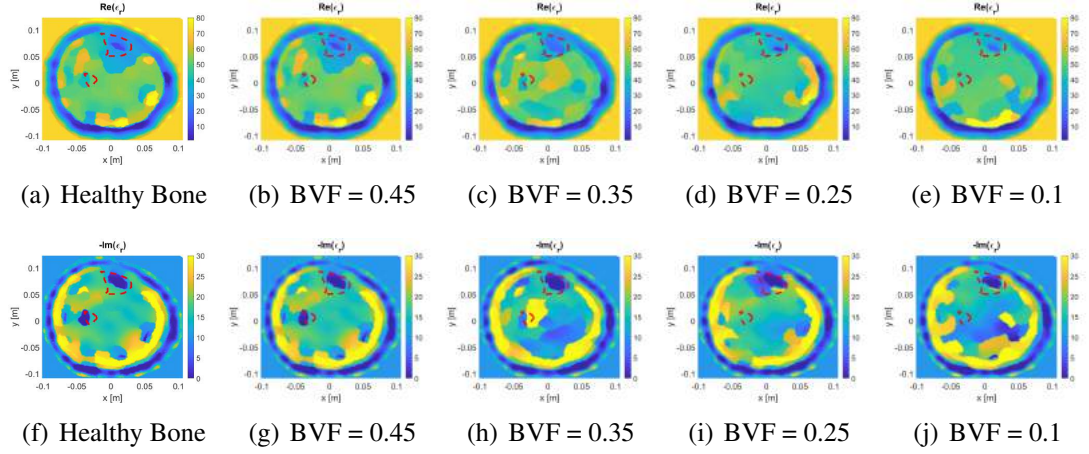


Figure 6.19: MRI model 2: The mid-value inversion results using the real-part based clustering estimated model for ultrasound gel.

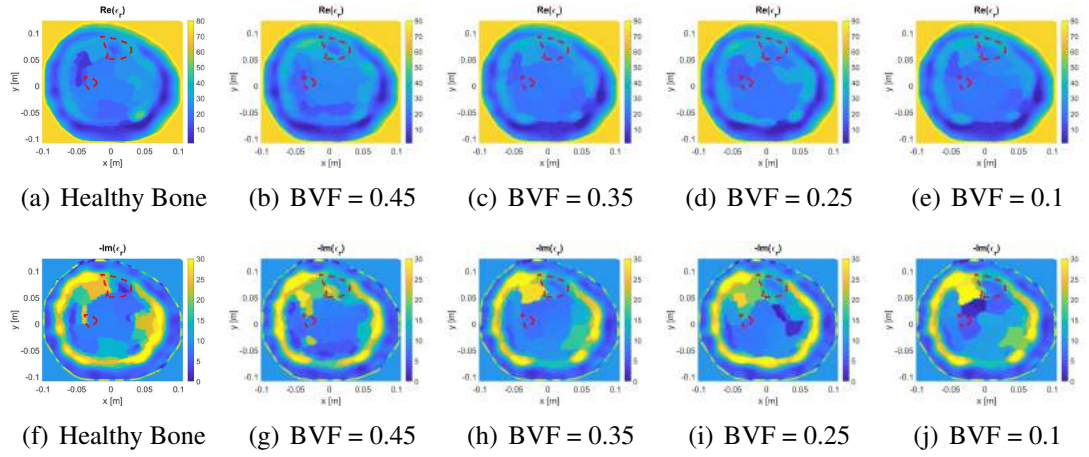


Figure 6.20: MRI model 2: The skin-fat inversion results using the real-part based clustering estimated model for ultrasound gel.

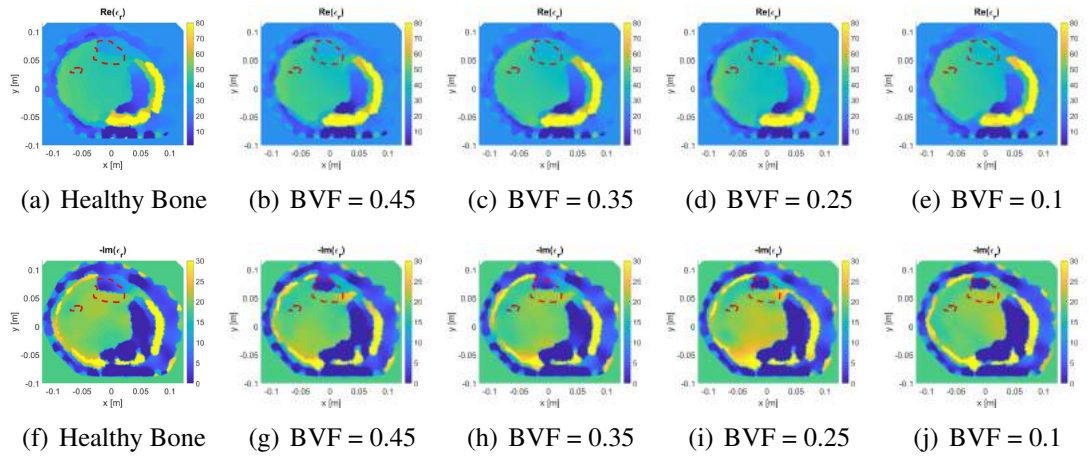


Figure 6.21: MRI model 3: The mid-value inversion results using the real-part based clustering estimated model for 80:20 Glycerin/Water solution.

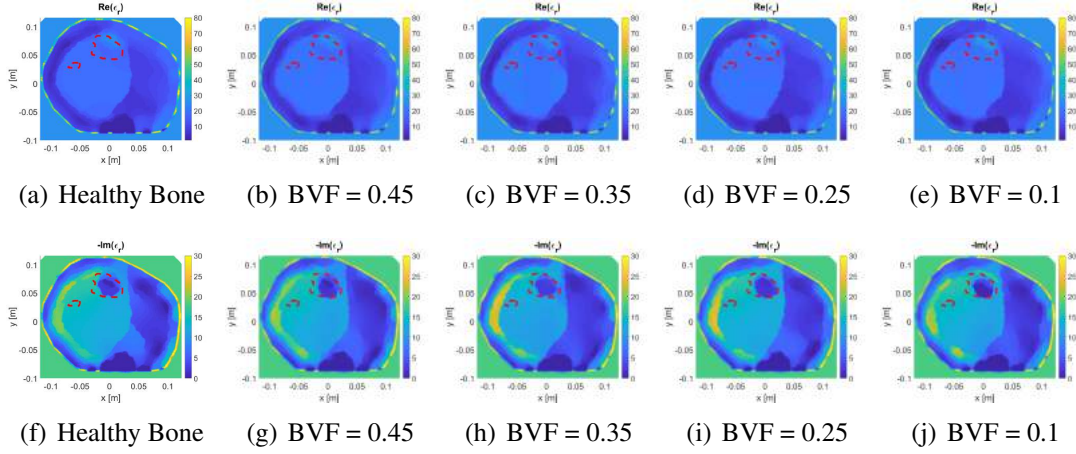


Figure 6.22: MRI model 3: The skin-fat inversion results using the real-part based clustering estimated model for 80:20 Glycerin/Water solution.

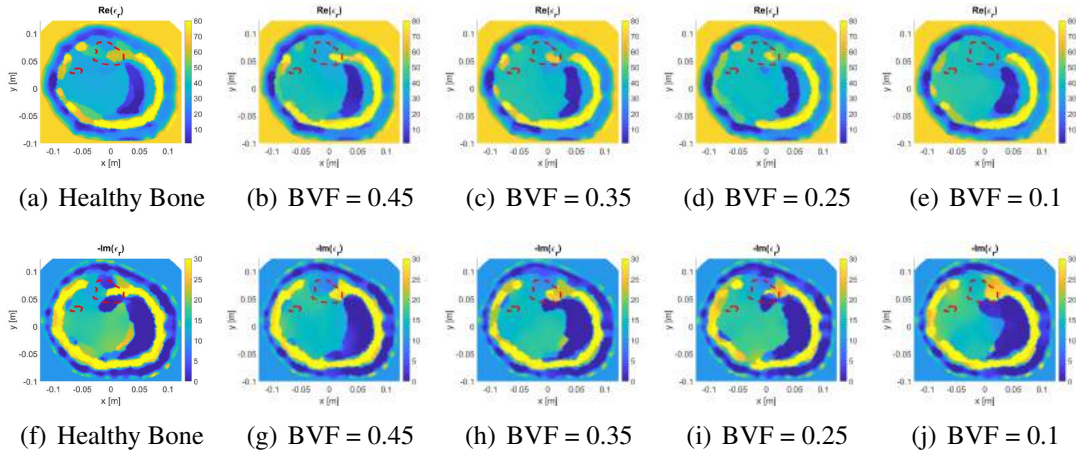


Figure 6.23: MRI model 3: The mid-value inversion results using the real-part based clustering estimated model for ultrasound gel.

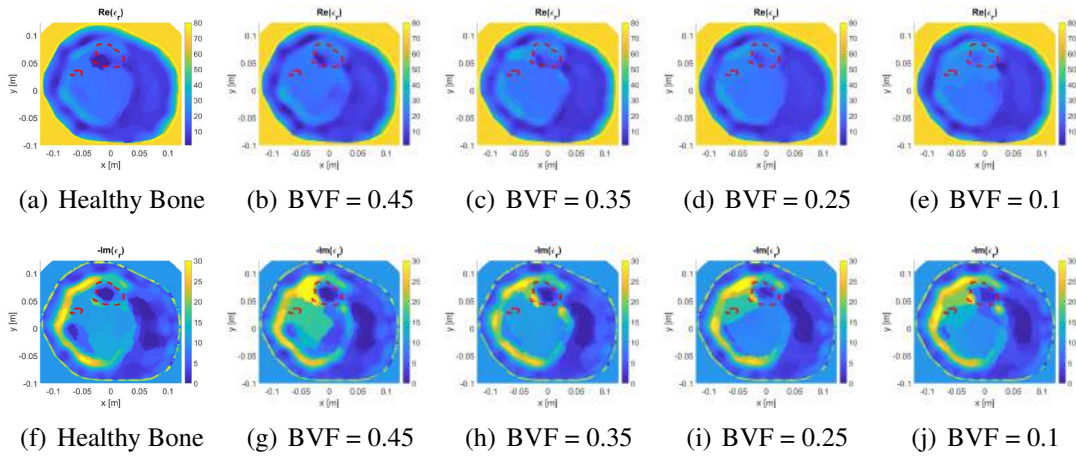


Figure 6.24: MRI model 3: The skin-fat inversion results using the real-part based clustering estimated model for ultrasound gel.

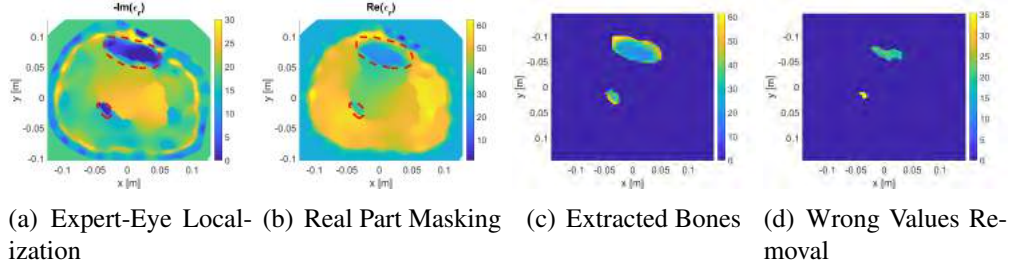


Figure 6.25: MRI model 1: The complete bone values extraction procedure results using 80:20 Glycerin/Water solution.

#### 6.4. Statistical Analysis of Bone Health Variations

To obtain information about the health of bones, both bones are extracted separately, whenever possible, to acquire their corresponding estimated relative complex permittivity values. This is achieved by following these steps,

1. Expert-Eye Localization: Manual localization of bones from the imaginary part reconstructed images to obtain bone masks.
2. Real Part Extraction: Applying the mask on the real part reconstructed images to obtain corresponding segments.
3. Discarding Wrong Values: Removing any values that are more than the first quartile of the obtained bone data points, which are considered as wrong bone values.
4. Finding Mean and Standard Deviation: Obtaining the mean and standard deviation of each estimated bone location.

As an example, the results of this procedure applied on healthy bone scenarios for MRI models 1, 2, and 3 utilizing mid-value inhomogeneous background and 80:20 Glycerin/Water solution matching medium are shown in Figures 6.25, 6.26, and 6.27. This procedure is applied on all scenarios of BVF and MRI models.

Furthermore, Figures 6.28, 6.29, and 6.30 show the line plots of MRI model 1, 2, and 3, respectively, using 80:20 Glycerin/Water solution and ultrasound gel. In these figures, the mean value of the estimated real part for the bones' relative permittivity versus BVF is plotted. Moreover, in each figure, the circles represent successful detection of bones, while the crosses represent the failure to detect bones.

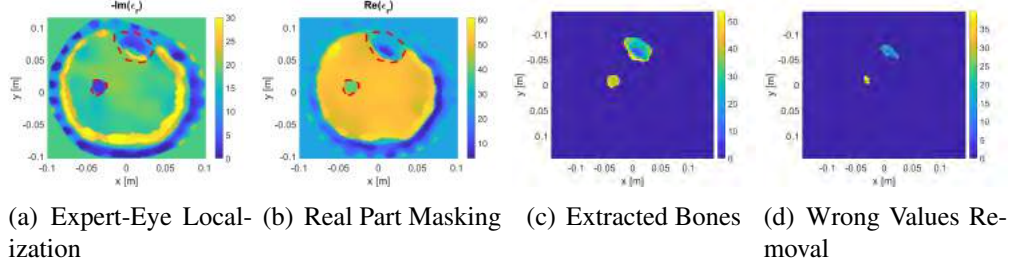


Figure 6.26: MRI model 2: The complete bone values extraction procedure results using 80:20 Glycerin/Water solution.

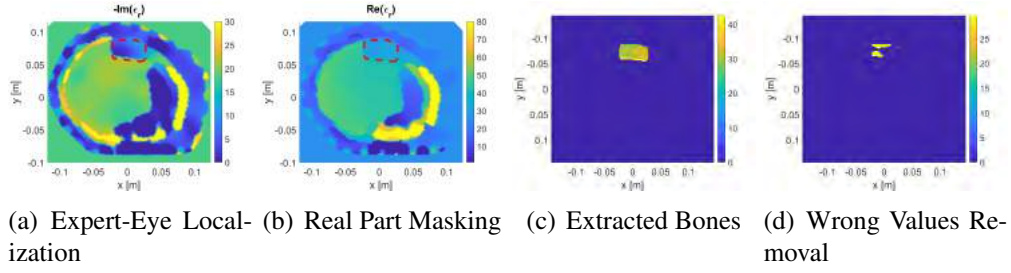


Figure 6.27: MRI model 3: The complete bone values extraction procedure results using 80:20 Glycerin/Water solution.

## 6.5. Analysis and Observations

Based on the results shown in Section 6.3, bone health variations are successfully observed. As BVF decreases, the real part relative permittivity increases. In addition, the fibula bone, in most cases, started disappearing and emerging with the

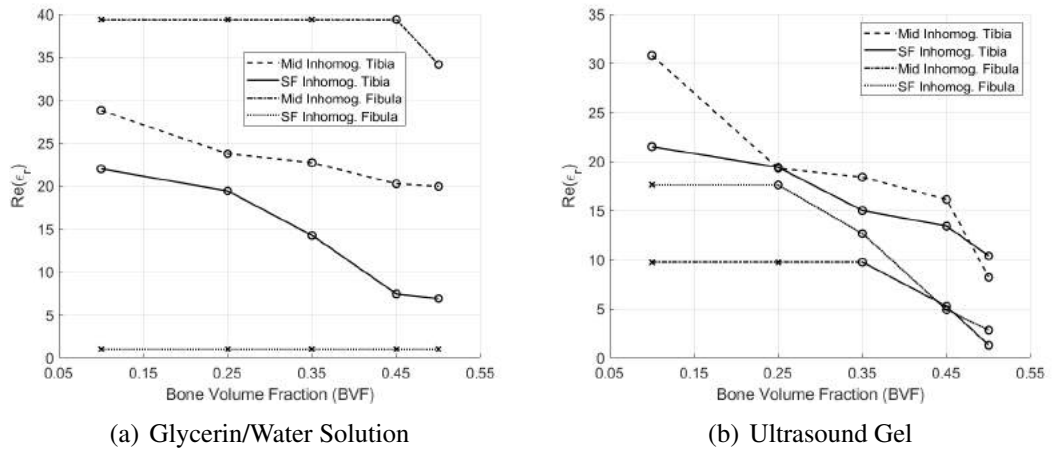


Figure 6.28: MRI model 1: The line plot representation of the mean value of the real part relative permittivity of bones.



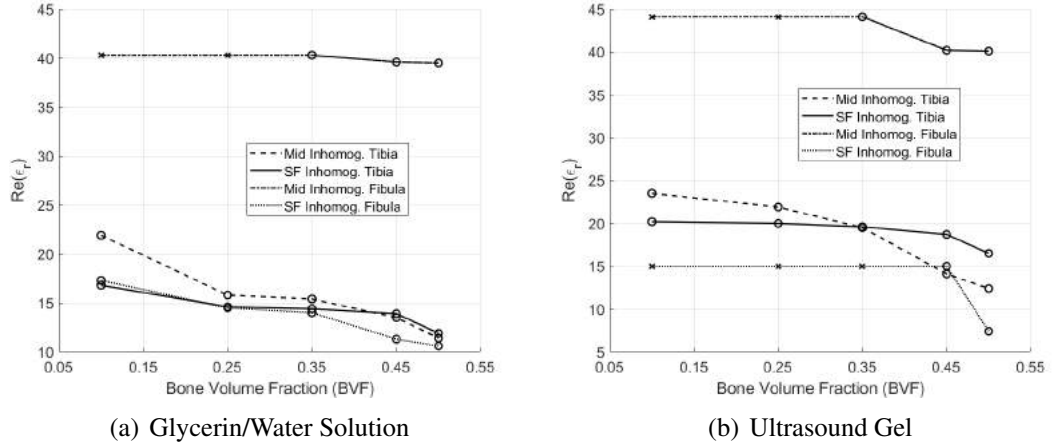


Figure 6.29: MRI model 2: The line plot representation of the mean value of the real part relative permittivity of bones.

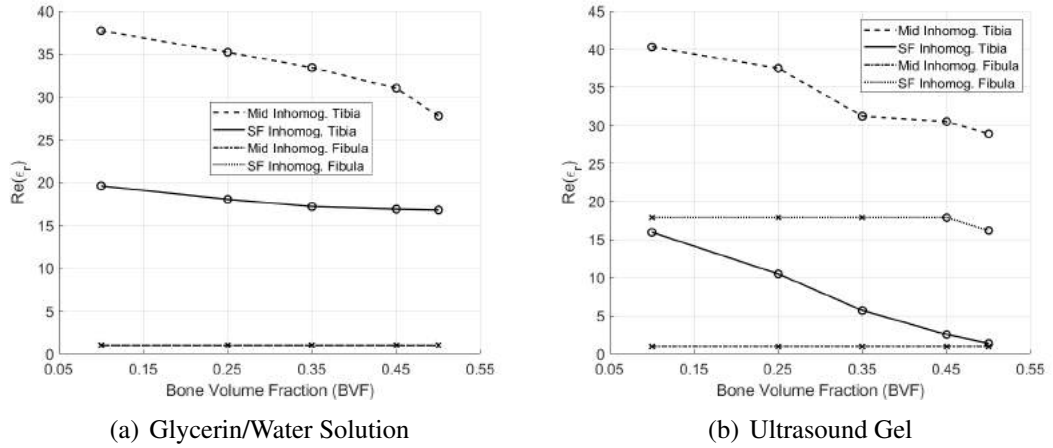


Figure 6.30: MRI model 3: The line plot representation of the mean value of the real part relative permittivity of bones.

surrounding muscle layer. Both the Glycerin/Water solution and the ultrasound gel provided the described behavior of the reconstruction process. Furthermore, the mid-value inhomogeneous background scenario helped in localizing both bones much better than the skin-fat scenario. However, the latter resulted in bones' relative permittivity values closer to the literature values than the former.

The line plots show that whenever the bone is increasing in terms of its BVF value, the plot follows a decreasing pattern. This is easily observable for all three MRI models for both inhomogeneous scenarios. In addition, as the bones' BVF decreases, the fibula bone was not detected successfully as it get emerged with the muscle tissues.

From this chapter, the following can be observed,

- The blind inversion images at any BVF scenario could be used to build estimated models using the proposed procedures.
- Bone health variations in terms of BVF ratio differences can be successfully extracted from MWT reconstructed images.
- The line plot follows a decreasing pattern in terms of real part of the bones' relative permittivity with respect to an increase in BVF.
- The imaginary part fails to localized the fibula bone when the BVF decreases.

All these observations support the hypothesis of this thesis: MWT succeeded in detecting variations in the bones' relative complex permittivity, which correspond to BVF variations that represent changes in bone density. For Vitamin D deficiency treatment, the overall bone density can be measured using MWT to monitor the progress of the treatment.



## Chapter 7: Conclusion and Future Work

In this thesis, an investigation for feasibility of using microwave tomography as a monitoring system for bone healing was performed. Three two-dimensional models illustrating the middle part of a human leg with three fat layer thicknesses were created. Using a finite element solver, the synthetic data was obtained from the forward problem for bones with different values of electrical properties. In the inverse problem, the synthetic measurements from the forward simulations were inverted to create an estimate map of electrical properties of the human leg; the inversion technique used was the contrast source inversion algorithm.

An enhancement procedure for the overall MWT configuration was investigated to improve the reconstruction process of the real and imaginary relative permittivity images. Based on the enhancement procedure, an image processing approach was introduced and evaluated in terms of successful image reconstruction for both tibia and fibula bones. The reconstruction process showed potential of successfully imaging bones.

Further, analysis was carried out for different BVF scenarios, to illustrate bone density loss. In the analysis a process was designed to obtain statistical data about the permittivity values of bones. The results of the analysis were line plots, which showed that changes in the bones' mineralization are reflected as detectable changes in the bones' dielectric properties. In addition, in most reconstructed images, the statistical line plot followed a downward trend in the electrical properties as BVF increases. The results show clearly the potential of using MWT for bone health monitoring.

The future work and recommendations for this thesis include the following points:

- Testing the inversion procedure on actual real bones and performing the degeneration process in the lab.
- Designing an experimental system as a wearable MWT system.
- Imaging the actual treatment process for a Vitamin D deficient patient after developing the actual MWT hardware system.

## References

- [1] P. Meaney *et al.*, “Bone Dielectric Property Variation as a Function of Mineralization at Microwave Frequencies,” *IEEE Transactions on Biomedical Engineering*, vol. 59, no. 12, pp. 3304–3314, 2012.
- [2] N. Watts *et al.*, “National Osteoporosis Foundation 2008 Clinicians Guide to Prevention and Treatment of Osteoporosis and the World Health Organization Fracture Risk Assessment Tool (FRAX): What They Mean to the Bone Densitometrist and Bone Technologist,” *Journal of Clinical Densitometry*, vol. 11, no. 4, pp. 473–477, 2008.
- [3] W. Bani-issa *et al.*, “Vitamin D Deficiency and Its Determinants in Adults: A Sample from Community-Based Settings in the United Arab Emirates,” *International Journal of Endocrinology*, vol. 2017, no. 3, pp. 1–7, 2017.
- [4] P. Meaney *et al.*, “Clinical Microwave Tomographic Imaging of the Calcaneus: A First-in-Human Case Study of Two Subjects,” *IEEE Transactions on Biomedical Engineering*, vol. 59, no. 12, pp. 3304–3313, 2012.
- [5] Z. Tian *et al.*, “Microwave Tomographic Imaging for Osteoporosis Screening: a Pilot Clinical Study,” presented at the IEEE Eng. Med. Biol. Soc., 2010, pp. 1218–1221.
- [6] W. Bradley, “History of Medical Imaging,” *Proceedings of the American Philosophical Society*, vol. 152, no. 3, pp. 349–361, 2008.
- [7] N. Smith and A. Webb, *Introduction to Medical Imaging: Physics, Engineering and Clinical Applications*. Cambridge, UK: Cambridge Texts in Biomedical Engineering, 2011.
- [8] K. Doi, “Diagnostic Imaging Over the Last 50 Years: Research and Development in Medical Imaging Science and Technology,” *Phys. Med. Biol.*, vol. 51, no. 1, pp. 5–27, 2006.
- [9] C. Gilmore *et al.*, “Microwave Imaging of Human Forearms: Pilot Study and Image Enhancement,” *International Journal of Biomedical Imaging*, vol. 2013, pp. 1–17, 2013.
- [10] E. Hall, “Lessons We Have Learned from Our Children: Cancer Risk from Diagnostic Radiology,” *Pediatric Radiology*, vol. 32, no. 10, pp. 700–706, 2002.
- [11] R. Acharya *et al.*, “Biomedical Imaging Modalities: A Tutorial,” *Computerized Medical Imaging and Graphics*, vol. 19, no. 1, pp. 3–25, 1995.
- [12] C. Pichot *et al.*, “Active Microwave Imaging of Inhomogeneous Bodies,” *IEEE Transactions on Antennas and Propagations*, vol. 33, no. 4, pp. 416–425, 1985.
- [13] R. Chandra *et al.*, “Medical microwave imaging and analysis,” in *Medical Image Analysis and Informatics: Computer-aided Diagnosis and Therapy*, P. Marques *et al.*, Eds. Boca Raton, Florida: CRC Press, 2017, pp. 451–466.

- [14] W. Khor *et al.*, “An Ultra Wideband Microwave Imaging System for Breast Cancer Detection,” presented at the International Symposium on Antennas and Propagation, Singapore, 2006.
- [15] T. Ruback, A. Fhager, and P. Jensen, “Microwave Imaging for Breast Cancer Detection: Comparison of Tomographic Imaging Algorithms using Single-frequency and Time-domain Data,” presented at the URSI General Assembly and Scientific Symposium, Istanbul, Turkey, 2011, pp. 13–20.
- [16] C. Gabriel, S. Gabriel, and E. Corthout, “The Dielectric Properties of Biological Tissues: I. Literature Survey,” *Phys. Med. Biol.*, vol. 41, p. 22312249, 1996.
- [17] Q. Liu *et al.*, “Active Microwave Imaging I2-D Forward and Inverse Scattering Methods,” *IEEE Transactions on Microwave Theory and Techniques*, vol. 50, no. 1, pp. 123–133, 2002.
- [18] R. Wojnar, “Bone and Cartilage its Structure and Physical Properties,” in *Biomechanics of Hard Tissues: Modeling, Testing, and Materials*, A. Ochsner and W. Ahmed, Eds. Weinheim: Wiley, 2010.
- [19] E. Marieb and S. Keller, *Essentials of Human Anatomy and Physiology*. Pearson, 2017.
- [20] K. Mount. (2011, Nov.) Anterior Leg, Part 1: The Supporting Cast. Internet. [Online]. Available: <http://anatomyproartifex.blogspot.ae/2011/11/anterior-leg-part-1-supporting-cast.html> [Accessed: Nov 20, 2011].
- [21] K. Kennel, M. Drake, and D. Hurley, “Vitamin D Deficiency in Adults: When to Test and How to Treat,” *Mayo Clin Proc.*, vol. 85, no. 8, pp. 752–758, 2010.
- [22] D. Hanley *et al.*, “Vitamin D in Adult Health and Disease: A Review and Guideline Statement from Osteoporosis Canada,” *CMAJ*, vol. 182, no. 12, pp. E610–E618, 2010.
- [23] E. Laird *et al.*, “Vitamin D and Bone health; Potential Mechanism,” *Nutrients*, vol. 2, pp. 694–724, 2010.
- [24] A. Nazarian and D. Stechow, “Bone Volume Fraction Explains the Variation in Strength and Stiffness of Cancellous Bone Affected by Metastatic Cancer and Osteoporosis,” *Calcif Tissue Int*, vol. 83, pp. 368–379, 2008.
- [25] E. Laird *et al.*, “Bone Volume Fraction and Structural Parameters for Estimation of Mechanical Stiffness and Failure Load of Human Cancellous Bone Samples; In-vitro Comparison of Ultrasound Transit Time Spectroscopy and X-ray CT,” *ELSEVIER, Bone*, vol. 107, pp. 145–153, 2018.
- [26] J. Wu *et al.*, “Effects of Bone Mineral Fraction and Volume Fraction on the Mechanical Properties of Cortical Bone,” *Journal of Medical and Biological Engineering*, vol. 26, pp. 1–7, 2005.

- [27] S. Semenov and R. Corfield, "Microwave Tomography for Brain Imaging: Feasibility Assessment for Stroke Detection," *International Journal of Antennas and Propagation*, vol. 2008, pp. 1–8, 2008.
- [28] I. Sarwar *et al.*, "Low-Cost Low-Power Acceleration of a Microwave Imaging Algorithm for Brain Stroke Monitoring," *Journal of Low Power Electronics and Applications*, vol. 8, no. 43, pp. 1–13, 2018.
- [29] A. Golnabi *et al.*, "Microwave Imaging for Breast Cancer Detection: Advances in ThreeDimensional Image Reconstruction," presented at the 33rd Annual International Conference of the IEEE EMBS, Boston, Massachusetts USA., 2011, pp. 5730–5733.
- [30] A. Zamani *et al.*, "Boundary Estimation of Imaged Object in Microwave Medical Imaging Using Antenna Resonant Frequency Shift," *IEEE Transactions on Antennas and Propagation*, vol. 66, no. 2, pp. 927–936, 2018.
- [31] M. Omer *et al.*, "Proof-of-Concept of the Incorporation of Ultrasound-Derived Structural Information into Microwave Radar Imaging," *IEEE Journal of Multiscale and Multiphysics Computational Techniques*, vol. 3, pp. 129–139, 2018.
- [32] L. Guo and A. Abbosh, "Stroke Localization and Classification Using Microwave Tomography with K-Means Clustering and Support Vector Machine," *Bioelectromagnetics*, vol. 39, pp. 312–324, 2018.
- [33] A. Peyman, A. Rezazadeh, and C. Gabriel, "Changes in the Dielectric Properties of Rat Tissue as a Function of Age at Microwave Frequencies," *Phys. Med. Biol.*, vol. 46, pp. 1617–1629, 2001.
- [34] M. Surita, A. Marwaha, and S. Marwaha, "Finite Element Analysis for Optimizing Antenna for Microwave Coagulation Therapy," *Journal of Engineering Science and Technology*, vol. 7, no. 4, pp. 462–470, 2017.
- [35] A. Winslow. (1965, Aug.) Magnetic Field Calculations in an Irregular Triangle Mesh. Internet. [Online]. Available: [digital.library.unt.edu/ark:/67531/metadc1034507](https://digital.library.unt.edu/ark:/67531/metadc1034507) [Accessed: March 26, 2018].
- [36] A. Zakaria, "The Finite-Element Contrast Source Inversion Method for Microwave Imaging Applications," PhD thesis, University of Manitoba, Canada, 2012.
- [37] P. M. Van Den Berg and R. E. Kleinman, "A Contrast Source Inversion Method," *Inverse problems*, vol. 13, no. 6, p. 1607, 1997.
- [38] A. Micheau and D. Hoa. (2017, Dec.) MRI of the Lower Extremity Anatomy - Atlas of the Human Body using Cross-sectional Imaging. Internet. [Online]. Available: <https://www.imaio.com/en/e-Anatomy/Limbs/Lower-extremity-MRI> [Accessed: Dec 22, 2017].
- [39] V. Tatco. (2016, Mar.) Normal MRI of the Leg. Internet. [Online]. Available: <https://radiopaedia.org/cases/normal-mri-of-the-leg> [Accessed: Mar 19 2016].

- [40] R. George *et al.* (2017, Dec.) Lower Leg Images. Internet. [Online]. Available: <https://mrimaster.com> [Accessed: Dec 22, 2017].
- [41] C. Geuzaine and J. Remacle, "GMSH: a Three-Dimensional Finite Element Mesh Generator with Built-in Pre- and Post-Processing Facilities," *International Journal for Numerical Method in Engineering*, vol. 79, no. 11, pp. 1–24, 2009.
- [42] N. Charles, "Simulation of Dynamic Propagation of Electromagnetic Wave in Microwave Passive Components Using Open Source Finite Element Software," *International Journal of Emerging Technology and Advanced Engineering*, vol. 3, no. 8, pp. 44–50, 2013.
- [43] S. Alias *et al.*, "A Brief Review of Surface Meshing in Medical Images for Biomedical Computing and Visualization," *International Symposium on Research in Innovation and Sustainability*, vol. 26, no. 5, pp. 1741–1744, 2014.
- [44] G. Melia, "Electromagnetic Absorption by the Human Body from 1 to 15 GHz," PhD thesis, The University of York, UK, 2013.
- [45] X. Li, "Body Matched Antennas for Microwave Medical Applications," Ph.D. dissertation, Karlsruher Forschungsberichte aus dem Institut für Hochfrequenztechnik und Elektronik, 2013.
- [46] A. Zakaria, C. Gilmore, and J. LoVetri, "Finite-element Contrast Source Inversion Method for Microwave Imaging," *Inverse Problems*, vol. 26, no. 11, p. 115010, 2010.
- [47] M. Alkhodari, A. Zakaria, and N. Qaddoumi, "Preliminary Numerical Analysis of Monitoring Bone Density Using Microwave Tomography," presented at the Asia-Pacific Microwave Conference (APMC), Kyoto, Japan, 2018.
- [48] Q. Fang, "Computational Methods for Microwave Medical Imaging," PhD thesis, Dartmouth College, Hanover, 2004.
- [49] P. Meaney *et al.*, "Importance of Using a Reduced Contrast Coupling Medium in 2D Microwave Breast Imaging," *Journal of Electromagnetic Waves and Applications*, vol. 17, pp. 333–355, 2003.
- [50] A. H. Golnabi, P. M. Meaney, and K. D. Paulsen, "Tomographic Microwave Imaging with Incorporated Prior Spatial Information," *IEEE Transactions on Microwave Theory and Techniques*, vol. 61, no. 5, pp. 2129–2136, 2013.
- [51] P. Labs. AquaSonic 100: Ultrasound Transmission Gel. Internet. [Online]. Available: <https://www.parkerlabs.com/aquasonic-100.asp> [Accessed: 01.01.2019].
- [52] Keysight. N1501A Dielectric Probe Kit. [Online]. Available: <https://www.keysight.com/en/pd-2492144-pn-N1501A/dielectric-probe-kit?cc=AE&lc=eng> [Accessed: 01.01.2019].
- [53] S. Lloyd, "Least Squares Quantization in PCM," *IEEE Transactions on Information Theory*, vol. 28, no. 2, pp. 129–137, 1983.

- [54] N. Singh, A. Mohapatra, and G. Kanungo, “Breast Cancer Mass Detection in Mammograms using K-means and Fuzzy C-means Clustering,” *International Journal of Computer Applications*, vol. 22, no. 2, pp. 15–21, 2011.
- [55] MATLAB. MATLAB Image Processing Toolbox. [Online]. Available: <https://www.mathworks.com/products/image.html> [Accessed: 01.01.2019].
- [56] J. Canny, “A computational approach to edge detection,” in *Readings in computer vision*. Elsevier, 1987, pp. 184–203.
- [57] K. S. Cole and R. H. Cole, “Dispersion and Absorption in Dielectrics I. Alternating Current Characteristics,” *The Journal of chemical physics*, vol. 9, no. 4, pp. 341–351, 1941.

## Appendix A: Dielectric Probe Measurements

The equipment used to measure the dielectric properties of different materials are Keysight's N1501A dielectric probe connected to a vector network analyzer (VNA) [52]. The VNA is controlled by a computer hosting a software that calculates the dielectric properties based on VNA measurements. The measurement setup, shown in Fig. 7.1, is available in microwave engineering laboratory at the American University of Sharjah.

Before starting with the measurements, the dielectric probe software is calibrated using three known loads, which are free-space, a short load, and distilled water. The calibration is performed in the frequency range at which the permittivity will be measured. A picture of the two calibration loads is shown in Fig. 7.2. The frequency range at which calibrations and measurements were performed was 0.5 GHz to 1.5 GHz.

After calibration is done, the dielectric probe is inserted into the liquid whose properties are to be measured. In this thesis, the liquid was the AquaSonic 100 ultrasound gel. Next, the software on the host computer is run, and the outputs are two plots of the real and imaginary components of the complex relative permittivity of the liquid within the chosen frequency range.

An example of measurement results compared to theoretical literature values are shown in Fig. 7.3 for distilled water. The theoretical values of water electrical properties

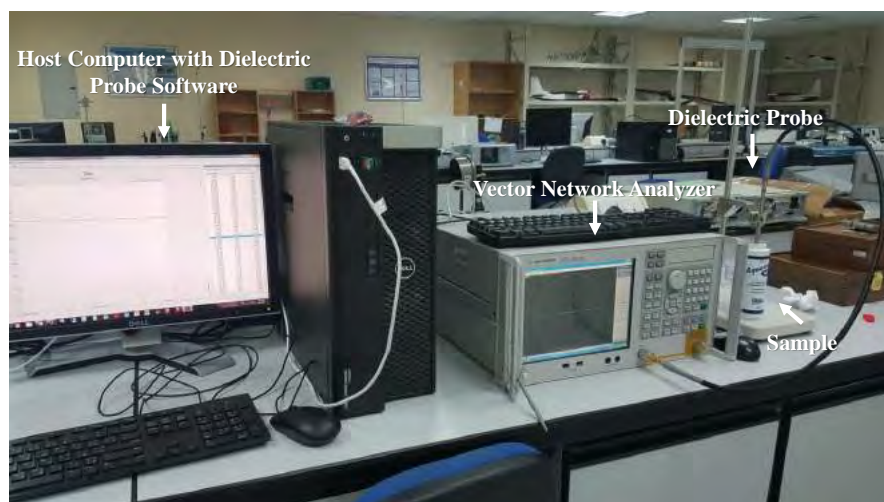


Figure 7.1: The setting used to measure AquaSonic 100 ultrasound gel dielectric properties.

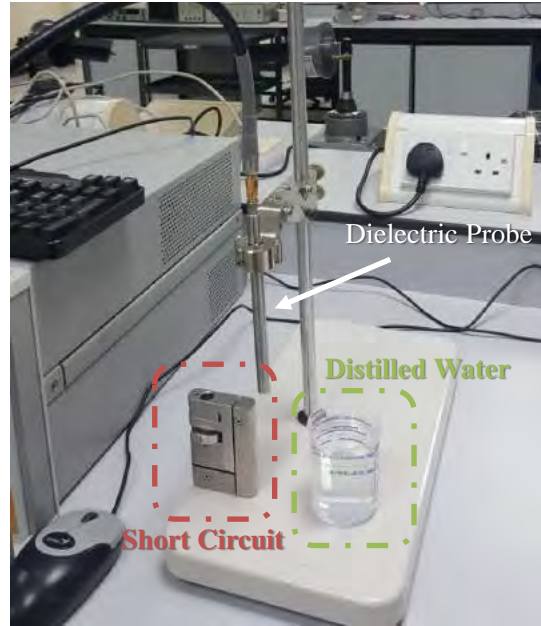


Figure 7.2: The loads used for calibrating the probe: short-circuit load and distilled water.

can be obtained using the Cole-Cole model [57]. As can be seen from the figure, the results are similar to each other with small variations. These variation may occur due to the water used not being truly distilled, or due to measurements errors like cable movement as the probe is lowered into the liquid.

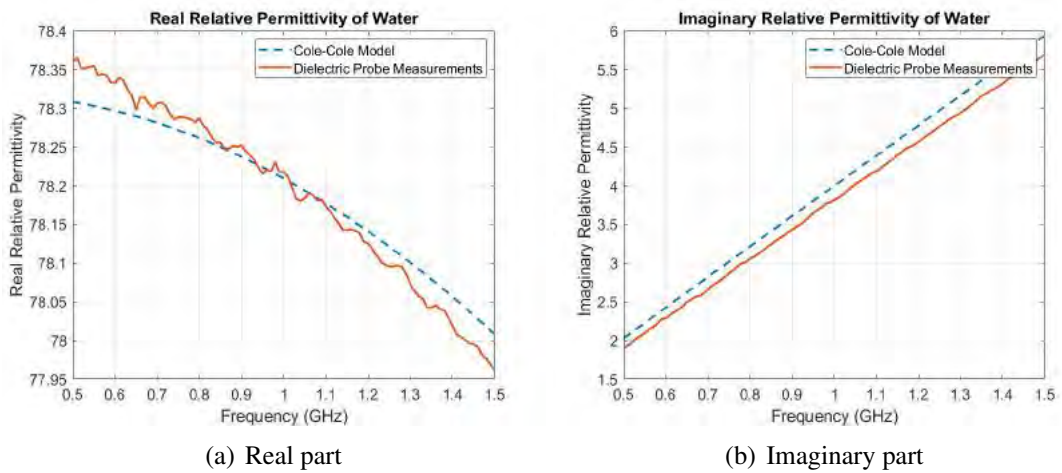


Figure 7.3: Relative permittivity values of distilled water: theoretical values versus measurements.



## **Vita**

Mohanad Alkhodari was born in 1994, in Abu Dhabi, United Arab Emirates (UAE). He received his Bachelors degree with honor in Electrical Engineering from Abu Dhabi University (ADU), United Arab Emirates (UAE) in 2017. In summer 2017, he joined the Microsystems Lab (iMicro) at Masdar Institute, UAE, working on ultrasound systems design as a Research Assistant Intern. He is currently a Teaching and Research Assistant in the College of Engineering at the American University of Sharjah (AUS), UAE, where he is pursuing his Masters degree in Biomedical Engineering with a full scholarship granted by the university to distinguished students. In summer 2018, he undertook a practical training in biomedical engineering at Health Shield Medical Center (HSMC) of Capital Health, Abu Dhabi. Alkhodari is an active representative of the Electrical and Biomedical Engineering Masters programs for the IEEE Engineering in Medicine and Biology Society (EMBS) Student Chapter at the AUS. In 2019, he won the first place at the UAE Ministry of Health and Prevention (MOHAP) Innovations in Health Hackathon with a group idea of a smart wearable cap for epileptic patients. Alkhodari won the first place in the Undergraduate Research Competition (URC) held at ADU in spring 2017 with his graduation research of a smartphone thermal imaging system for diabetic patients, out of which he authored and published journal paper. His current research interests include medical imaging, medical microwave imaging development, and biomedical signal processing